2009

Quantitative Macro- and Microscale Methods for Characterizing Cell Viability

Julianne Forman Audiffred
Louisiana State University and Agricultural and Mechanical College

Recommended Citation

Audiffred, Julianne Forman, "Quantitative Macro- and Microscale Methods for Characterizing Cell Viability" (2009). *LSU Doctoral Dissertations*. 3813.
https://digitalcommons.lsu.edu/gradschool_dissertations/3813

QUANTITATIVE MACRO- AND MICROSCALE METHODS FOR CHARACTERIZING CELL VIABILITY

A Dissertation

Submitted to the Graduate Faculty of the
Louisiana State University and
Agricultural and Mechanical College
in partial fulfillment of the
requirements for the degree of
Doctor of Philosophy

in

The Interdepartmental Program in
Engineering Science

by
Julianne Forman Audiffred
B.S., Louisiana State University, 2002
M.S., Louisiana State University, 2005
December 2009

DEDICATION

This work is dedicated to my husband, Bryan,
and
my son, Bennett Alexander

ACKNOWLEDGEMENTS

I appreciate the guidance and support of my graduate committee, Dr. Richard Bengtson, Dr. Tryfon Charalampopoulos, Dr. Jin-Woo Choi, Dr. Marybeth Lima, Dr. Steven Soper, and Dr. Todd Monroe. I would especially like to thank my major advisor, Dr. Todd Monroe, for his guidance and continued support over the past few years. His patience helped to make this possible, and I have learned a great deal about professionalism and high-quality work ethics that I know will be invaluable for my future endeavors. Also, I owe much appreciation (and coffee) to Dr. Marybeth Lima for the many years of mentoring during my undergraduate and graduate school experience.

I would also like to thank Dr. Daniel Thomas and the various people in the BAE Department who have assisted me. Financial assistance throughout my graduate work was provided by National Science Foundation (NSF Graduate Research Fellowship), Donald W. Clayton (Donald W. Clayton Assistantship), and Dr. Daniel Hayes (Research Associate position in affiliation with the LSU AgCenter).

There are numerous other graduate and undergraduate students that have provided practical and moral help throughout this interdisciplinary project: Micah Fincher for the technical (testing and modeling) and hands-on assistance in the "art" of fabricating chips, as well as the enthusiasm and optimism when I needed it most; Jack Chiu for the soldering lessons and electronics support; and many other students in the Monroe Lab, including Michael Modica, Paige Brown, Sarah De Leo, Ammar Qureshi, Tyler Clement, Anna Dugas, Chad Jarreau, Rick Blidner, Nicholas Gerbo, Leah Mueller, and especially Carla Haslauer (a colleague who has provided a tremendous amount of support and advice as we have both pursued our doctoral degrees at the same time). Additionally, special thanks go to Marilyn Dietrich in the flow

cytometry core at Veterinary Medicine for her help and use of the flow cytometer; Jason Guy for the many micromilled chips; Matt Hupert, Maggie Witek, and the CBMM community for hot-embossing and initial chip fabrication direction; and Mr. Tom McClure for machine shop expertise.

Finally, I am grateful for my parents, sister, and friends who have supported me throughout my graduate school adventure. The last few months have required long hours and much encouragement, and I could not have completed this dissertation without Circe's devoted companionship during the late-night writing, my husband's unwavering support, and my son's endearing smiles.

TABLE OF CONTENTS

LIST OF TABLES

LIST OF FIGURES

LIST OF ABBREVIATIONS

ATP	adenosine triphosphate
BioMEMS	biological micro-electro-mechanical systems
BF	brightfield microscopy
C_m	membrane capacitance
CHO	Chinese hamster ovary cell line
CPT	camptothecin
DC	doxorubicin-induced cardiomyopathy
DEP	dielectrophoresis
$\Delta\Psi_m$	mitochondrial membrane potential
$DiBAC_4(3)$	(bis-(1,3-dibarbituric acid)-trimethine oxanol
DMEM-RS	Dulbecco's Modified Eagle's Medium-Reduced Serum
DMSO	dimethylsulfoxide
DNA	deoxyribonucleic acid
ECIS	electrical cell-substrate impedance sensing
E-field	electric field
FACS	flow-activated cell sorting
FBS	fetal bovine serum
FITC	fluorescein isothiocyanate
FL	fluorescent
FN	fibronectin protein
FRET	fluorescence resonance energy transfer
GEN	Genistein apoptosis-inducing agent
HeLa	human epithelial carcinoma cells
HL-60	promyelocytic leukemia cells
H_2O_2	hydrogen peroxide
IEF	isoelectric focusing
JC-1	fluorescent probe, mitochondrial potential (forms "J-aggregates")
Jurkat	immortalized T-lymphocyte cell line
K562	human chronic myelogeneous leukaemic cell line
LCR	complex impedance meter (inductor, capacitor, resistor)
MTT	(3-(4,5-Dimethylthiazol-2-yl)-2,5-diphenyltetrazolium bromide)
NI	national instruments
Oligo	oligonucleotide
OM	OptiMEM
PBS	phosphate buffered saline
PCD	programmed cell death
PDMS	polydimethylsiloxane
PI	propidium iodide
PMMA	polymethyl methacrylate.
Pt	platinum
PS	phosphatidylserine, polystyrene
RBCs	red blood cells
RPMI-RS	Roswell Park Memorial Institute (RPMI)- reduced serum media
SEM	scanning electron microscopy

SU-8	epoxy-based negative photoresist
TEM	transmission electron microscopy
TLM	thermal lens microscopy
TMP	transmembrane potential
UVA	ultraviolet light (320-400nm)

ABSTRACT

The goal of this study is to combine molecular and microdevice methods to characterize and quantify viability of single mammalian cells. Fluorescent-based assays were optimized for adherent HeLa and suspension Jurkat cells and were used as a tool for validation of a microfabricated diagnostic device. Cell and substrate/surface interactions were considered for designing a microfluidic device that can be used to characterize cell viability for quantitative biomedical and cell biology applications, which require label-free, real-time monitoring of cells.

Several interdisciplinary methods are employed to evaluate electrical impedance differences between live and dead Jurkat cells in a microfluidic device. Biological Micro-Electro-Mechanical Systems (BioMEMS) offer many advantages over the conventional macroscale approaches to biomedical diagnostics, such as reduced reagents, costs, and power consumption; shorter reaction time; portability; versatility; and potential for parallel, integrated operations, thus having the potential to revolutionize how many current cell-based biomolecular assays are performed. A microchip device to detect cell viability at the single-cell level in real-time has much potential for pharmacological drug screening or point-of-care diagnostics. Optimal cell media conditions such as pH and osmolarity are evaluated to ensure cell viability and adequate sensitivity for detecting cell events via electrical impedance measurements. A fluorescent cell assay using Calcein was optimized for optical validation of Jurkat cell viability studies for cells flowing through a microchannel. Fluorescence microscopy was combined with acquired electrical impedance (at 2 MHz) to validate the presence and viability of each cell at the detection electrodes. The microchip design parameters such as substrate material and geometry of microchannel and electrodes were based of the average 12 um-diameter of Jurkat cells tested. Here, we demonstrate the design of a polymer-based chip device that is able to differentiate

between live and dead Jurkat cells on the basis of electrical impedance magnitude and phase signals, which could be related to inherent dielectric differences of live and dead cells. The overall outcome of this study provides groundwork for quantifying cell viability of single cells on-chip, in real-time, in a flow-through system, without the use of expensive fluorescent labels.

CHAPTER 1. INTRODUCTION

1.1 Background on Cell Viability

1.1.1 Necrosis and Apoptosis

Apoptosis is a complex, tightly regulated programmed cell death (PCD), which is triggered by either internal or external cellular events. Apoptosis (derived from Greek: apo "apart" and ptosis: "fallen") translates to shedding of leaves from tress in autumn and was first studied by Kerr et al. (1972). Apoptotic processes are important for maintaining tissue homeostasis, natural defense mechanisms, and the natural aging process (Vaux and Strasser 1996). Inappropriate regulation of apoptosis results in disease, such as cancer, developmental defects, and neurodegenerative diseases. For therapeutic intervention, a clear understanding and ability to detect apoptotic events is important.

There are two distinct forms of cell death (Fig. 1.1). Necrosis is an uncontrollable pathological form of cell death, characterized by cell swelling, plasma membrane rupture, and inflammation. It is a result of chemical or physical damage to the cell (Kerr et al. 1972). Apoptosis is triggered by milder environmentally damaging stimuli, such as ultraviolet radiation

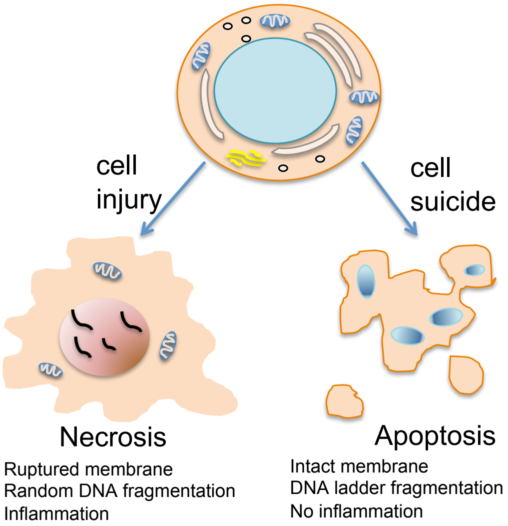

Figure 1.1 Representation illustrating two types of cell death (necrosis and apoptosis).

or lack of growth factors. Loss of cell membrane integrity is a very late event during apoptosis and is similar to the compromised cell membrane characteristic of necrosis. Dissimilar morphological and biochemical features are used to differentiate between necrosis and apoptosis.

Apoptotic processes involve significant changes in the cellular membrane and nucleus. Apoptosis is characterized by phosphatidylserine (PS) translocation from the inner leaflet to the outer leaflet of the phospholipid bilayer, while the cell membrane remains intact. The loss of plasma membrane asymmetry is a universal, early apoptotic event, independent of cell type (van Engeland et al. 1998; Vermes et al. 1995) (Martin et al. 1995). Henson and colleagues were the first to study the connection between PS exposure and apoptosis (Fadok et al. 1992). PS exposure on the cell surface continues until the final stages of apoptosis when the cell has divided into apoptotic bodies.

Additional apoptotic morphological events include condensed chromatin, cell shrinkage and blebbing, asymmetry of the plasma membrane, and formation of apoptotic bodies, which are phagocytized without causing inflammation (Kerr et al. 1972). Along with nucleus fragmentation, a biochemical hallmark of apoptotic cells includes the cleavage of DNA into approximately 200 base pair fragments, which are resolved into a "DNA ladder" by electrophoresis (Willingham 1999). The morphological changes result from characteristic molecular and biochemical events, such as the activation of caspases and release of cytochrome c. Early apoptotic cells are recognized by morphological changes that begin with condensing chromatin, cell shrinkage, and loss of asymmetry of the plasma membrane (Kerr et al. 1972). Later apoptotic events include nucleus fragmentation, DNA "laddering," membrane blebbing, and cell fragmentation. Apoptotic bodies are small, compact vesicles that contain cytosol, condensed chromatin, and organelles. Macrophages engulf and remove apoptotic bodies from

the tissues without causing an inflammatory response. Many apoptosis detection methods target these particular cellular events and are discussed later in further detail.

1.1.2 Conventional Techniques to Measure Apoptosis

There are currently over 300 different apoptosis detection kits on the market for detecting and/or quantifying apoptosis, yet all of these methods still have limitations for acquiring quantitative data of single cells (Valero et al. 2005; Wolbers et al. 2005). Early apoptosis assays relied upon morphologic changes detected by light microscopy, electron microscopy, or flow cytometry using nuclear staining dyes (Koopman et al. 1994). Quantifying apoptosis by microscopy was inexact, and the nonvital dyes would only stain late apoptotic cells once the membrane was damaged. In 1994, Koopman et al. were the first to use labeled annexin V for flow cytometric detection of phosphatidylserine translocation on B cells (Koopman et al. 1994). Ethidium bromide, a nonvital stain, was used to label necrotic cells. The binding of annexin V was found to correlate with apoptotic morphology and is a technique that is widely used for detecting apoptosis. Vermes and collaborators were among the first to study the use of annexin V with apoptotic cells (Vermes et al. 1995).

The biotinylated annexin V assay has been used successfully for flow cytometric analysis of apoptosis (Chan et al. 2003; vanEngeland et al. 1996). Annexin V is a calcium-dependent, phospholipid binding protein with a high affinity for PS (vanEngeland et al. 1996). By double-labeling for annexin V and either a membrane impermeable DNA stain (propidium iodide) or esterase live stain (calcein AM), distinct populations of live, apoptotic, and necrotic cells can be quantified using flow cytometric techniques as seen in Figure 1.2. Stained cells can be viewed for qualitative results under a fluorescence microscope, using appropriate filters, and quantified by flow cytometry.

Some of the other existing apoptosis methods are based on changes in DNA strand breaks (TUNEL assay), DNA fragmentation (DNA laddering), chromatin condensation (light microscopy examination), alteration of membrane integrity (trypan blue or propidium iodide exclusion assays), and cytoplasmic changes (including, intracellular enzyme activity, caspases, Ca^{++} flux, mitochondrion dysfunction). DNA laddering, morphological examination, and exclusion assays do not allow precise quantification of apoptotic cells on a cell-by-cell basis, and the TUNEL assay can be labor-intensive and time-consuming (Leite et al. 1999). Labeled (FITC or biotin) annexin V-affinity assay allows for simultaneous labeling of other cell-surface antigens and can be analyzed quantitatively by flow cytometry and qualitatively by fluorescence microscopy.

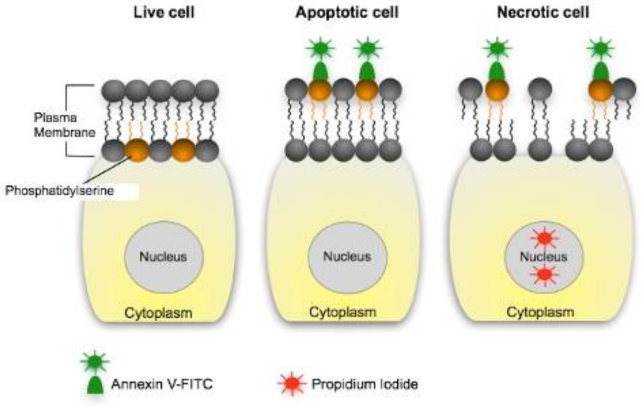

Figure 1.2 The annexin V-FITC, propidium iodide assay shows live, apoptotic, and necrotic cells using annexin V binding and membrane impermeable DNA dye.

1.1.3 Limitations of Conventional Apoptosis Assays

Most of the methods described above are not specific and/or lack quantitative measures. For the flow cytometry assays, a large number of cells are required (10,000 cells), and the labeled antibodies/reagents are expensive (Qin et al. 2005). The cell preparation (staining, centrifuging, wash steps) for analysis is time-consuming (on order of hours for a lot of samples), and thereby makes it impossible to perform real-time monitoring of apoptosis. Also, all of the

flow cytometry assays require a sophisticated, expensive flow cytometer and trained technician. Cells are often unable to be run live and require fixatives for analysis that can interfere with measuring metabolic properties of living cells. The harvesting, staining steps in flow cytometry do not allow for analysis of intact, single cells and are known to introduce artifacts from the manipulation steps (Wolbers et al. 2005). Timing of apoptosis analysis is crucial as apoptosis is a short duration event, a time-dependent and irreversible process once the cascade begins.

1.1.4 Significance and Therapeutic Importance

Apoptosis, programmed cell death, is a major target of drug discovery in fields, such as oncology, gerontology, and recombinant biotechnology (Feng et al. 1999; Valero et al. 2005). A BioMEMS microchip for detecting single-cell apoptosis in a sensitive, targeted, quantitative method in real-time has enormous potential for high-throughput pharmacological screening of drugs. There is much literature describing the critical need for an apoptosis chip device; however, a successful apoptosis device has yet to be reported. Sohn et al. mention the application of pharmacological effects on cell cycle and cell death which could be improved upon through real-time monitoring (Sohn et al. 2000) while Wang's group emphasizes the importance of a medical diagnostic tool for early detection and monitoring of cancer treatment efficacy, such as detection and quantification of apoptotic cells in a patient's blood before and during cancer treatment (Wang et al. 2002). Additionally, this device could be used for the analysis of human blood, such as when differential white blood count is used as an early disease indicator or for detecting and isolating fetal cells from the maternal circulation to test for prenatal genetic analysis as suggested by Holmes et al. (Holmes et al. 2006). The miniaturized detection of apoptosis on a chip could also serve as a novel tool for better understanding cellular signaling pathways and disease. The need for early detection is a goal for clinical diagnoses and future

point-of-care applications (Ahn et al. 2004). With the progression of micro-/nano-technology today, the label-less ability to study apoptosis in single cells in real-time may become a reality.

1.2. Recent Apoptotic Detection Studies Using Microfluidic Platforms

Several of the bench-scale apoptosis assays described in section 1.1 have been adapted for use in microdevices. In general, these studies aim to decrease analysis time, increase sensitivity, consume less reagents and cells, and allow for high-throughput screening. In this chapter, these microfluidic designs are reviewed by the particular cellular or molecular target that forms the basis of the assay.

1.2.1 Mitochondrial Membrane Potential

The mitochondrial membrane potential ($\Delta\Psi_m$) is composed of chemical and electrical components that are involved in electron transport processes and is used as a characteristic indicator of cell health (Kataoka et al. 2005). A microfabricated device was designed for separation of intact and compromised membrane potential mitochondria by using micro-

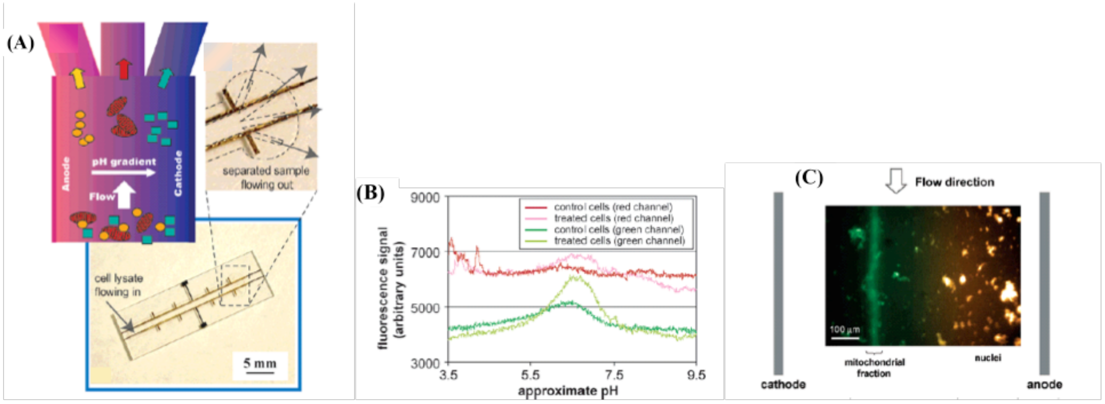

Figure 1.3 Micro-IEF device for separating mitochondria (Lu et al. 2004). (A) Schematic for isoelectric focusing of protein and organelles with a photo showing the microfabricated device. (B) IEF of JC-1 labeled mitochondria from HeLa cells show two subpopulations of organelles (majority of mitochondria have acidic pI (in red channel), while a small population of mitochondria have near neutral pH (visible in green FL channel)). (C) IEF of mitochondria from NR6wt cells lysate stained with MitoTracker Green (distinct narrow band) and propidium iodide (broad band). A pH of 3-6 buffer was used. Mitochondria focused at pI between 4 and 5.

isoelectric focusing (IEF) (Figure 1.3) (Lu et al. 2004). In IEF, a protein molecule is mobilized due to an external electric field and stops migrating when it reaches its isoelectric point (pI) (net charge is zero) due to the pH gradient. This device consists of electroplated gold electrodes (50μm thick) and microfluidic channels in photopatternable epoxy; fabrication of this micro-IEF device included photolithography, thin-film metal deposition/patterning, and electroplating techniques. For detection, potential-sensitive JC-1 dye was used as a quantitative fluorescent marker of mitochondrial membrane potential. For healthy mitochondria that retain their membrane potential, the dye accumulates with formation of J-aggregates and red fluorescence (exc. 535nm/em. 590 nm) while mitochondria that lose their potential show green fluorescence characteristic of the monomers (exc. 485 nm/em. 530nm). The different pIs for intact and compromised $\Delta\Psi_m$ could be used for analyzing cell lysates to determine if the cells lost membrane potential due to apoptosis. While this device provides fast separation in small samples, it would be more ideal to avoid the cell lysis steps required using this approach.

A fluorescence-based microchip has also been used to analyze mitochondrial membrane potential in living cells (Kataoka et al. 2005). $DiOC_6(3)$ (3, 3'-dihexyloxacarbocyanine iodide) fluorophore (exc. 484 nm /em. 501nm) is a green-fluorescent lipophilic, cationic probe used as an indicator of $\Delta\Psi_m$. Baba and colleagues successfully evaluated this fluorescent mitochondrial event using a fluorometer (average fluorescence of the entire sample) and Agilent 2100 Bioanlayzer that uses microchips.

A commercially-available microdevice capable of DYm-based apoptotic detection is the Agilent 2100 Bioanalyzer, which uses disposable microchips coupled with off-chip two-color fluorescence detection (Figure 1.4). Cells are moved by pressure-driven flow in microfluidic channels and are hydrodynamically focused before passing the fluorescence interrogation point.

Each chip contains 6 sample cell wells (10 mL cell sample/well) and networks of microchannels (75 x 25 mm) etched on a glass substrate. When the cell channel and cell buffer channel intersect under laminar flow, cells are "pinched" near one wall of the channel and continue to pass the detector in single file. Light from the blue LED (472 nm) and red laser (635 nm) is focused in the detection area and excites the cells. Photodiodes (510-540 nm and 674-696 nm) are used for detection of fluorescence emitted by the cells. Constant flow rates are ~ 3-4 mm/s, and there are approximately 500-1000 cell events recorded per sample well in 4 min.

The sensitivity of the Agilent 2100 Bioanalyzer for detecting fluorescence is less than a conventional flow cytometer because the Agilent 2100 Bioanalyzer uses a photodiode instead of a photomultiplier tube (PMT). A conventional fluorescent activated cell sorter (FACS) flow cytometer determines fluorescence of single cells, but is very expensive and can be relatively complicated to operate. Also, FACS techniques require cell modification preparation with the

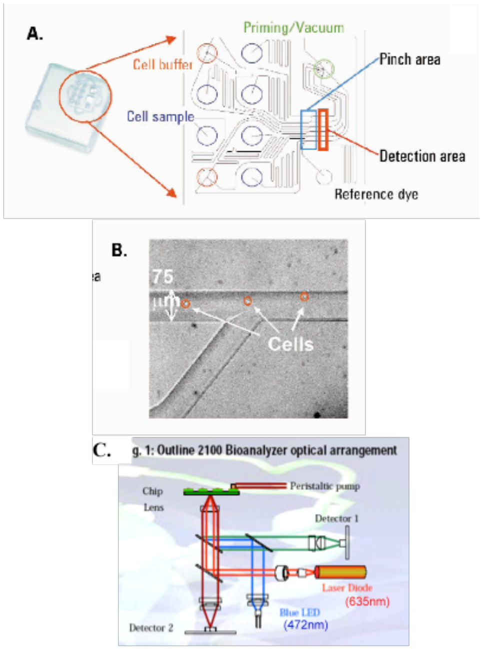

Figure 1.4 Agilent 2100 bioanalyzer lab-on-a-chip (http://www.chem.agilent.com).(A) Schematic showing cell buffer, cell sample, priming solution, and focusing dye wells, (B) Cell channel intersected by cell buffer stream, (C) Optical arrangement in the 2100 Bioanalyzer (Preckel et al.).

use of cell markers and antibodies. The Agilent 2100 Bioanalyzer is easier to operate, relatively inexpensive, and uses less reagents/cells; however, the optics of this system restricts the fluorophores that can be used and still requires expensive dyes and optical components.

1.2.2 Phosphatidylserine (PS) Translocation

Agilent Bioanalyzer 2100 cell chip system was also used to evaluate annexin V-binding in human umbilical vein endothelial cells (HUVECs) and normal human dermal fibroblasts (NHDFs) (Chan et al. 2003). Annexin V-biotin/streptavidin-Cy5 and calcein-AM fluorophores were used to determine the percentages of apoptotic cells in the live calcein cell population and are comparable to conventional flow cytometric data.

1.2.3 DNA Fragmentation

The microfluidic device platform has also been used for the detection of DNA fragmentation in a single cardiomyocyte by electrophoresis (Kleparnik and Horky 2003). Doxorubicin-induced cardiomyopathy (DC) is a life-threatening condition in patients undergoing chemotherapy, where there is an irreversible loss of cardiac myocytes. It is thought that active cell death has a role in the onset of DC, and thus stresses the importance of studying apoptosis in the pathogenesis of DC.

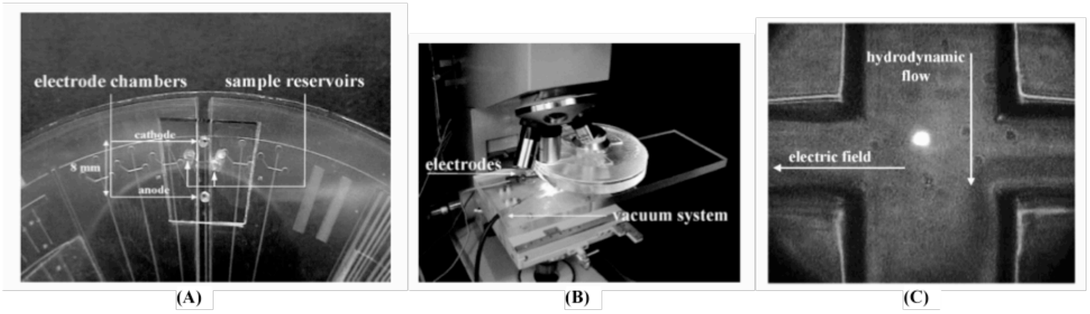

Figure 1.5 (A) Detail of the CD-like plastic microfluidic device- silicon rubber covers the channels of a separation cross, while the holes form the electrode and sample chambers (B) Microfluidic device (with Pt electrodes and glass tubing connecting the vacuum system with one of the sample chambers) mounted on microscope (C) Cells are introduced into the separation cross by negative-pressure-induced hydrodynamic flow (Kleparnik and Horky 2003).

The microfluidic system for resolving DNA fragmentation performs the cell handling in vacuum-driven flow, alkaline cell lysis and denaturing, and electrophoretic separation. Confocal microscopy was used for high-sensitive laser-induced fluorescence (LIF) of the ethidium bromide-labeled DNA fragments. The separation and sample channels were injection-molded in a polycarbonate CD with 50 x 20 μm channel. The microfluidic disc and silicon cover were fastened together by two external plexiglass discs which were fixed in the middle with a screw (Fig. 1.5). Platinum electrodes were inserted in the electrode chambers, and a laboratory vacuum pump was used to move the cells across the channel and was controlled manually by a valve in the vacuum system.

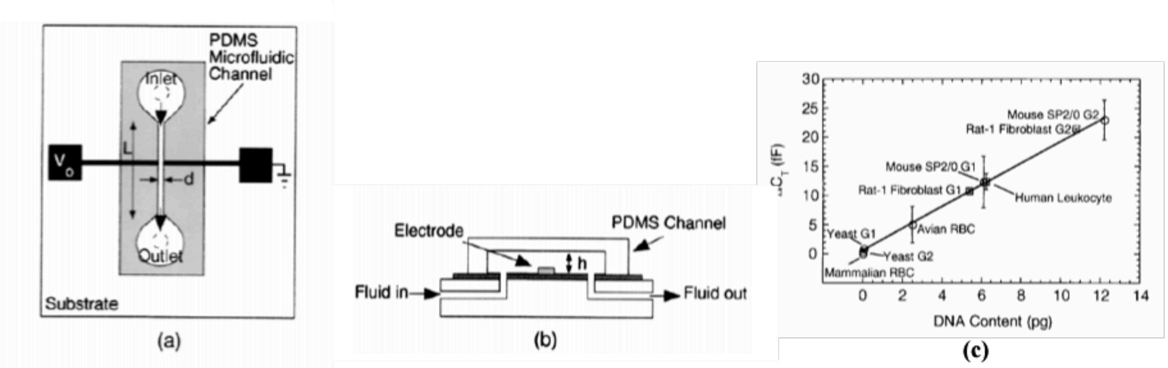

Figure 1.6 Capicitance cytometry- quantifying DNA content of single cells to analyze cell cycle kinetics (Sohn et al. 2000). (A) Top view of the device including electrode configuration, inlet and outlet holes for fluid, and PDMS microfluidic channel (distance (*d*) separating the electrodes is 30 μm, width of the PDMS channel is also 30 μm, L is 5 mm). (B) Side view along the vertical axis shows a view of fluid delivery, which is accomplished with a syringe pump at non-pulsatile rates (1-300 μL/hr). (C) Change in capacitance (ΔC_T) vs. DNA content, which shows a linear relationship at 1-kHz frequency.

Another flow cytometry technique has been employed on the basis of cellular DNA content to detect apoptosis- in which apoptotic cells have less DNA content than live diploid cells. The "capacitance cytometry" technique was based on the observed linear relationship between DNA content of eukaryotic cells and the change in capacitance that is observed when an

individual fixed cell passes across a 1-kHz electric field (Sohn et al. 2000). This microfluidic technique was used to quantify DNA content and analyze cell-cycle kinetics of cell populations, independent of cell species (among yeast, mouse, rat, and human). An AC capacitance measurement is the basis for this microdevice. The change in total capacitance (ΔC_T) across a pair of 30μm-wide microelectrodes is recorded as individual cells flow through the 30μm-wide microfluidic channel (Figure 1.6). The microdevice system was fabricated in a multi-stage process. The gold microelectrodes (50 μm-wide and 30 μm apart) (sensor) are fabricated by photolithography on a glass/quartz substrate, and holes (millimeter-size) were drilled into the substrate to provide an inlet and outlet for the fluid and cells. Soft lithography was used to create a polydimethyl-siloxane (PDMS) microfluidic channel (two heights were used: 30 μm and 40 μm). The height of the gold microelectrodes is not reported. The PDMS channel was aligned over the electrodes and holes, and a syringe pump was used to deliver fluid. The capacitance was measured by a commercial capacitance bridge at a frequency of 1 kHz. There is no documentation on the use of live cells with this device nor is there data to show that the signal of this device could be a function of cell viability.

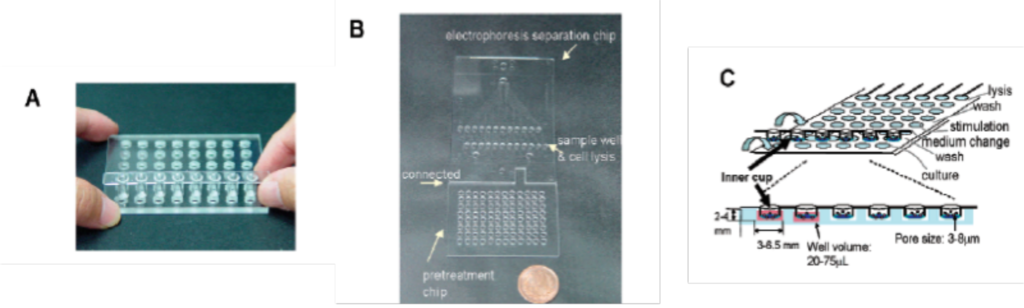

Figure 1.7 Self-contained on-chip cell culture and pretreatment system with (A) 48-well microdevice integrating cell culture, washing, stimulation, lysis, immunoassays (Nisshin Medical Instrument), (B) 96-well microchip by Nisshin Medical Instrument connected to electrophoresis separation chip (Hitachi Chemical), and (C) Proposed cell culture microdevice incorporating all three devices (Tabuchi and Baba 2004).

1.2.4 Caspase Activity

A self-contained on-chip system and pretreatment microdevice system was developed and used for detection of caspase-3 expression in Jurkat cells (Tabuchi and Baba 2004). The novel cell culture system was based on two existing integrated cell culture microdevices. The new system consists of an acrylic plate drilled with 48-96 holes (5-6.5 mm diameter), and an “inner cup” (8-well strip) was modified with a 3-8 μm pore-polycarbonate membrane (Figure 1.7). The inner cup, which was manipulated with a wire, was inserted into the microdevice wells. This device avoids the labor-intensive pipetting and centrifugation steps involved in cell preparation. In the last cell culture treatment step, the cell lysis buffer is added, and the soluble protein precipitates through the membrane (out of the insert cup) into the well. The protein precipitate is then isolated to be used for detection analysis in a commercial electrophoresis separation chip, and the sample can be readily introduced from the pretreatment system to the electrophoresis separation channel by a pressurization (sample injection) technique.

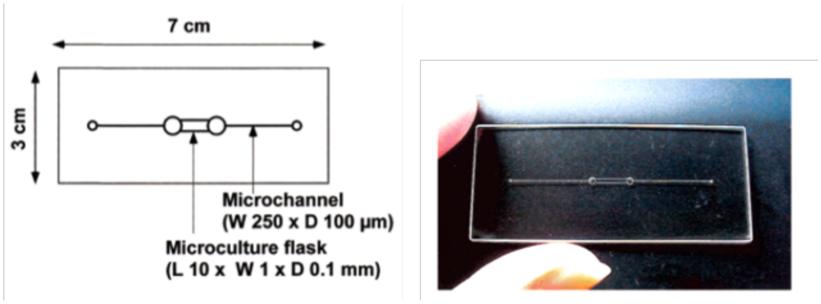

Figure 1.8 Micro-chip based system for monitoring cytochrome c release using TLM (Tamaki et al. 2002).

The heat-treated Jurkat cells reported here were evaluated for caspase activity (incubation with anti-caspase-3-antibody) and phosphatidylserine (incubation with annexin V-biotin/streptavidin-Cy5) by obtaining electrophoretic separation of the stress-induced proteins

(electropherograms) from the protein assay. While this self-contained, pre-treatment system is convenient for avoiding the cell prep steps, another method is discussed later in the future proposed project which proposes to detect apoptosis, without requiring the preparation of extra reagents, use of wash steps, or need for lysing cells.

1.2.5 Release of Cytochrome c

The release of cytochrome c from the mitochondria to the cytosol, which is another hallmark event of apoptosis, has been evaluated on the microfluidic chip platform. The scanning thermal lens microscope (TLM) detection system and cell culture microchip (microflask) was developed for detecting a non-fluorescent biological substance in a neuroblastoma-glioma (NG-108-15) hybrid cell (Tamaki et al. 2002). The cell chip was composed of three quartz glass plates (30 mm x 70 mm) with two small access holes for inlet and outlet (Figure 1.8). Microchannels (250 μm width, 100 μm deep) and the microculture flask (100 μm deep, 1mm wide, 1 cm long (1μL volume)) were made using an intensified CO_2 laser beam. The three plates were polished and laminated together. The amount of cytochrome c detected was estimated to be as low as 10^{-20} mol.

The fluorescent image of the cell stained with MitoTracker Green in Fig. 1.9(A) shows the distribution of mitochondria in a live cell. Cytochrome c (cyt c), which is non-fluorescent and unable to be visualized by fluorescent microscopy, is found in the mitochondria of live cells and should be located outside the nucleus. The cyt c distribution in a live cell is assumed to be similar to the mitochondria distribution as per the similarity they observed in Fig. 1.9 (A) and (B). Therefore, the authors find it reasonable to consider the higher intensity signal is mainly related to the cyt c localized in the mitochondria. The distribution of the signal intensities indicates a diffusion of cyt into the cytosol during apoptosis (Fig. 1.9 (C)). Several assumptions

were made by this group to extrapolate from the fluorescent image to the claims in the TLM imaging. While the TLM excitation beam was selected to be 532nm (where cyt c has strong absorption, ε~10,000), it is still possible that other cell components were also detected simultaneously when the signal intensities were acquired. Also, it would be difficult to obtain real-time measurements with this system due to the amount of time required for scanning. The authors claim that they are able to directly monitor the amount of cytochrome c in an intact live cell undergoing apoptosis without using any expensive fluorophores; however, it is an indirect measurement at best, and there is no verification that it is definitely cytochrome c being visualized.

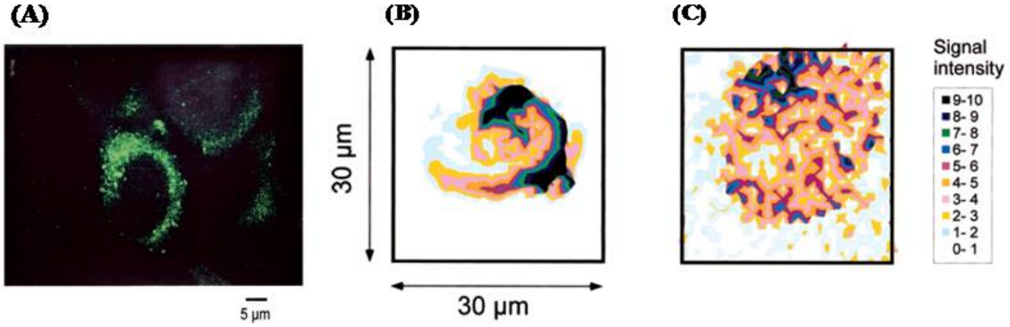

Figure 1.9 (A) Fluorescent image of mitochondria in live neuroblastoma-glioma cell stained by MitoTracker Green. Scanning thermal lens microscopy images of a single cell (B) before apoptosis and (C) 4 hr after staurosporine-induced apoptosis (Tamaki et al. 2002).

1.2.6 Intracellular Calcium (Ca^{2+}) Detection

There are changes in the cytosolic Ca^{2+} concentration and intracellular Ca^{2+} concentration during the apoptosis cascade of events. A microfluidic device was developed to monitor the apoptosis-associated Ca^{2+} fluxes (Wheeler et al. 2003). The microchip was constructed from poly(dimethylsiloxane)(PDMS) for monitoring the intracellular Ca^{2+} levels of a single cell (Jurkat cell). A micro-“dock” was fabricated on the chip to capture or trap a single cell for monitoring with trypan blue dye (Figure 1.10). Another microchip was developed for real-time

monitoring of cellular Ca^{2+} uptake in HL-60 cells using a calcium binding dye (Fluo 3-AM) (Yang et al. 2002).

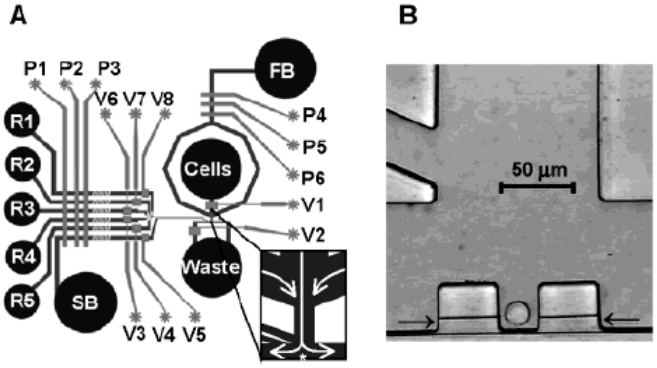

Figure 1.10 Microfluidic cell trapping chip for measuring intracellular calcium ion concentration of a single cell (Wheeler et al. 2003). (A) Schematic of device which includes SB (shield buffer) and FB (focusing buffer) inlets, valves which are actuated by applying pressure to control inlets (V1-V8), pumps (P1-P3 or P4-P6) which are activated. (B) CCD image of an individual Jurkat cell trapped in the cell dock.

1.3 Electroanalytical Methods and Apoptosis

Electrochemical methods have various advantages over the label assays described in section 1.2, such as minimal cell manipulation, reduced cell preparation/cost of reagents, potential for automation, amenability for miniaturization, ease for real-time monitoring, and sensitivity of detection. In this chapter, relevant electrochemical properties are defined, followed by their applications in cell-based detection. Electrochemical methods provide a non-invasive means of detecting and quantifying cell properties, such as cell size, membrane capacitance, and cytoplasm conductivity as a function of frequency (Cheung et al. 2005). Electrochemical cell diagnostic applications have advanced considerably since the first electrodes were incorporated into a microfluidic device (Ayliffe et al. 1999). Electrical methods are easily integrated in microfluidics and show much promise due to their relatively simpler and cheaper peripheral equipment (Yi et al. 2006a). Incorporation of this instrument at the microscale costs ($4,000-

$5,000) for the electrochemical method are the lowest compared to optical and mass spectrometric (MS) equipment ($50,000 to 250,000) (Yi et al. 2006b).

1.3.1 Electrochemical Properties of Eukaryotic Biological Cells

Dielectrophoresis is the movement of polarizable particles that are placed in a non-uniform electrical field and is based on the difference in permittivities of the particles and surrounding media (Jones 1995; Pohl 1951; Wang et al. 2002). A cell has a dielectric constant that is significantly different than the surrounding buffer. Cellular DEP responses are studied as a function of the applied electric field, allowing for single-cell discrimination of cell membrane capacitance and conductivity. Table 1.1 includes a list of parameters that are commonly used for assigning conductivities and permittivities of cells and buffer solutions.

The eukaryotic biological cell is typically modeled as a spherical particle with a conductive cytoplasm and capacitive cell membrane (conductance of gm assumed to be negligible) (Fig. 1.12). The induced charge is not uniformly distributed across the cell; rather it is an induced dipole, and is dependent on the relative polarizability of the particle with respect to the surrounding media.

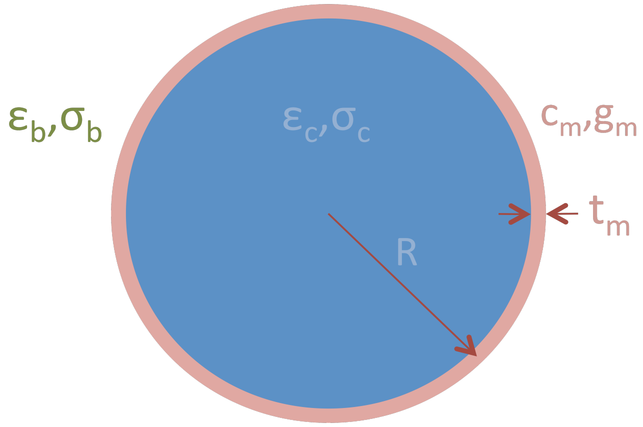

Figure 1.11 Electrical parameters of cell with radius (R) include thin membrane (t_m), lipid bilayer capacitance C_m and conductance G_m, conductivity and permittivity of cytoplasm (σ_c, ε_c) and surrounding buffer solution (σ_b, ε_b)

Table 1.1 Dielectric parameters used for characterizing cell and buffer solutions

Cell dimensions		
Membrane thickness	4-10nm	(Markx and Davey 1999)
Capacitance of cell membrane	0.5 μF/cm^2	(Pethig and Kell 1987)
Conductivities		
Cell membrane	10^{-8} – 10^{-4} S/m	(Markx and Davey 1999)
Cell cytoplasm	2-10 S/m	(Markx and Davey 1999)
DI water	0.15 mS/m	(Durr et al. 2003)
Polystyrene (-COOH) bead	0.8 mS/m	(Demierre et al. 2007)
1mM PBS	1.4 mS/m	(Demierre et al. 2007)
Relative Permittivities		
DI water	79-80	(Markx and Davey 1999)
Cell membrane	2-10	(Markx and Davey 1999)
Cell cytoplasm	50-120	(Markx and Davey 1999)
Polystyrene (-COOH) bead	3.5	(Durr et al. 2003))

The DEP force (F_{DEP}) acting on a spherical particle in a buffer solution is a function of the radius of the particle, applied electric field, and permittivity of the cell and surrounding medium and is given by the following equation (Jones 1995).

$$F_{DEP} = 2\pi R^3 \varepsilon_b \, \mathrm{Re}[f_{CM}] \nabla E^2 \qquad \text{(Eq. 1.1)}$$

where, R= radius of particle,
ε_b= permittivity of the buffer,
∇E^2= electric field applied (proportional to gradient and strength of applied field),
$\mathrm{Re}[f_{CM}]$= Real part of the Clausius-Mossotti factor

The Clausius-Mossotti (f_{CM}) factor is a frequency-dependent parameter that is a measure of the dielectric contrast between particle and medium and depends on the cell's membrane properties or shape (Jones 1995). The Clausius-Mossoti factor is proportional to the dielectrophoretic force.

$$f_{CM}=\varepsilon^*_p-\varepsilon^*_b/\varepsilon^*_p+2\varepsilon^*_b \qquad \text{(Eq. 1.2)}$$

where ε^*_p, ε^*_b = complex permittivity of particle buffer ($\varepsilon^*=\varepsilon-j(\sigma/\omega)$),
σ = conductivity
ω = angular frequency of electrical field

Assuming the imaginary components do not contribute to F_{DEP}, the remaining Real part of f_{CM} is: $\mathrm{Re}[f_{CM}] = \dfrac{\varepsilon_p - \varepsilon_b}{\varepsilon_p + 2\varepsilon_b}$

The Re [f_{CM}] determines the effective polarizability of the particle. This polarizability parameter varies as a function of the frequency of the applied field and depends on the particle and buffer dielectric properties (value ranging between +1 and -0.5). If the particle is more polarizable than the medium, Re [f_{CM}] > 0, the particle is attracted to the high intensity electric field regions and undergoes positive DEP (pDEP). Also, if the particle is less polarizable than the medium, Re [f_{CM}] <0, the particle is repelled from the high intensity electric field regions and undergoes negative DEP (nDEP). The DEP crossover frequency is the frequency where the DEP force switches from pDEP to nDEP and vice versa. DEP crossover frequency and measured cell radius in a known conductivity medium can be used to approximate cell membrane capacitance and conductance values (Wang et al. 2002). Pethig et al. have described how a dying cell undergoes important changes in its dielectric properties (Pethig and Markx 1997). The cell membrane consists of the lipid bilayer, which contains many proteins and is highly insulating while the cell interior contains membrane-covered particulates (mitochondria, vacuoles, nucleus, and dissolved charged molecules). The conductivity of the cell interior (1 S/m) is 10^7 times more conductive than the cell membrane (10^{-7} S/m) (Pethig and Markx 1997). Upon cell death, a necrotic cell's membrane becomes permeable, and its conductivity increases by a factor of 10^4 as the cell contents are dispersed into the surrounding medium. Therefore, cell death is associated with a large change in dielectric properties, thus also a large change in dielectric polarizability.

Membrane capacitance describes the area of the membrane that acts as a barrier and can accumulate ionic species in response to the applied electric field, while the membrane conductance is a measure of the net transport of ionic species through pores and ion channels,

which is influenced by applied electric field. Alterations in the DEP properties, the "dielectric-phenotype", which are related to capacitance and conductivity of membrane, cell size, and intracellular components have been described for apoptotic and necrotic cells and demonstrate potential for applications related to quantification of the apoptotic process (Wang et al. 2002). Alterations in cytoplasm conductivity, membrane capacitance, and dielectrophoretic properties have also been studied for cells (HL-60, K562, and adherent cell lines) undergoing apoptosis as discussed later in this chapter (Labeed et al. 2006) (Arndt et al. 2004) (Wang et al. 2002). The biophysical properties of the cell membrane and cytoplasm of apoptotic cells is discussed in section 1.3, where an increase in cytoplasm conductivity and membrane capacitance and loss of cell volume are reported (Labeed et al. 2006).

1.3.2 Electrochemical Detection Methods

1.3.2.1 Impedance Spectroscopy and Micro Flow Cytometry

Renaud and colleagues demonstrated a label-free differentiation of particles and red blood cells (RBCs) in an on-chip cytometer using impedance spectroscopy for detection (Cheung et al. 2005). Polystyrene beads and RBCs in 5mM PBS were measured individually at a rate of 1,000 cells/minute in the frequency range of 350 kHz to 20 MHz in the micro-flow cytometer. The microfluidic channel included focusing electrodes, measurement electrodes, and sorting electrodes as seen in Figure 1.12(A). The "measurement" area has a 20x40 μm^2 cross-section, and the electrodes are 30 μm wide. The amplitude and phase information was used to separate the cells based on their dielectric properties. A correlation plot is shown for the separation of particles based on simultaneous measurements at a reference frequency of 602 kHz and high frequency of 10 MHz (Figure 1.12(B)). While this has yet to be shown, this microfabricated tool could be taken one step further and used in applications to characterize and detect early-stage

apoptotic cells, such as the "cell trap" micro-system that was studied using an optical detection system as shown in Figure 1.13 (Valero et al. 2005). A microfluidic "cell-trap" device that manipulates cells by electroosmotic flow (EOF) was one of the first devices used to study apoptosis at the single-cell level. Cell discrimination was determined by fluorescence microscopy by imaging PI (membrane integrity indicator) and FLICA (blocks the activation of caspases) as the cells became localized in the trap (Fig. 1.13(b)). Thus, it is apparent how this device could be extrapolated upon to incorporate impedance measurements along with the fluorescent measurements if microelectrodes were incorporated in the trap region.

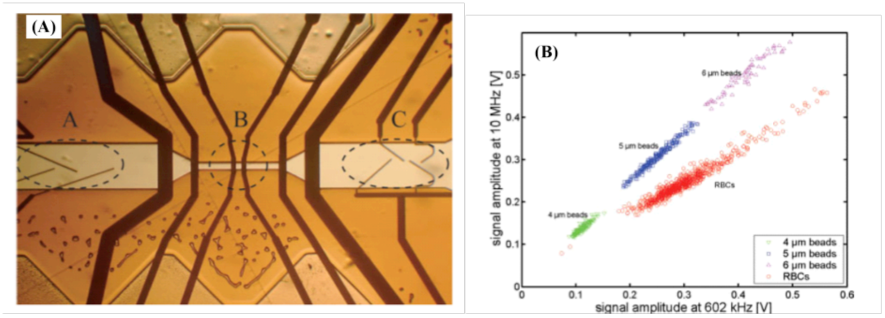

Figure 1.12 Microfluidic channel and microelectrodes used in the impedance spectroscopy flow cytometer (Cheung et al. 2005). (A) Close-up view of the microfluidic channel and electrodes [A. Focusing electrodes, B. Measurement electrodes, C. Sorting electrodes]. (B) Correlation plot of the impedance measurements for different size microparticles and red blood cells (RBCs)

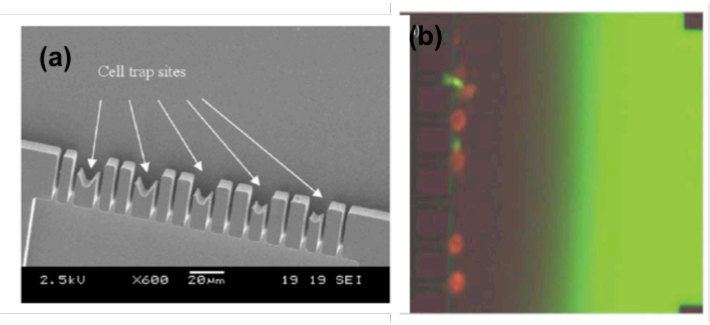

Figure 1.13 (A) SEM image of a microfluidic cell trap device for studying apoptotic cell death in HL-60 cells; (B) Fluorescent image showing how apoptotic cells were identified (Valero et al. 2005).

Bioelectrical impedance has also been used to successfully monitor apoptosis based on changes in cell shape of immobilized adherent endothelial cells (Arndt et al. 2004). Changes in cell shape were measured as adherent cells were grown on planar gold-film electrodes (d=2mm) for ECIS (electric cell-substrate impedance sensing) measurements from 1Hz to 1MHz. The ECIS measurements based on the 3D shape of the cells was more sensitive than the caspase-3 activity assay or structural changes in cell-cell contacts. This technique was successful in monitoring the dynamics of apoptosis in a cell monolayer, though this particular method will not lend itself to single-cell measurements or suspension cell applications.

Electrochemical impedance measurements were used to discriminate between different cell types and particle sizes with rates exceeding 100 samples/second on a single-cell basis (Gawad et al. 2001). The microdevice was based on the micro-Coulter particle counter principle and consisted of a glass-polyimide chip with integrated channels and electrodes microfabricated according to the size of the particles investigated (1-20 μm) (Fig. 1.14 (a) (b)). A differential pair of microelectrodes along with an HP 4284A precision LCR meter, was used to record each cell's impedance signal while using the surrounding media as a reference. The system was able to record simultaneous impedance measurements at multiple frequencies (100 kHz to 15 MHz). Calibrated latex beads (diameters of 5 and 8 μm), human erythrocytes, and erythrocyte ghost cells (without their internal content) in standard PBS (conductance of ~ 1.6 S/m) were used in the microchip device (Figure 1.14(c)). Several cell assumptions were made for the simulations that were performed to compare different electrode geometries. The cell was assumed to be a uniform, sphere with cytoplasm conductivity (σ_c~0.5 S/m) surrounded by a thin, non-conductive membrane with capacitance (1μF/cm^2) and resistance of the surrounding PBS related to the conductivity of the PBS solution (σ_{sol}~1.6 S/m). This non-optical tool could have applications in

oncology, haematology, or toxicology. The impedance spectroscopy microchip device is limited by its planar electrode design, and no studies were conducted using this device for applications beyond particle sizing and counting, such as for cell viability detection or monitoring of apoptotic cell populations.

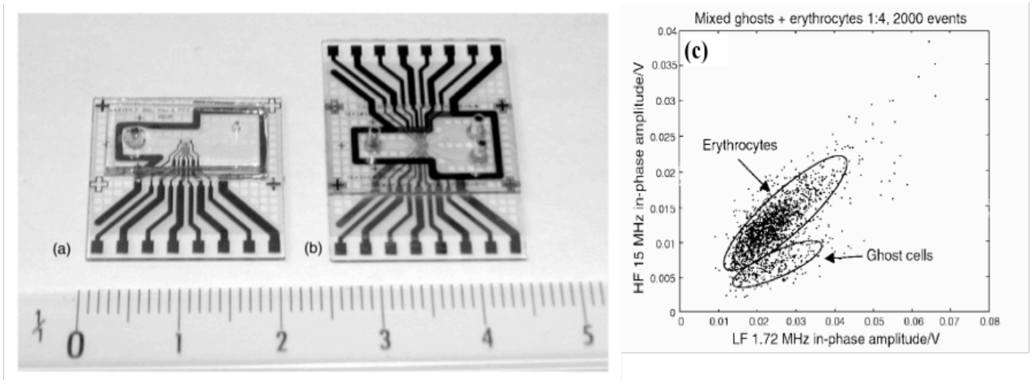

Figure 1.14 (A) Microfabricated chip with PDMS cover. (B) Chip-on-chip configuration with electrodes on the bottom with an experimental sorting chamber. (C) Ghost cells and erythrocytes are discriminated in a correlation plot, where ghost cell cytoplasm conductance has a lower HF/LF ratio similar to the buffer solution (Gawad et al. 2001).

Additional work has been reported that using impedance spectroscopy for cell detection and counting using cell lysate in a microfluidic device (Cheng et al. 2007). The microdevice consists of top and bottom slides (75mmx25mm) bonded to 50um thick PDMS gaskets with an opening of 5cm x 4mm forming closed microfluidic channels. Gold electrodes were constructed with standard photolithography and gold wet etching. Three different electrode designs were studied (interdigitated (IDT) co-planar(3.8mmx15um with 35um gaps), simple two-rail co-planar (100um wide with 3.8mm spacing), and top- and bottom- (5cm-4mm gold pads) electrodes) (Fig. 1.15). Low-conductive buffer (8.5% sucrose and 0.3% dextrose) was used to flow the peripheral blood mononuclear cells (PBMCs) into the device for targeted cell capture. Cells are then lysed to release intracellular ions, which are monitored using surface patterned electrodes and impedance spectroscopy (LCR meter) to detect cell numbers. This study found that the

impedance magnitude at 760Hz (measured using an Agilent 4284 LCR meter) is a function of number of cells captured on-chip and was able to detect as few as 20 cells/mL. This study was successfully able to measure bulk cell concentration using impedance spectroscopy, though lacked the single-cell detection of whole cells that is described in Chapter 4.

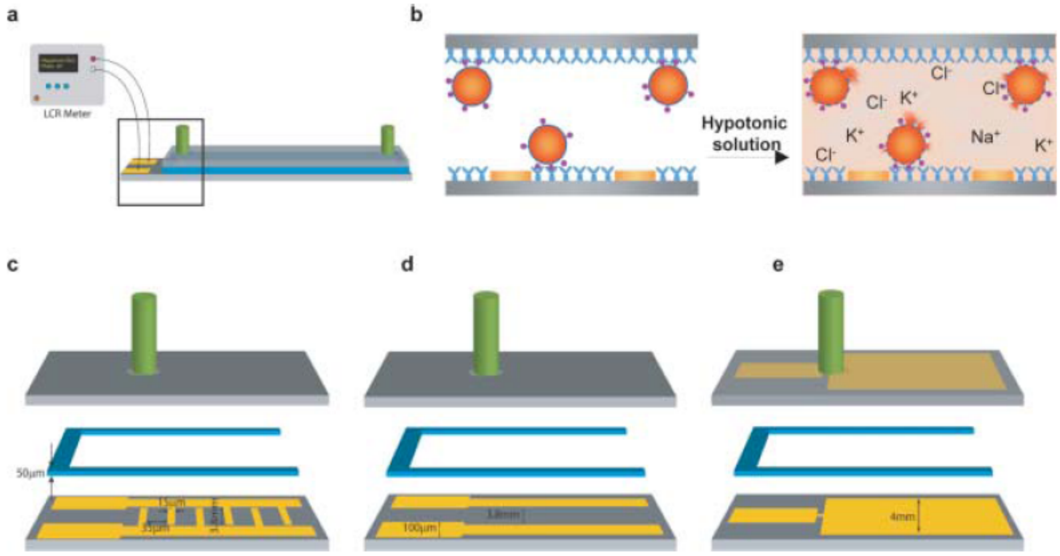

Figure 1.15 (A) Schematic drawing of impedance measurement (LCR meter, green port is inlet), (B) Representation showing targeted cell isolation on-chip, cell lysis, cell ion release, which increases bulk conductance, and uses surface electrodes to measure impedance spectroscope to detect cell concentration, (C) interdigitated (IDT) co-planar electrodes, (D) simple 2-rail co-planar electrodes, (E) top-bottom electrodes (PDMS gaskets are blue). (Cheng et al. 2007)

1.3.2.2 Voltammetric Method and Apoptosis (Bulk Cell Measurements)

A voltammetric method was used to study apoptosis in K562 cells using a small flow chamber (100uL) assembled with a 3-electrode system (edge-oriented graphite 0.196 cm^2 working electrode on the ceiling) and CHI model 600 voltammetric analyzer (Feng et al. 1999). Cells ($2x10^6$ cells/mL) in PBS flowed through the channel for measurement of faradic response (peak current), and a DNA fragmentation assay was used for verification of apoptosis-induced cells (Vp16 (4'-demethylepipodophylotoxin-β-D-ethylidone-pyranoglucoside)- apoptosis-

inducing agent). The results of this study show that the measured decrease in faradic response of apoptotic cells is related to the electrochemical activity of cells that is altered during apoptosis. The flow rate of the cells through the flow chamber is not reported, and it appears that the figures are based on bulk cell measurements over time- though it in unclear from the description of the experimental setup. The significance of this voltammetric method is relevant for future electrochemical detection methods and shows potential for being able to sensitively monitor apoptosis in the early stages (Feng et al. 1999) .

1.3.2.3 DEP and Apoptosis

Dielectrophoretic techniques have been demonstrated to have potential for detecting and quantifying normal, apoptotic, and necrotic cells using a human myelogenous leukemia cell line (HL-60) (Wang et al. 2002). The cell membrane was the main focus for its early role in participating in apoptosis. Genistein (GEN) was used to induce apoptosis as it is a topoisomerase and tyrosine protein kinase inhibitor, which induces apoptosis at all phases of the HL-60 cell cycle. The annexin V assay and appearance of the sub-G1 cell subpopulation were used as indicators of apoptosis. An electrode chamber and glass substrate were used with a DEP electrode array (HP 8116A applied 3-V-pk-to-pk sinusoidal signal). Observing the cells and measuring their diameters under a microscope, the crossover frequency of randomly selected cells was determined by the frequency at which their DEP-induced motion changed direction, with 20 cells studied for each treatment in less than 20min.The morphology of the cell membrane was monitored by scanning electron microscopy (SEM) imaging and changes in membrane capacitance. As the cells began forming “blebs,” there was an increase in smooth areas on the surface of the membrane over a four-hour time-frame (Fig. 1.16). The increase in smooth areas was suggested to be a result of a loss of microvilli and other membrane features. The decreased

morphological complexity correlated with the observed decrease in membrane capacitance as the cells progressed through apoptosis. The crossover frequencies for the necrotic (trypan-blue positive) HL-60 cells were in the megahertz range and widely different from the live control and apoptotic control cell populations as shown in Fig. 1.17 (Wang et al. 2002).

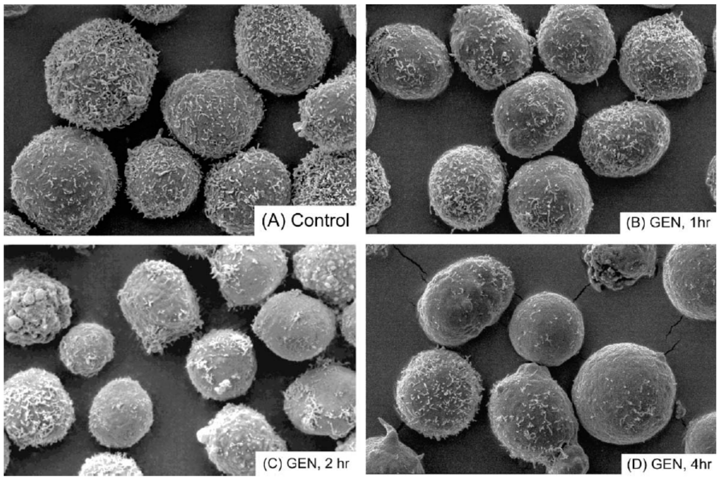

Figure 1.16 SEM images of HL-60 cells following apoptotic inducer (genistein (GEN)) treatment that reveal changes in the membrane morphology with apoptosis (A) control, (B) 1hr, (C) 2 hr, and (D) 4 hr-GEN treatment (magnification x2500) (Wang et al. 2002).

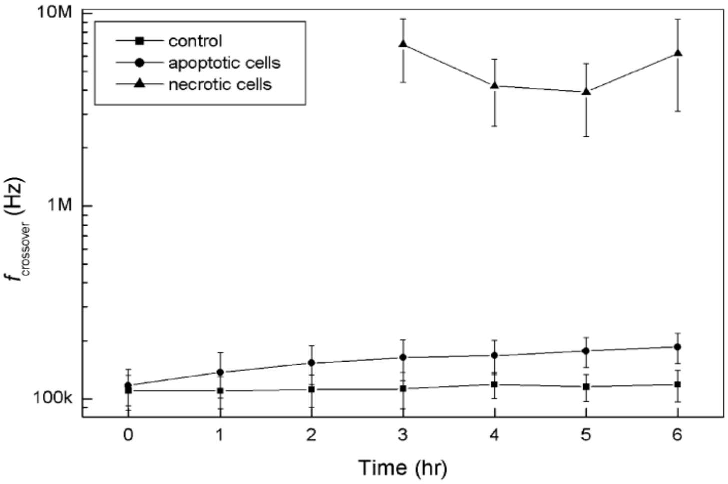

Figure 1.17 Differences in crossover frequencies of live, necrotic, and apoptotic cells after inducing apoptosis (Wang et al. 2002).

Dielectrophoresis was also used to determine the dielectric properties of human chronic myelogeneous leukaemic (K562) cells during apoptosis (Labeed et al. 2006). The cells ($3x10^5$ cells/mL) were placed in petri dish with 5mS/m isotonic buffer (8.5% (w/v) sucrose, 0.3% (w/v) dextrose, and PBS), and while observing with microscope/video camera/monitor, the authors counted the cells as they collected at the electrodes for a period of 1 min. For the DEP measurements, signals of 10Vpk-pk and frequencies between 5kHz and 20 MHz (at 5 frequencies/decade) were used. Staurosporine was used as the inducing agent, and an AnnexinV-FITC/PI and TMRE (tetramethylrhodamine ethylester- a cationic, lipophilic dye that accumulates in negatively charged mithochondrial matrix) assay were used to verify apoptosis. Early apoptotic cells were observed to undergo an increase in cytoplasm conductivity (0.28 to 0.50 S/m), loss of cell volume, and increase in membrane capacitance (9.7 to 20 mF/m^2). This data is based on single-cell measurements that were manually collected, and the number of cells for each treatment is not directly stated. The data is reported as an average of 6 experiments. Also, the role ion efflux (loss of K+ and Na+ ions) during early apoptosis is discussed. The biophysical parameters (DEP results) of the K562 cells were determined by applying the collected data with best-fit modeling using the single-shell model (Irimajiri et al. 1979). This study shows that dielectric properties of cells differ among multiple cell populations and can be used to assess different stages of apoptosis.

A review of current literature in the area of cell viability and microfluidic platforms has been presented. Also, electrochemical properties of eukaryotic cells and dielectric changes involved in cell viability have brought much attention to the dielectric differences that have been reported for live, apoptotic, and necrotic cells. However, there is still no published account of impedance-based, label-free, single-cell viability detection of flowing cells on a chip.

1.4 Specific Aims

The goal of this project was to combine molecular and microdevice methods to characterize and quantify viability of single cells. Fluorescent-based assays were optimized for adherent HeLa and suspension Jurkat cells and were used as a tool for validation of a microfabricated diagnostic device. Cell and substrate/surface interactions were considered for designing a microfluidic device that can be used to characterize cell viability for quantitative biomedical and cell biology applications, which require label-free, real-time monitoring of cells. The aims of the project were as follows:

1.4.1 Aim 1: Evaluate Flow-based Methods for Cell Viability Using Flow Cytometry

Fluorescent probes and time-course experiments were optimized to discriminate non-fixed live, necrotic, and apoptotic cells using flow cytometry. These flow-based assays were successfully used to determine the thresholds of UVA photoactivating light that biological cells can withstand during photoactivation studies (Forman et al. 2007). This flow-based assay was also applied for investigating post-thaw viability and apoptotic response of cells in the presence and absence of gold nanoparticles and a commonly used cryoprotectant, dimethylsulfoxide (DMSO) (Thirumala et al. 2007).

1.4.2 Aim 2: Determine Quantification of Cell-substrate Interactions and Cell Viability Using Light and Fluorescent Microscopy

Expanding upon the flow-based, fluorescent assays described in Aim 1, Jurkat cell viability in defined media and polymer substrates was evaluated using light and fluorescent microscopy. Brightfield light microscopy and cell viability (MTT and CalceinAM) assays were used to characterize the adhesive behavior of Jurkat cells in various media on tissue-treated and untreated polystyrene surfaces. This study explored Jurkat cell responses on deposited polymer

surfaces to study the viability and adhesion of these cells in response to differing substrate materials.

1.4.3 Aim 3: Design a Microfluidic Device for Discrimination of Cell Viability Using Fluorescence and Electroanalytical Methods

Finally, work was done to fabricate a PMMA microchip that is designed specifically for Jurkat cells (~12um in diameter), which were characterized with different polymer substrates as discussed in Aim 2. The spherical morphology and inherent suspension-nature of the Jurkat cell line deemed it to be a good candidate for flow-based, microfluidic applications. The fluorescent microscopy cell viability assay that was optimized for the Jurkat cells in Aim 1 was the tool used for validation of impedance-based cell viability measurements. The integrated microelectrodes were characterized as follows: highly conductive (Pt wire), 76 um in diameter, uniform cross-section aligned with 50 um-wide microchannel that can be interfaced with electrical connections (outside of the chip) to the impedance analyzer.

Completion of these aims establish the proof-of-concept for electroanalytical quantification and characterization of cell viability, which could be used as a platform for various label-free cell biology applications beyond apoptosis, such as identifying cell phenotype/behavior or evaluation of nanotechnology-related applications that are beyond the resolution and capabilities of optical techniques.

1.5 References

Ahn CH, Choi JW, Beaucage G, Nevin JH, Lee JB, Puntambekar A, Lee JY. 2004. Disposable Smart lab on a chip for point-of-care clinical diagnostics. Proceedings of the Ieee 92(1):154-173.

Arndt S, Seebach J, Psathaki K, Galla HJ, Wegener J. 2004. Bioelectrical impedance assay to monitor changes in cell shape during apoptosis. Biosensors & Bioelectronics 19(6):583-594.

Ayliffe HE, Frazier AB, Rabbitt RD. 1999. Electric impedance spectroscopy using microchannels with integrated metal electrodes. Journal of Microelectromechanical Systems 8(1):50-57.

Borisenko GG, Matsura T, Liu SX, Tyurin VA, Jiang JF, Serinkan FB, Kagan VE. 2003. Macrophage recognition of externalized phosphatidylserine and phagocytosis of apoptotic Jurkat cells - existence of a threshold. Archives of Biochemistry and Biophysics 413(1):41-52.

Chan SDH, Luedke G, Valer M, Buhlmann C, Preckel T. 2003. Cytometric analysis of protein expression and apoptosis in human primary cells with a novel microfluidic chip-based system. Cytometry Part A 55A(2):119-125.

Cheng X, Liu YS, Irimia D, Demirci U, Yang LJ, Zamir L, Rodriguez WR, Toner M, Bashir R. 2007. Cell detection and counting through cell lysate impedance spectroscopy in microfluidic devices. Lab on a Chip 7(6):746-755.

Cheung K, Gawad S, Renaud P. 2005. Impedance spectroscopy flow cytometry: On-chip label-free cell differentiation. Cytometry Part A 65A(2):124-132.

Demierre N, Braschler T, Linderholm P, Seger U, van Lintel H, Renaud P. 2007. Characterization and optimization of liquid electrodes for lateral dielectrophoresis. Lab on a Chip 7(3):355-365.

Durr M, Kentsch J, Muller T, Schnelle T, Stelzle M. 2003. Microdevices for manipulation and accumulation of micro- and nanoparticles by dielectrophoresis. Electrophoresis 24(4):722-731.

Fadok VA, Voelker DR, Campbell PA, Cohen JJ, Bratton DL, Henson PM. 1992. Exposure of phosphatidylserine on the surface of apoptotic lymphocytes triggers specific recognition and removal by macrophages. Journal of Immunology 148(7):2207-2216.

Feng J, Cheng K, Luo GA, Wang RJ, Wang DB. 1999. A voltammetric method for analyzing the apoptosis of K562 cells. Analytical Communications 36(11-12):379-381.

Forman J, Dietrich M, Monroe WT. 2007. Photobiological and thermal effects of photoactivating UVA light doses on cell cultures. Photochemical & Photobiological Sciences 6(6):649-658.

Galloway M, Stryjewski W, Henry A, Ford SM, Llopis S, McCarley RL, Soper SA. 2002. Contact conductivity detection in poly(methyl methacylate)-based microfluidic devices for analysis of mono- and polyanionic molecules. Analytical Chemistry 74(10):2407-2415.

Gawad S, Schild L, Renaud P. 2001. Micromachined impedance spectroscopy flow cytometer for cell analysis and particle sizing. Lab on a Chip 1(1):76-82.

Gomez R, Bashir R, Sarikaya A, Ladisch MR, Sturgis J, Robinson JP, Geng T, Bhunia AK, Apple HL, Wereley S. 2001. Microfluidic Biochip for Impedance Spectroscopy of Biological Species. Biomedical Microdevices 3:201-209.

Hanshaw RG, Smith BD. 2005. New reagents for phosphatidylserine recognition and detection of apoptosis. Bioorganic & Medicinal Chemistry 13(17):5035-5042.

Holmes D, Morgan H, Green NG. 2006. High throughput particle analysis: combining dielectrophoretic particle focussing with confocal optical detection. Biosens Bioelectron 21(8):1621-30.

Irimajiri A, Hanai T, Inouye A. 1979. Dielectric theory of multi-stratified shell-model with its application to a lymphoma cell. Journal of Theoretical Biology 78(2):251-269.

Jiguet S, Bertsch A, Hofmann H, Renaud P. 2005. Conductive SU8 photoresist for microfabrication. Advanced Functional Materials 15(9):1511-1516.

Jones TB. 1995. Electrical forces and torques on bioparticles. Electrostatics 1995. p 135-144.

Kataoka M, Fukura Y, Shinohara Y, Baba Y. 2005. Analysis of mitochondrial membrane potential in the cells by microchip flow cytometry. Electrophoresis 26(15):3025-3031.

Kerr JFR, Wyllie AH, Currie AR. 1972. Apoptosis - Basic Biological Phenomenon with Wide-Ranging Implications in Tissue Kinetics. British Journal of Cancer 26(4):239-257.

Kleparnik K, Horky M. 2003. Detection of DNA fragmentation in a single apoptotic cardiomyocyte by electrophoresis on a microfluidic device. Electrophoresis 24(21):3778-83.

Koopman G, Reutelingsperger CPM, Kuijten GAM, Keehnen RMJ, Pals ST, Vanoers MHJ. 1994. Annexin-V for Flow Cytometric Detection of Phosphatidylserine Expression on B-Cells Undergoing Apoptosis. Blood 84(5):1415-1420.

Labeed FH, Coley HM, Hughes MP. 2006. Differences in the biophysical properties of membrane and cytoplasm of apoptotic cells revealed using dielectrophoresis. Biochimica Et Biophysica Acta-General Subjects 1760(6):922-929.

Leite M, Quinta-Costa M, Leite PS, Guimaraes JE. 1999. Critical evaluation of techniques to detect and measure cell death - study in a model of UV radiation of the leukaemic cell line HL60. Analytical Cellular Pathology 19(3-4):139-151.

Lu H, Gaudet S, Schmidt MA, Jensen KF. 2004. A microfabricated device for subcellular organelle sorting. Anal Chem 76(19):5705-12.

Markx GH, Davey CL. 1999. The dielectric properties of biological cells at radiofrequencies: Applications in biotechnology. Enzyme and Microbial Technology 25(3-5):161-171.

Martin SJ, Reutelingsperger CPM, McGahon AJ, Rader JA, Vanschie R, Laface DM, Green DR. 1995. Early redistribution of plasma-membrane phosphatidylserine is a general feature of apoptosis regardless of the initiating stimulus- inhibition by overexpression of bcl-2 and abl. Journal of Experimental Medicine 182(5):1545-1556.

Park BY, Madou MJ. 2005. 3-D electrode designs for flow-through dielectrophoretic systems. Electrophoresis 26(19):3745-3757.

Pethig R, Kell DB. 1987. The passive electrical properties of biological systems: their significance in physiology, biophysics and biotechnology. Phys Med Biol 32(8):933-70.

Pethig R, Markx GH. 1997. Applications of dielectrophoresis in biotechnology. Trends in Biotechnology 15(10):426-432.

Pohl HA. 1951. The motion and precipitation of suspensoids in divergent electric fields. Journal of Applied Physics 22(7):869-871.

Preckel T, Kuschel M, Barthmaier P, Valer M, Buhlmann C. A new tool for routine testing of cell cultures- Integration of cell staining and anlalysis of cellular protein expression on a microfluidic chip-based system. Agilent Technologies Poster (www.agilent.com/chem/labonachip).

Qin JH, Ye NN, Liu X, Lin BC. 2005. Microfluidic devices for the analysis of apoptosis. Electrophoresis 26(19):3780-3788.

Quinti L, Weissleder R, Tung CH. 2006. A fluorescent nanosensor for apoptotic cells. Nano Letters 6(3):488-490.

Sanchez-Alcazar JA, Ault JG, Khodjakov A, Schneider E. 2000. Increased mitochondrial cytochrome c levels and mitochondrial hyperpolarization precede camptothecin-induced apoptosis in Jurkat cells. Cell Death and Differentiation 7(11):1090-1100.

Sane AT, Cantin AM, Paquette B, Wagner JR. 2004. Ascorbate modulation of H2O2 and camptothecin-induced cell death in Jurkat cells. Cancer Chemotherapy and Pharmacology 54(4):315-321.

Sohn LL, Saleh OA, Facer GR, Beavis AJ, Allan RS, Notterman DA. 2000. Capacitance cytometry: measuring biological cells one by one. Proc Natl Acad Sci U S A 97(20):10687-90.

Span LFR, Pennings AHM, Vierwinden G, Boezeman JBM, Raymakers RAP, de Witte T. 2002. The dynamic process of apoptosis analyzed by flow cytometry using Annexin-V/propidium iodide and a modified in situ end labeling technique. Cytometry 47(1):24-31.

Tabuchi M, Baba Y. 2004. Self-contained on-chip cell culture and pretreatment system. J Proteome Res 3(4):871-7.

Tamaki E, Sato K, Tokeshi M, Sato K, Aihara M, Kitamori T. 2002. Single-cell analysis by a scanning thermal lens microscope with a microchip: Direct monitoring of cytochrome c distribution during apoptosis process. Analytical Chemistry 74(7):1560-1564.

Tay FEH, Yu LM, Pang AJ, Iliescu C. 2007. Electrical and thermal characterization of a dielectrophoretic chip with 3D electrodes for cells manipulation. Electrochimica Acta 52(8):2862-2868.

Thirumala S, Forman JM, Monroe WT, Devireddy RV. 2007. Freezing and post-thaw apoptotic behaviour of cells in the presence of palmitoyl nanogold particles. Nanotechnology 18(19):-.

Valero A, Merino F, Wolbers F, Luttge R, Vermes I, Andersson H, van den Berg A. 2005. Apoptotic cell death dynamics of HL60 cells studied using a microfluidic cell trap device. Lab on a Chip 5(1):49-55.

van Engeland M, Nieland LJW, Ramaekers FCS, Schutte B, Reutelingsperger CPM. 1998. Annexin V-affinity assay: A review on an apoptosis detection system based on phosphatidylserine exposure. Cytometry 31(1):1-9.

van Tilborg GAF, Mulder WJM, Deckers N, Storm G, Reutelingsperger CPM, Strijkers GJ, Nicolay K. 2006. Annexin A5-functionalized bimodal lipid-based contrast agents for the detection of apoptosis. Bioconjugate Chemistry 17(3):741-749.

vanEngeland M, Ramaekers FCS, Schutte B, Reutelingsperger CPM. 1996. A novel assay to measure loss of plasma membrane asymmetry during apoptosis of adherent cells in culture. Cytometry 24(2):131-139.

Vaux DL, Strasser A. 1996. The molecular biology of apoptosis. Proceedings of the National Academy of Sciences of the United States of America 93(6):2239-2244.

Vermes I, Haanen C, Steffensnakken H, Reutelingsperger C. 1995. A Novel Assay for Apoptosis - Flow Cytometric Detection of Phosphatidylserine Expression on Early Apoptotic Cells Using Fluorescein-Labeled Annexin-V. Journal of Immunological Methods 184(1):39-51.

Wang LS, Flanagan L, Lee AP. 2007. Side-wall vertical electrodes for lateral field microfluidic applications. Journal of Microelectromechanical Systems 16(2):454-461.

Wang XJ, Becker FF, Gascoyne PRC. 2002. Membrane dielectric changes indicate induced apoptosis in HL-60 cells more sensitively than surface phosphatidylserine expression or DNA fragmentation. Biochimica Et Biophysica Acta-Biomembranes 1564(2):412-420.

Wei SY, Vaidya B, Patel AB, Soper SA, McCarley RL. 2005. Photochemically patterned poly(methyl methacrylate) surfaces used in the fabrication of microanalytical devices. Journal of Physical Chemistry B 109(35):16988-16996.

Wheeler AR, Throndset WR, Whelan RJ, Leach AM, Zare RN, Liao YH, Farrell K, Manger ID, Daridon A. 2003. Microfluidic device for single-cell analysis. Analytical Chemistry 75(14):3581-3586.

Willingham MC. 1999. Cytochemical methods for the detection of apoptosis. Journal of Histochemistry & Cytochemistry 47(9):1101-1109.

Wolbers F, Haanen C, Andersson H, Van den Berg A, Vermes I. 2005. Chapter 8, Analysis of Apoptosis on Chip: Why the move to chip technology? In: Berg HAaAvd, editor. Lab-on-Chips for Cellomics Micro and Nanotechnologies for Life Science. Netherlands: Kluwer Academic Publishers. p 197-224.

Yang MS, Li CW, Yang J. 2002. Cell docking and on-chip monitoring of cellular reactions with a controlled concentration gradient on a microfluidic device. Analytical Chemistry 74(16):3991-4001.

Yi CQ, Li CW, Ji SL, Yang MS. 2006a. Microfluidics technology for manipulation and analysis of biological cells. Analytica Chimica Acta 560(1-2):1-23.

Yi CQ, Zhang Q, Li CW, Yang J, Zhao JL, Yang MS. 2006b. Optical and electrochemical detection techniques for cell-based microfluidic systems. Analytical and Bioanalytical Chemistry 384(6):1259-1268.

CHAPTER 2. FLOW-BASED METHOD FOR QUANTIFYING CELL VIABILITY OF CELLS EXPOSED TO PALYMITOYL GOLD NANOPARTICLES AS CRYOPRESERVATIVE[1]

2.1 Introduction to Cryotherapeutic Procedures and Cell Studies

The aim of this study was to evaluate the freezing response of HeLa and Jurkat cells in the presence of commercially available nanoparticles, NPs (Palmitoyl Nanogold®, Nanoprobes). The cells were incubated with NPs for either 5 min or 3 h, and a calorimeter technique was then used to generate the volumetric shrinkage response during freezing at 20 °C min^{-1}. Concomitantly, we also examined the effect of a commonly used cryoprotectant, dimethylsulfoxide, DMSO (10% v/v ratio) on the freezing response of HeLa and Jurkat cells. By fitting a model of water transport to the experimentally determined volumetric shrinkage data, the reference hydraulic conductivity, L_{pg}, (μm/min-atm) and activation energy, E_{Lp}, (kcal mol^{-1}) were obtained. For HeLa cells, the values of L_{pg} ranged from 0.08 to 0.23 μm/min-atm, while E_{Lp} ranged from 10.9 to 37.4 kcal mol^{-1}. For Jurkat cells these parameter values ranged from 0.05 to 0.16 μm/min-atm and 9.5 to 35.9 kcal mol^{-1}. A generic optimal cooling rate equation was then used to predict the optimal rates of freezing HeLa and Jurkat cells in the presence and absence of DMSO and NPs. The post-thaw viability and apoptotic response of HeLa and Jurkat cells was further investigated by cooling cells at three rates in the presence and absence of DMSO and NPs using a commercially available controlled rate freezer. Jurkat cells treated in this manner demonstrated an increase in their adhesive properties after 18 h incubation and adhered strongly to the bottom of the culture plate. This observation prevented further analysis of Jurkat apoptotic and necrotic post-thaw responses. There was no significant effect of NPs or DMSO alone on

---

[1] Reprinted with permission from IOP Publishing. Thirumala, S., Forman, J.M., Monroe, W.T., Devireddy, R.V. (2007). "Freezing and post-thaw apoptotic behaviour of cells in the presence palmitoyl nanogold particles." Nanotechnology 18(195104).(www.iop.org/journals/nano)

HeLa cell viability prior to freezing. The post-thaw results from HeLa cells show that the NPs increased the measured post-freeze apoptotic response when cooled at 1 °C min^{-1}, suggesting a possible therapeutic use of NPs in cryodestructive procedures (http://iopscience.iop.org/0957-4484/18/19/195104/?ejredirect=.iopscience).

Successful cryotherapeutic procedures for biological cells and tissues will impact a wide range of human endeavors, including assisted reproductive techniques, cancer recovery and re-habilitation procedures, organ storage and transplantation processes and conservation of endangered species. In general, freezing storage requires the addition of a class of chemicals denoted as cryoprotective agents (CPAs). Their extensive use is based on the serendipitous observation by Polge and co-workers (Polge et al. 1949) that sperm cells were able to survive freezing in the presence of a chemical (glycerol) and did not survive the freezing process in its absence. There is considerable divergence across the classes of organic molecules that possess some CPA activity, ranging from low molecular weight solutes like dimethylsulfoxide (DMSO), glycerol and sucrose (Lovelock 1954) to high molecular weight polymers like polyvinylepyrrolidone (PVP) and hydroxyl ethyl starch (Ashwoods et al. 1972). Several hypotheses have attempted to explain the protective action of CPAs, but none of them are widely accepted or well established (Ashwoods et al. 1972; Karow 1991; Lovelock 1954; Meryman 1974; Pegg 2002; Yancey 2005). On the other hand, a significant amount of evidence suggests that the benefits of chemicals should be weighed against their potential to produce direct cryoinjury (Baust et al. 2000; Fahy 1986; Fowler and Toner 2005; Fuller 2004; Rall 1987).

Studies related to cryoprotectant action dates back to the 1950s, when Lovelock (Lovelock 1954) demonstrated that the hemolysis of red blood cells depends on the permeability of the neutral solutes. Mazur (Mazur 1960) proposed that polymeric CPAs avoid denaturing of

the membranes by strong salt solutions at low temperatures either by preventing seeding of the supercooled water inside the cells or by coating the sensitive plasma membranes. Nash (Nash 1966) made a more detailed attempt to explain the cryoprotectant action on a combination of parameters based on the property of forming strong and numerous hydrogen bonds, interaction with water molecules, and the volume occupied by a molecule of solute. Farrant (Farrant 1969) advocated that a polymer such as PVP may exhibit enhanced colligative properties at higher concentrations and may protect cells by lowering the external salt concentrations in a manner similar to low molecular cryoprotectants. Anchordoguy *et al (Anchordoguy et al. 1987)* suggested additional modes of action of CPAs such as electrostatic interaction of CPAs (such as glycerol, trehalose and sucrose) with polar head groups of phospholipids, and the efficacy of CPAs depends on the strength of these interactions. Arakawa, Timasheff and colleagues have shown that the effect of solute on the stability of proteins derives from the balance between stabilizing and destabilizing effects of solute either by preferential binding or preferential exclusion from the protein surface (Arakawa and Timasheff 1985; Crowe et al. 1990). The disaccharide sugars, such as trehalose, have also been shown to preserve membrane structure and function by interacting with polar head groups of phospholipids at hypertonic exposures during freezing (Rudolph and Crowe 1985). However, Ashwood-Smith *et al* (Ashwoods.Mj et al. 1972), Williams and Harris (Williams and Harris 1977) and Williams (Williams 1983) have suggested that the cryoprotective efficiency of polymers resides in their ability to alter the physical properties of solutions during freezing rather than indirect effects on cell membranes (Takahashi et al. 1988).

The aim of the present study is to examine the potential cryobiological applications of commercially available nanoparticles, NPs (Palmitoyl Nanogold®, Nanoprobes, Yaphank, NY).

Gold NPs have been widely used for analytical and biomedical applications for many years. For an excellent review of gold nanoparticles and their applications, the interested reader is referred to Daniel and Astruc (Daniel and Astruc 2004). Palmitoyl gold nanoparticles have been used to label and visualize lipid vesicles and cell membranes (Brewer et al. 2004) yet their direct effect on membrane permeability and thus cryostability remains unknown. The palmitate functionality on these nanoparticles may serve as an anchor to membranes similar to the fatty acylated domains of amphitrophic proteins that regulate membrane function (Resh 1999). In addition to specific chemistries, the heat conducting aspects of metallic nanoparticles have been shown to influence targeted freezing in cryosurgical procedures (Yu et al. 2005). Because the modes of cryoprotectant action can vary from alteration of physical properties of the freezing media to the direct changes in the cell membrane properties, we presumed that NPs could act as benign replacement for chemically active CPAs.

During freezing of cells in suspensions, ice forms initially in the extracellular space. Depending on the imposed cooling rate, the two main biophysical processes during freezing will then occur: (i) cellular dehydration associated with the loss of intracellular water, or (ii) intracellular ice formation (IIF) associated with the nucleation of ice crystals within the intracellular space. Water transport has been extensively investigated in single cells using standard cellular microscopy (Diller 2005) and, more recently, a differential scanning calorimetric (DSC) technique (Devireddy et al. 1998; Thirumala et al. 2005a; Thirumala et al. 2005b). In the present study, we utilized the DSC technique to assess the water transport response during freezing of HeLa and Jurkat cells with and without NPs. These two cell lines were chosen as examples of an adherent (HeLa) and a suspension (Jurkat) cell, each of which is well characterized, widely used and commonly frozen in various laboratories. In the interest of

completeness, we also present water transport responses during freezing of these cells in the presence of DMSO, a commonly used CPA. By fitting a well established model of water transport to the measured water transport response we determined the membrane permeability (water transport) parameters during freezing of HeLa and Jurkat cells in the absence of CPAs, in the presence of DMSO and in the presence of NPs. The experimentally determined membrane permeability parameters were incorporated into a recently developed generic optimal cooling rate equation (Thirumala and Devireddy 2005) and used to predict the optimal cooling rates for cryopreservation of the two cell types studied. Based on the predicted optimal cooling rates, three cooling rates were chosen to investigate the post-thaw behaviour of HeLa and Jurkat cells frozen and thawed in the presence and absence of DMSO and NPs.

There exists substantial evidence in the literature that apoptosis could be a possible contributing factor in cryopreservation failure. For example, it has been reported that apoptotic cell death occurs in cells exposed to subfreezing temperatures (Hollister 1998; Mathew et al. 1997). Therefore, in addition to analysing the immediate post-thaw survival, we have also analysed the post-freeze apoptotic response of the HeLa cells (for reasons, described later, Jurkat cells were not used in these apoptotic studies). Post-thaw experiments were based on propidium iodide (PI) uptake and the detection of the early apoptosis event, phosphatidylserine (PS) translocation (Koopman et al. 1994) using a flow cytometric annexin V apoptosis assay (Pena et al. 2003).

2.2 Theoretical Background

A model for water and solute transport in response to chemical potential gradients based on irreversible thermodynamics has been proposed by Kedem and Katchalsky that consists of two differential equations which describe the water and CPA flux across the membrane (Kedem and

Katchalsky 1958). If the flux of CPA is negligible in comparison to the flux of water, and assuming that water is essentially the only species transported at subzero temperatures, the Kedem–Katachalsky model reduces to a water transport model, as proposed by Mazur (Mazur 1963) and later modified by Levin *et al* (Levin et al. 1976). The water transport model of Mazur can be further modified to incorporate the presence of CPAs as:

$$\frac{dV_w}{dT} = -\frac{L_pART}{Bv_w}\left[\ln\left(\frac{(V_{cell}-V_b)-(n_sv_s+n_{cpa}v_{cpa})}{(V_{cell}-V_b)-(n_sv_s+n_{cpa}v_{cpa})+v_w(\psi_sn_s+n_{cpa})}\right)-\frac{\Delta H_f}{R}\left(\frac{1}{T_R}-\frac{1}{T}\right)\right] \quad (2.1)$$

where R is the universal gas constant; V_{cell} is the cell volume; V_b is the osmotically inactive cell volume; A is the constant cell surface area; T is the absolute temperature; T_R is the reference temperature (273.15K); B is the cooling rate (°Cmin^{-1}); v_w is the molar specific volume of water; v_{cpa} is the specific molar volume of CPA; n_{cpa} is the number of moles of CPA; ψ_s is the dissociation constant for salt in water (=2); n_s is the number of moles of salt initially inside the cell; H_f is the latent heat of fusion of water; L_p is the permeability of the plasma membrane to water. The permeability of the plasma membrane to water, L_p, is assumed to be a function of temperature and concentration of solute, CPA and water, and is given as (Levin et al. 1976):

$$L_p = L_{pg}(cpa)\exp\left(-\frac{E_{Lp}(cpa)}{R}\left(\frac{1}{T}-\frac{1}{T_R}\right)\right) \quad (2.2)$$

where L_{pg}(cpa) is thepermeability of the cell membrane to water at T_R = 273.15 K; and E_{Lp}(cpa) is the apparent activation energy for the process. Model assumptions include membrane-limited transport, with negligible temperature and pressure differentials across the plasma membrane, the external solution in equilibrium with extracellular ice, and an approximately ideal internal solution (Devireddy et al. 1998; McGrath et al. 1975; Smith et al. 1998; Toner 1993).

2.3 Materials and Methods

2.3.1 Culture and Isolation of HeLa and Jurkat Cells

HeLa cells (human epithelial carcinoma cells, American Type Culture Collection) were maintained in 25 cm^2 flasks (BD Falcon, Franklin Lakes, NJ) with 5 ml of Dulbecco's Modified Eagle's medium-reduced serum (DMEM-RS) supplemented with 3% foetal bovine serum (FBS) and incubated at 37 °C in a humidified atmosphere containing 5% CO_2. Jurkat T lymphocyte cells (E6.1, ATCC) were maintained in 25 cm^2 flasks (BD Falcon, Franklin Lakes, NJ) with 5 ml of HyQ® RPMI-1640-reduced serum medium (RPMI- RS) supplemented with 3% foetal bovine serum (FBS) and also incubated at 37°C in a humidified atmosphere containing 5% CO_2. HeLa cells were plated at a density of 80 000 cells cm^{-2} in 12-well culture plates (BD Falcon, Franklin Lakes, NJ) and were allowed to adhere and grow for 24 h prior to trypsinization (0.25% trypsin) and resuspension in Opti-MEM® serum-free medium for differential scanning calorimeter (DSC) and controlled rate freezer (CRF) experiments. Opti-MEM was chosen as a reduced protein medium for cell treatments to minimize potential for NP-serum protein interactions that could block potential cryobiological effects. Jurkat cells were resuspended in Opti-MEM to a density of $\sim 1 \times 10^6$ cells ml^{-1} in 12-well culture plates (BD Falcon, Franklin Lakes, NJ) for treatment prior to being transferred to sterile eppendorf tubes for the DSC and CRF experiments.

Six separate DSC water transport experiments were conducted for HeLa and Jurkat cells in the absence of any CPAs, in the presence of a permeating CPA, dimethylsulfoxide (DMSO; 10%, v/v) and in the presence of NPs (Palmitoyl Nanogold) for incubation times of either 5 or 180 min. While 180 min is longer than a typical CPA pre-freeze treatment, this extended incubation of nanoparticles and cells was chosen to ensure their complete association, based on

typical durations for nanogold labelling procedures (Hainfeld and Powell 2000). All samples used in the experiments had concentration of cells ranging from 0.5 to 1×10^6 cells ml^{-1}.

For DSC experiments in the absence of CPAs, HeLa cells were washed, harvested by trypsinization, concentrated by centrifugation at 400 × *g* for 5 min, resuspended to ~20 μl in Opti-MEM and placed on ice. For DSC experiments in the presence of CPA, cells were treated in an identical manner as above except that the cell pellet was resuspended in stock CPA solution (10% v/v DMSO; Irvine Scientific) and equilibrated for 10 min. Osmolarity of the CPA media was measured to be 1685 mOsm which includes ~1400 mOsm of DMSO (Vapro® Vapour Pressure Osmometer, Wescor Inc). And finally, for DSC experiments in the presence of NPs, 300 nanomoles of nanogold particles (Palmitoyl Nanogold®, Nanoprobes, Yaphank, NY) were first dissolved in 50 μl of DMSO as DMSO is a commonly used organic solvent to enhance the solubility of hydrophobic nanoparticles in aqueous solutions (Balakin et al. 2006). The DMSO+NP mixture was then added to 50 ml of Opti–MEM to create a uniform stock solution containing 3.6×10^{15} nanoparticles ml^{-1} of Opti-MEM. The addition of DMSO to the Nanogold resulted in ~0.001% DMSO concentration in the final Opti-MEM + NPs solution and was presumed to have a negligible effect. For 3 h NPs treatment, concentrated HeLa cells were resuspended in the NPs solution and then plated in a 12-well for 3 h in the incubator before harvesting for the DSC experiments. For the 5 min NPs treatment the concentrated cell pellet was resuspended in NPs solution for 5 min before being used in the DSC experiments. The osmolarity measurements of the NPs solution ranged from 285 to 290 mOsm (Vapro Vapour Pressure Osmometer) and were essentially similar to the osmolarity measurements of Opti-MEM solution. This suggests that the presence of NPs did not change the osmolarity of the NPs freezing medium.

2.3.2 DSC Experiments

The DSC experiments to measure the water transport in HeLa and Jurkat cells were performed as reported in earlier studies on other cell systems (Devireddy et al. 2004; Devireddy et al. 1998; Diller 2005; Thirumala et al. 2006; Thirumala et al. 2005a; Thirumala et al. 2005b; Yuan and KR 2001). Briefly, the heat release measurements of interest are Δq_{dsc} and $\Delta q(T)_{dsc}$, which are the total and fractional differences between the heat releases measured by integration of the heat flows during freezing of osmotically active (live) cells in media, $q_{initial}$, and during freezing of osmotically inactive (dead) cells in media, q_{final} (i.e. $\Delta q_{dsc} = q_{initial} - q_{final}$; $\Delta q(T)_{dsc} = q(T)_{initial} - q(T)_{final}$). This difference in heat release has been shown to be related to cell volume changes in several biological systems as:

$$V(T) = V_i - \frac{\Delta q(T)_{dsc}}{\Delta q_{dsc}} \cdot (V_i - V_e) \tag{2.3}$$

The unknowns needed in equation (2.3) apart from the DSC heat release readings are V_i (the initial cell volume) and V_e (the end or the final cell volume). The cell geometry and the inactive cell volume (V_b) of HeLa and Jurkat cells were determined at constant room temperature by using a light microscope (Nikon Eclipse TS100) equipped with METAVIEW software (see section 2.4 and Figure 2.1).

2.3.3 Biophysical Parameter Estimation

The biophysical parameters for water transport were then estimated using a non-linear regression algorithm as previously reported (Thirumala et al. 2006; Thirumala et al. 2003; Thirumala et al. 2005a). The experimentally measured water transport data at 20 ºC min^{-1} for both cell types were compared to theoretically predicted curves (Eqns. 2.1 and 2.2), and the biophysical parameters of water transport, L_{pg} and E_{Lp} (or $L_{pg}[cpa]$ and $E_{Lp}[cpa]$), were

iteratively adjusted until the chi-squared variance, χ^2, was minimized (or a goodness of fit parameter R^2 was maximized: a value of 1 representing a perfect fit while a value of 0 represents a flawed fit) using a gradient search method as described in Bevington and Robinson (Bevington and Robinson 1992). All reported parameters were obtained for curve fits with a variance $\chi^2 < 10^{-3}$ or an $R^2 > 0.99$.

Table 2.1 Predicted subzero membrane permeability parameters (the reference membrane permeability in the absence and presence of CPAs, L_{pg} or $L_{pg}[cpa]$, and activation energy in the absence and presence of CPAs, E_{Lp} or $E_{Lp}[cpa]$) and optimal rates of freezing for HeLa and Jurkat cells. Note that the goodness-of-fit, R^2 value was always greater than 0.99.

Cell type (V_b)	Freezing media	L_{pg} or L_{pg}[cpa] (μm/min-atm)	E_{Lp} or E_{Lp}[cpa] (kcal mol^{-1})	B_{opt} (°C min^{-1})
HeLa cells ($0.45V_o$)	No CPA	0.08	10.9	30.6
	10% DMSO	0.08	16.7	22.4
	Nanoparticles (5 min incubation)	0.23	37.4	21.0
	Nanoparticles (3 h incubation)	0.19	33.8	21.1
Jurkat cells ($0.52V_o$)	No CPA	0.05	9.5	33.7
	10% DMSO	0.06	17.4	24.0
	Nanoparticles (5 min incubation)	0.16	35.9	22.3
	Nanoparticles (3 h incubation)	0.13	33.3	20.8

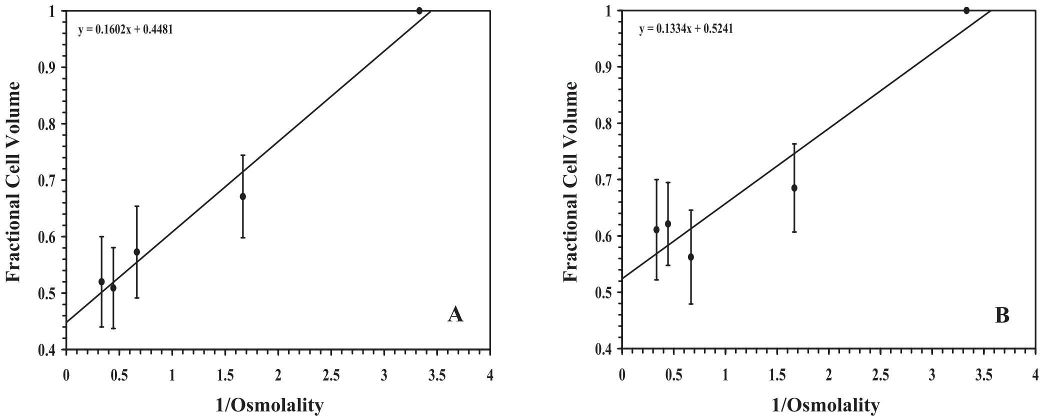

Figure 2.1 The Boyle-van't plot showing the resulting volume changes of the HeLa (A) and Jurkat cells (B) when cells were exposed to several external osmolalities (0.3, 0.6, 1.5, 2.25 and 3.00 Osm/kg) at constant temperature (~27 ºC). The required osmolalities were achieved by diluting 10x D-PBS (3.00 Osm/kg) with distilled water (~0.0 Osm/kg). The filled circles represent average volumetric data. The dark line is a linear curve (assumes cells behave as ideal osmometers) when extrapolated to infinite osmolality, results in an osmotically inactive cell volume, V_b, of $0.45V_o$ for HeLa cells and $0.52V_o$ for Jurkat cells. The inverse of osmolality is plotted along x-axis and normalized volume is plotted along y-axis. Error bars represent standard deviation in the data (for each point n = 60 - 75 cells).

2.3.4 Theoretical Prediction of Optimal Cooling Rates

Thirumala and Devireddy (Thirumala and Devireddy 2005) reported that, for a variety of biological systems, a comparison of the published experimentally determined values of B_{opt} (in°C min^{-1}) agreed quite closely with the value obtained using a generic optimal cooling rate equation that defines:

$$B_{opt} = 1009.5 \bullet e^{(-0.0546 \bullet E_{Lp})} \bullet (L_{pg}) \bullet \left(\frac{A_c}{V_o - V_b} \right) \tag{2.4}$$

In this equation, L_{pg} and E_{Lp} (or $L_{pg}[cpa]$ and $E_{Lp}[cpa]$) represent the membrane permeability parameters (in µm/min-atm and Kcal/mole, respectively), while the last term $\left(\frac{A_c}{V_o - V_b} \right)$ (in µm^{-1}) represents the ratio of the available surface area for water transport (A_c) to the initial volume of intracellular water ($V_o - V_b$). Once the cell level parameters L_{pg} and E_{Lp} (or $L_{pg}[cpa]$ and $E_{Lp}[cpa]$) are determined using the curve-fitting procedure described above, we utilized Eqn. (2.4) to predict the optimal rates of freezing HeLa cells.

2.3.5 Freeze/Thaw Experiments

All reagents for cell culture were purchased from HyClone Laboratories, Inc. (Logan, UT), unless otherwise stated. Annexin V-FITC/PI kit was purchased from Molecular Probes (Eugene, Oregon). Staurosporine was purchased from CalBiochem (EMD BioSciences, Darmstadt, Germany). HeLa and Jurkat cell culture and treatments for freeze/thaw experiments were the same as mentioned previously for DSC experiments except that, after centrifugation, the cell pellet was resuspended in 0.5 ml of the appropriate cryopreservation or nanoparticle solutions in a 1.5 ml sterile eppendorf tube (USA Scientific, Ocala, FL) and were arranged onto a 1.5 ml tube rack (Stackarack for 1.5 ml tube, USA Scientific). All freezing experiments were

carried out using a programmable controlled-rate freezing (CRF) machine (Planer Series Kryo 560-16, TS Scientific, Perkasie, PA). The tube cluster was loaded into the cryomachine (which was precooled to 4 °C) and kept for 1 min for equilibration. The samples were then cooled to an end temperature of −80 °C at three freezing rates: 1, 22 and 34 ºC min^{-1} (these cooling rates were chosen based on the predicted optimal rates of cooling; see table 2.1). Using the procedures described earlier by Thirumala *et al* (Thirumala et al. 2005b), the actual cooling rate imposed by the CRF on the sample was within 5% of 1 ºC min^{-1} and within 10% of 22 ºC min^{-1} and 34 ºC min^{-1}. Because the CRF machine used in this study was limited to a controlled thawing/warming rate of 40 ºC min^{-1}, the thawing rate 200 ºC min^{-1} was obtained by removing the tube rack from the CRF machine and quickly bringing the tubes into contact with a warm water bath maintained at 37 ºC (Thirumala et al. 2005b).

The thawed samples were then centrifuged, resuspended in appropriate culture media, and seeded in separate wells of a 12-well plate for an 18 h incubation period at 37 ºC. Non-frozen cell controls of HeLa and Jurkat cells were also carried out for each experimental condition to determine if there were any cellular effects due to the 10% DMSO (10 min), 5 min NP, and 3 h NP treatments alone. Following the treatment, the cells were resuspended in fresh medium and plated in a 12-well plate. After 18 h, the non-frozen cell controls and the thawed samples were analyzed by brightfield mircroscopy and flow cytometry.

2.3.6 Brightfield Phase-contrast Microscopy

Following the 18 h recovery period, HeLa and Jurkat cells were imaged by brightfield phase-contrast microscopy at 20× magnification. Images were acquired with an inverted Eclipse TS100 Nikon fluorescence microscope and a CoolSnapFX camera (Photometrics,

Tucson, AZ). Image processing was performed using MetaVue software (Universal Imaging Corporation, West Chester, PA).

2.3.7 Cell Viability and Apoptosis/Necrosis Assessment

A well-established annexin V apoptosis assay was analysed by quantitative flow cytometry (Pena et al. 2003). This assessment was carried out only for HeLa cells, as the Jurkat cells treated in similar fashion to the HeLa cells exhibited adhesion to the cell culture plate (see section 4). As a chemically induced apoptotic control, HeLa cells were incubated in fresh medium enriched with 0.25 μM staurosporine. For a necrotic control, HeLa cells were incubated for 18 h in fresh medium with 2mM hydrogen peroxide ($H_2 O_2$). The no-treatment control consisted of HeLa cells treated in fresh medium, free from inducing agents. For each treatment, detached and attached cells were pooled, harvested by trypsinization (0.25% trypsin), washed with 200 μl of culture medium and resuspended in 100 μl of 1X annexin-binding buffer (included in annexin V- FITC/PI kit). 100 μl of HeLa cell suspension was mixed with 5 μl of annexin-V-FITC and 1 μl of 100 μg ml^{-1} propidium iodide (PI) and incubated in the dark at room temperature for 15 min. Liquid volume was removed by centrifugation and aspiration, and the cells were resuspended by gentle vortexing in 300 μl of 1X annexin-binding buffer to be analysed on the flow cytometer. Apoptosis analyses for HeLa cells were performed on a FACS Caliber flow cytometer (BD Biosciences, San Jose, CA) utilizing 488 nm laser excitation and fluorescence emission at 530 nm (FL1) and >575 nm (FL3). Forward and side scatter measurements were made using linear amplification, and all fluorescence measurements were made with logarithmic amplification. A total of 1100–20000 cells per sample were acquired using Cell Quest software (BD Biosciences, San Jose, CA), and data samples were analysed using WinMDI 2.8 software (by Dr J Trotter, Scripps Institute, La Jolla, CA).

Apoptosis is characterized by phosphatidylserine (PS) translocation from the inner leaflet to the outer leaflet of the lipid bilayer, while the cell membrane remains intact. Annexin V-positive cells correspond to cells that have experienced PS translocation. PI staining of the cells indicates that the integrity of the cell membrane has been compromised and is used to distinguish living and early apoptotic cells from necrotic cells. The fluorescent dotplots show three cell populations: live (annexin V-FITC-negative/PI-negative), necrotic (annexin V-FITC-positive/PI-positive), and apoptotic (annexin V-FITC- positive/PI-negative). Quadrant analysis was performed on the gated fluorescence dotplot to quantify the percentage of live, necrotic and apoptotic cell populations. The quadrant was placed according to the no-treatment control and 2 mM H_2O_2 necrotic control (the representative reference dotplots with quadrants are shown in the supplementary data (available at stacks.iop.org/Nano/18/195104)).

2.3.8 Statistical Analysis

All values are indicated as mean ± SEM. Student's *t*-test was employed, with $p < 0.05$ considered to be significant. Each '*n*' replicate was composed of a single well and treatment in which 1100–20000 cell events were analysed and each experiment was conducted in triplicate.

2.4 Results

2.4.1 Cell Geometry and Osmotically Inactive Cell Volume

The trypsinized HeLa cells were found to have an initial diameter of 15 ± 1.5 μm (n = 15), and the Jurkat cell diameter was measured to be 12 ± 1.1μm (n = 15). The corresponding initial isotonic volume, $V_{o,}$ is ~1767 μm^3 for HeLa cells and 905 μm^3 for Jurkat cells. Osmotically inactive cell volume of HeLa and Jurkat cells was determined by the use of Boyle-van't plot which plots equilibrium cell volume as the dependent variable and the inverse of the external osmolality as the independent variable, see figure 2.1. A critical assumption in Boyle

van't Hoff analysis is the inhibition or suppression of active compensatory processes by which cells readjust their volume during their passive osmotic water transport (Lucke and McCutcheon 1932; Wehner et al. 2004). In figure 2.1, the filled circles represent the average cell volume data from the bright field image analysis**,** and the error bars represent the standard deviations in the measurements. A linear curve was fit to the measured cell volume at various external osmolalities. Extrapolating the linear fit to the vertical axis, corresponding to an infinite external osmolality, resulted in an osmotically inactive cell volume of $0.45V_o$ for HeLa cells and $0.52V_o$ for Jurkat cells. Note that the presence of DMSO in the intracellular compartment increases the osomotically inactive cell volume of HeLa cells to $\sim 0.53V_i$ and Jurkat cells to $\sim 0.59V_i$. Based on the HeLa and Jurkat cell dimensions measured, the ratio of $\left(\frac{A_c}{V_o - V_b}\right)$ is 0.727 μm^{-1} for HeLa cells (using $V_b = 0.45V_o$) and 1.04 μm^{-1} for Jurkat cells (using $V_b = 0.52V_o$).

2.4.2 Freezing Response of HeLa Cells

Figure 2.2 shows the water transport data and simulation for HeLa cells using the best-fit parameters in equation (2.1) at a cooling rate of 20 °C min^{-1} in a medium containing no CPAs (figure 2.2(A)), DMSO as CPA (figure 2.2(B)) and incubated with NPs for 5 min (figure 2.2(C)) and 3 h (figure 2.2(D)). The dynamic portion of the cooling curve (region where the initial and final heat release thermograms are distinct and separate) was found to be between −0.6 and −12 °C with no CPAs or with NPs[2], while it was between −3.1 and −21 °C with DMSO. The model simulated equilibrium cooling response (equilibrium is achieved at each temperature when the internal and external osmotic pressures are equal) is also shown for reference as a dotted line (· ·

---

[2] As stated earlier we have experimentally verified, using a vapor pressure osmometer, that the presence of NPs does not significantly impact the osmolality of the freezing media (and hence the phase change temperature in the presence of NPs is assumed to be –0.6 ºC).

· · · ·). The HeLa cell membrane permeability values that best fit the water transport data in the absence and presence of DMSO and NPs are shown in table 2.1. The theoretically predicted optimal cooling rate values obtained using equation (2.4) for freezing HeLa cells are also given in table 2.1; the optimal cooling rate for HeLa cells in the absence of CPAs is ~31 °C min^{-1}, in the media containing 10% DMSO is ~22 °C min^{-1} and in the media containing NPs is ~21°C min^{-1} (for both 5 min and 3 h incubation times).

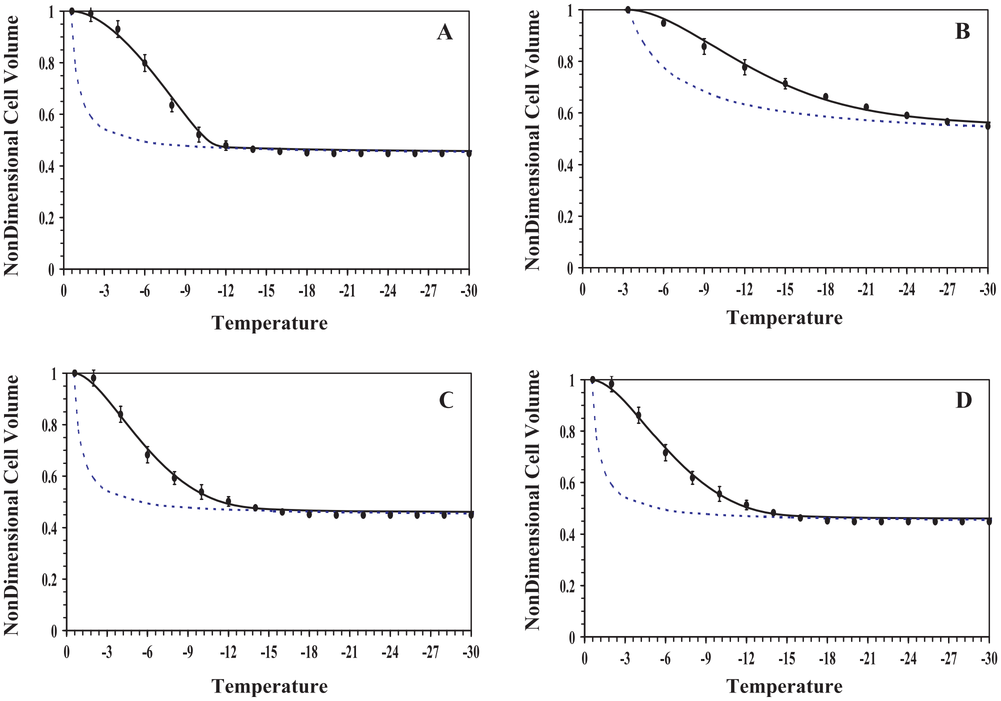

Figure 2.2 Volumetric response of HeLa cells as a function of subzero temperatures obtained using the DSC technique at 20 ºC/min in the absence of CPAs (A), in the presence of DMSO (B), in the presence of NPs with 5 min incubation (C) and in the presence of NPs with 180 min incubation (D). The measured volumetric response is shown as filled circles where as the model-simulated dynamic cooling response at 20 ºC min^{-1} is shown as a solid line and was obtained by using the best-fit membrane permeability parameters (*L_{pg} and E_{Lp} or L_{pg}[cpa] and E_{Lp}[cpa]*) (table 1) in the water transport equation (Eqns. 1 and 2). The simulated equilibrium cooling response is also shown, for reference, as a dotted line (· · · · · ·). The nondimensional volume is plotted along the y axis while the subzero temperatures are shown along the x axis. The error bars represent the standard deviation for the mean values of six separate DSC experiments (n = 6).

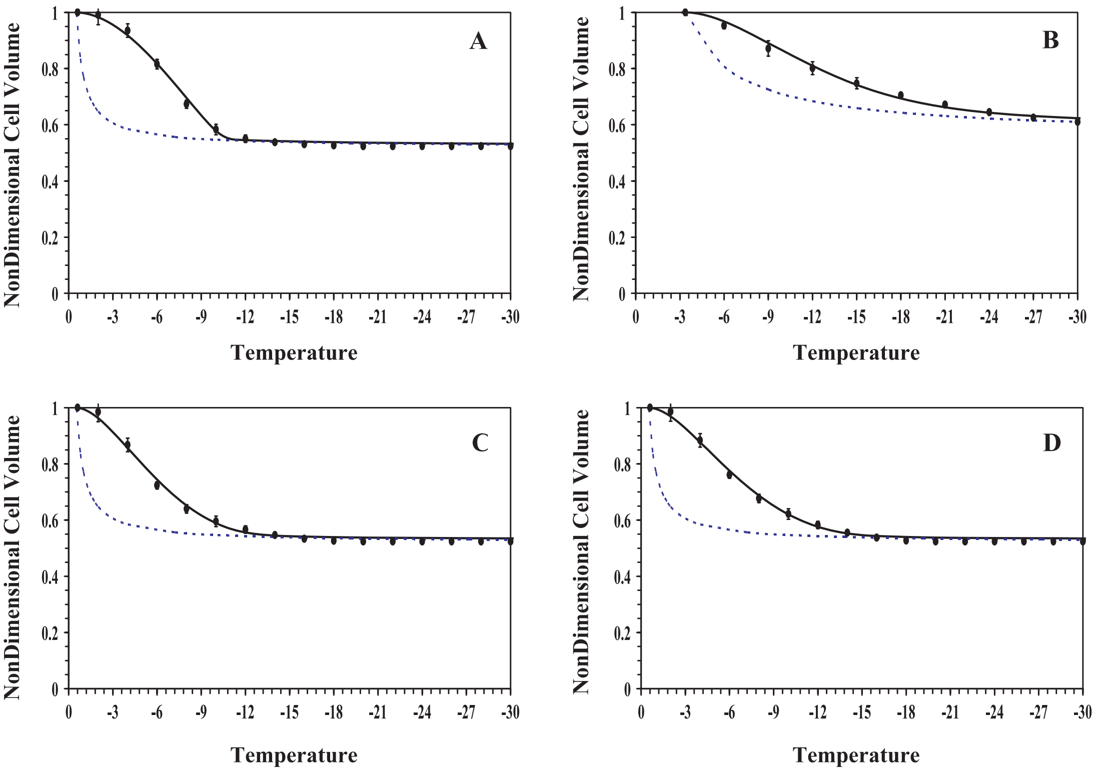

Figure 2.3 Volumetric response of Jurkat cells as a function of subzero temperatures obtained using the DSC technique at 20 ºC min^{-1} in the absence of CPAs (A), in the presence of DMSO (B), in the presence of NPs with 5 min incubation (C) and in the presence of NPs with 180 min incubation (D). The measured volumetric response is shown as filled circles where as the model-simulated dynamic cooling response at 20 ºC min^{-1} is shown as a solid line and was obtained by using the best-fit membrane permeability parameters (L_{pg} *and* E_{Lp} *or* $L_{pg}[cpa]$ *and* $E_{Lp}[cpa]$) (table 1) in the water transport equation (Eqns. 1 and 2). The nondimensional volume is plotted along the y-axis while the subzero temperatures are shown along the x-axis. The error bars represent the standard deviation for the mean values of six separate DSC experiments (n = 6).

The water transport data (see figure 2.2) obtained in the presence of NPs is significantly different (>99% confidence level using Student's *t*-test) from the water transport response of HeLa cells in the presence of DMSO. Additionally, the water transport response of HeLa cells obtained in the presence of DMSO is also significantly different than the response obtained in the absence of DMSO, albeit at a lower confidence level of 95%. There is no significant

difference between water transport behaviour of HeLa cells incubated with NPs for either 5 min or 3 h.

2.4.3 Freezing Response of Jurkat Cells

Figure 2.3 shows the water transport data and simulation for Jurkat cells using the best-fit parameters in equation (2.1) at a cooling rate of 20 °C min^{-1} in a medium containing no CPAs (figure 2.3(A)), DMSO as CPA (figure 2.3(B)) and incubated with NPs for 5 min (figure 2.3(C)) and 3 h (figure 2.3(D)). The dynamic portion of the cooling curve was found to be between −0.6 and −10 °C with no CPAs, −0.6 to −12°C with NPs, and it was between −3.1 and −21 °C in the presence of DMSO. The simulated equilibrium cooling response is shown as a dotted line (· · · · · ·). The Jurkat cell membrane permeability values that best fit the water transport data in the absence and presence of DMSO and NPs are shown in table 2.1. The theoretically predicted optimal cooling rate values obtained using equation (2.4) for freezing Jurkat cells are given in table 2.1; the optimal cooling rate for Jurkat cells in the absence of CPAs is ~34 °C min^{-1}, in the media containing 10% DMSO is ~24 °C min^{-1} and in the media containing NPs is ~22 °C min^{-1} (for both 5 min and 3 h incubation times).

Similar to the measured water transport response of HeLa cells, the water transport data obtained for Jurkat cells in the presence of NPs was significantly different (>99% confidence level using the Student's t-test) from the water transport response in the presence of DMSO. Also, the water transport response of Jurkat cells in the presence of DMSO was significantly different than the response obtained in the absence of DMSO, albeit at a lower confidence level of 95%. No significant difference in water transport response was observed when Jurkat cells were incubated either 5 min or 3 h, a behavior similar to that observed with HeLa cells. And finally, the equilibrium cooling response or the volumetric shrinkage response of HeLa and

Jurkat cells cooled infinitely slowly, was significantly different (>99% confidence level using the Student's t-test) from the dynamic water transport data obtained at 20 ºC min^{-1} for both cell types (shown in figures 2.2 and 2.3).

Figure 2.4 shows the contour plots of the goodness-of-fit parameter ($R^2 = 0.96$) in the L_{pg} and E_{Lp} (or $L_{pg}[cpa]$ and $E_{Lp}[cpa]$) space that 'fit' the measured water transport data for HeLa and Jurkat cells in the four media investigated. Any combination of L_{pg} and E_{Lp} (or $L_{pg}[cpa]$ and $E_{Lp}[cpa]$) shown to be within the contour will 'fit' the water transport data in the specified freezing media with an R^2 value > 0.96. Note that for both the HeLa and Jurkat cells the best fit parametric space obtained in the absence of DMSO or NPs is almost completely enclosed by that obtained in the presence of NPs. This suggests that the water transport parameters obtained in the absence of DMSO or NPs could predict the water transport response of the HeLa and Jurkat cells in the presence of NPs quite accurately, while the converse is not true.

2.4.4 Post-thaw Viability and Apoptotic Response

As stated earlier, we have performed several controlled-rate freezing (CRF) experiments on different treatments of HeLa and Jurkat cells. As shown in table 2.1, the predicted optimal cooling rates for HeLa and Jurkat cells can be broadly classified into two ranges: ~20–24 °C min^{-1} in the presence of either DMSO or NPs and ~30–34 °C min^{-1} in the absence of both DMSO and NPs. Thus, for the CRF experiments, we have chosen two cooling rates, 22 and 33 °C min^{-1}, along with an additional slow cooling rate of 1 °C min^{-1}. It was assumed that 22 °C min^{-1} was optimal for both HeLa and Jurkat cells treated with either DMSO or NPs and 33 °C min^{-1} was optimal for cells treated with only Opti-MEM. Finally 1 °C min^{-1} was presumed to be a damaging cooling rate for all treatments of HeLa and Jurkat cells.

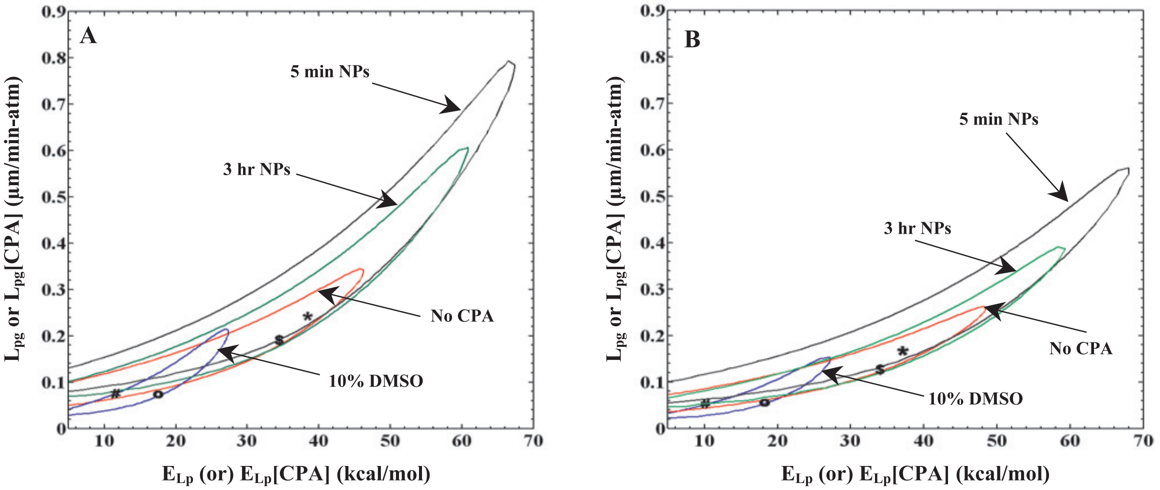

Figure 2.4 Contour plots of the goodness of fit parameter *R^2* (= 0.96) for water transport response in HeLa (A) and Jurkat (B) cells in the absence of CPAs, in the presence of DMSO and NPs. The common region corresponds to the range of parameters that "fit" the water transport data for different media with *R^2* ≥ 0.96. Note that the "best fit" parameters shown in table 1 are also shown in both the figures as either "#" (with DMSO), or "o" (without DMSO or NPs), or "$" (cells incubated with NPs for 3 hr) or "*" (cells incubated with NPs for 5 min). The membrane permeability at 0 ˚C, *L_{pg}* (or *$L_{pg}[cpa]$*) ($m^3\ N^{-1}s^{-1}$) is plotted on the y-axis while the apparent activation energy of the membrane, *E_{Lp}* (or *$E_{Lp}[cpa]$*) (kJ/mole) is plotted on the x-axis.

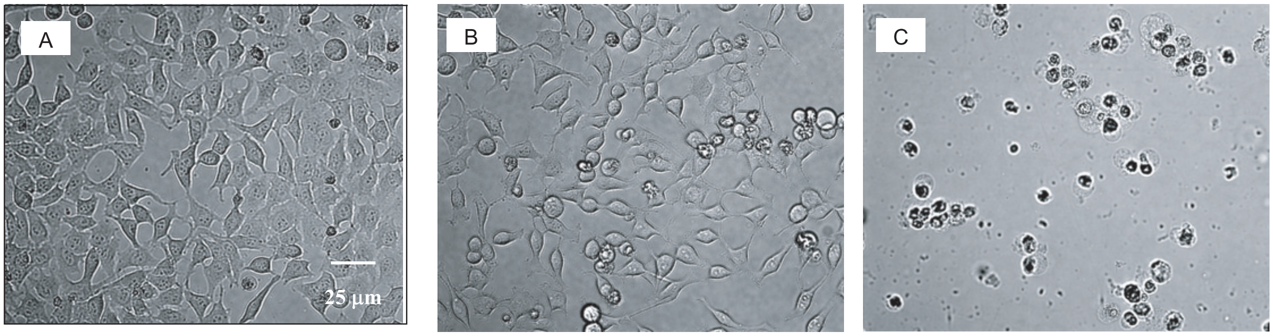

Figure 2.5 18 h post-thaw phase-contrast images (20×) of: (A) Control or non-frozen HeLa cells; (B) HeLa cells frozen in 10% DMSO at 22 ºC min^{-1}, and (C) HeLa cells incubated with NPs for 5 min and cooled at 22 ºC min^{-1}. Scale bar represents 25 µm.

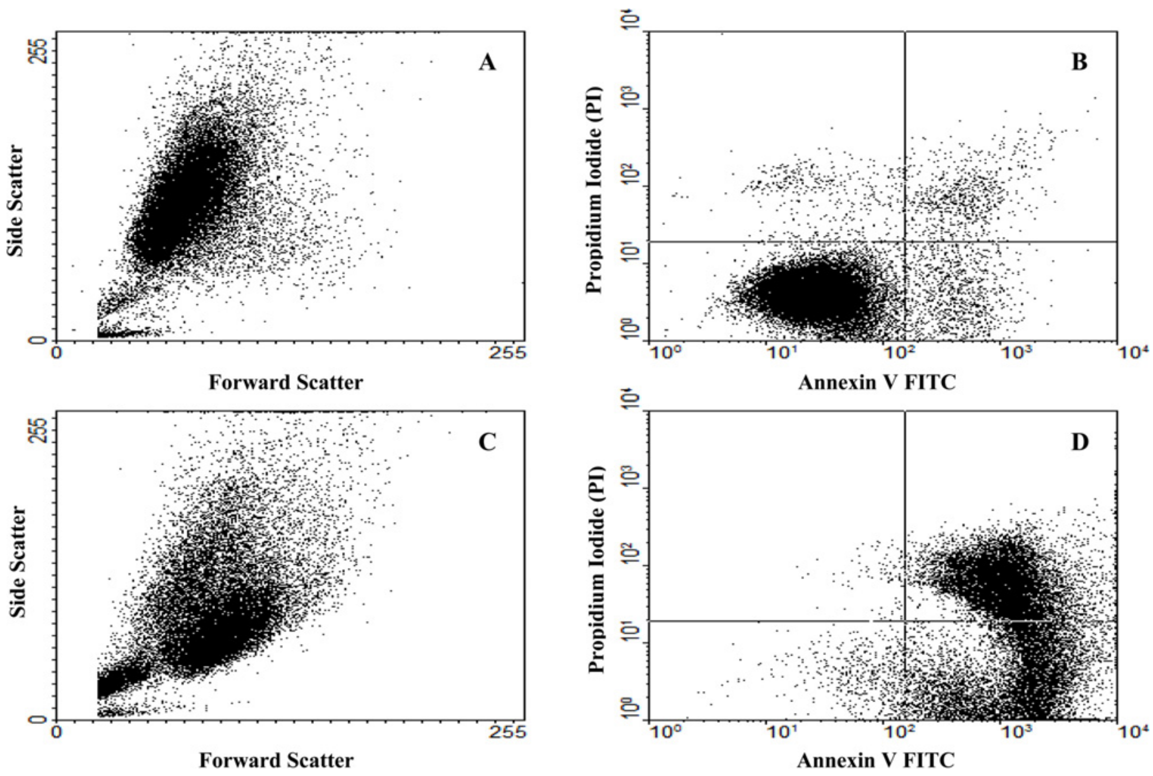

Figure 2.6 Characteristic cytometer scatterplots and fluorescence dotplots showing fluorescence-activated cell sorting (FACS) analysis of cell death after freezing determined by annexin V staining and PI-uptake for HeLa cells cooled at 22 ºC min-1: (A) scatterplot for HeLa cells frozen in the presence of 10% DMSO; (B) fluorescence dotplot for HeLa cells frozen in the presence of 10% DMSO; (C) scatterplot for HeLa cells incubated with NPs for 5 min; and (D) fluorescence dotplot for HeLa cells incubated with NPs for 5 min.

Table 2.2 Effect of different treatments with non-frozen and assay controls on resulting percentages of necrotic, live, and apoptotic HeLa cells according to the annexin V apoptosis assay protocol. Experiments were performed in triplicate, and data are expressed as mean ± SEM.

	% Necrotic (±stdev)	% Live (±stdev)	% Apoptotic (±stdev)
Non-frozen controls			
No CPA	$0.9^{\pm0.1}$	$89.5^{\pm1.3}$	$6.0^{\pm0.9}$
10% DMSO	$2.0^{\pm0.6}$	$87.6^{\pm2.2}$	$6.5^{\pm0.8}$
5 min NP	$1.2^{\pm0.3}$	$87.0^{\pm3.0}$	$5.9^{\pm0.8}$
3 h NP	$3.5^{\pm1.4}$	$81.7^{\pm4.4}$	$10.23^{\pm2.7}$
Assay controls			
Live (untreated control)	$1.7^{\pm0.5}$	$86.9^{\pm2.3}$	$6.4^{\pm1.4}$
Necrotic (H_2O_2 treated)	$51.3^{\pm10.7}$	$6.2^{\pm2.3}$	$8.7^{\pm3.4}$
Apoptotic (staurosporine treated)	$10.6^{\pm2.8}$	$48.9^{\pm5.7}$	$19.4^{\pm2.6}$

The controlled-rate freezing experiments were performed as detailed earlier in the methods section. Figure 2.5 shows the morphology of the HeLa cells incubated for 18 h post-thaw and illustrates the state of the cells after freezing in different media. The images are for HeLa cells cooled to −80 °C at 22 °C min^{-1} and thawed back to 37 °C at 200 °C min^{-1} and incubated for 18 h. The non-frozen control (figure 2.5(A)) shows attached HeLa cells with normal morphology as expected. The image of 10% DMSO-treated HeLa cells (figure 2.5(B)) shows that a substantial amount of cells have attached and survived the freeze–thaw protocol while there is only cellular debris and floating necrotic cells in the case of the 5 min NP treatment (figure 2.5(C)).

When the typically non-adherent Jurkat cells were treated with either no CPA, DMSO or NPs in Opti-MEM, they adhered to the culture plate. Despite strenuous efforts, we were unable either through enzymatic or mechanical means to disassociate and collect these adherent Jurkat cells. Hence Jurkat cells were not available for analysis of apoptosis through the flow cytometry assay. Therefore, all post-thaw behaviour was assessed only for HeLa cells. Characteristic scatter and fluorescence dotplots are shown in figure 2.6 for HeLa cells cooled at 22 °C min^{-1} to −80 °C. The scatterplot for HeLa cells frozen in the presence of 10% DMSO (figure 2.6(A)) reveals a homogeneous cell population. The scatterplot for HeLa cells treated with NPs for 5 min and then frozen (figure 2.6(C)) reveals an increase in cell fragments as indicated by the appearance of the population with low forward scatter (FSC) and low side scatter (SSC). Additionally, the increase in internal granularity (increase in SSC) reveals the deteriorating physical condition of HeLa cells frozen with NPs (figure 2.6(C)). The fluorescence dotplot for HeLa cells frozen in the presence of 10% DMSO (figure 2.6(B)) shows a majority of the cells are in the lower left quadrant (annexin V–/ *PI–*), which corresponds to the live cell population. Conversely, the fluorescence dotplot for HeLa cells treated with NPs for 5 min and then frozen (figure 2.6(D))

shows a majority of the cells are either in the lower right quadrant (annexin V^+/PI^-, apoptotic) or in the upper right quadrant (annexin V^+/PI^+,necrotic). This population quadrant analysis was performed on all of the experimental treatments to obtain quantitative information on the condition of the cells following the freeze–thaw protocol described earlier (figure 2.7).

After the 18 h incubation period following the freeze–thaw experiment, the percentages of necrotic, live and apoptotic HeLa cells were determined (figure 2.7). No significant difference was found among the non-frozen controls (table 2.2), indicating that treatment with 10% DMSO or nanoparticles alone was not cytotoxic. The percentage of live, necrotic and apoptotic HeLa cells are shown for the four treatments and the three cooling rates investigated: live (figure 2.7(A)), necrotic (figure 2.7(B)) and apoptotic (figure 2.7(C)). There was no significant difference in the post-thaw survival of 10% DMSO treatments at the three cooling rates studied (figure 2.7(A)). This result is not surprising since the HeLa cell line is a robust, widely used immortalized cell line that laboratories commonly store frozen in liquid nitrogen. McGrath *et al* (McGrath et al. 1975) reported similar data indicating no statistically significant difference in the survival of HeLa cells cooled to −20 °C at rates of 5, 20 and 30 °C min^{-1}.

HeLa cells treated with NPs for 5 min and then cooled at 1 °C min^{-1} had significantly more apoptotic cells (75 ± 1.5%) when compared to apoptotic cells at the faster cooling rates of either 22 °C min^{-1} (44 ± 5.3%) or 33 °C min^{-1} (36 ± 7%). Interestingly, for HeLa cells treated with NPs and then frozen, we observed a significant increase in the percentage of necrotic cells accompanied by a corresponding decrease in the percentage of apoptotic cells, when the cooling rate is increased from 1 to 22 °C min^{-1}. In the absence of cryopreservative agents, the percentage of apoptotic HeLa cells significantly decreases as the cooling rate increases from 1 °C min^{-1} (71 ± 2.1%) to 33 °C min^{-1} (41 ± 2.8%). This suggests that the mechanism of cell death for

the slower rate (1 °C min^{-1}) differs from the faster cooling rates in which there is a reduced percentage of apoptotic cells. Conversely, HeLa cells treated with NPs for 3 h and then frozen, exhibited a significantly higher survival at 33 °C min^{-1} (12 ± 2.1% live) compared to 1 °C min^{-1} (4 ± 0.4%). HeLa cells treated with 10% DMSO and then frozen were found to have significantly higher percentages of surviving cells at all three cooling rates when compared to the other treatments (see figure 2.7), although a cursory examination of figure 2.7(A) might suggest an improved post-thaw viability for cells cooled at 33 °C min^{-1} in the presence of NPs (5 min incubation) and also in the absence of CPAs. However, a closer examination of the data revealed that this seemingly significant improvement in post- thaw cell viability was actually not statistically significant. And finally, for the 10% DMSO treatments, 20000 cell events were collected for all freezing rates; however, in the absence of DMSO and NPs, fewer cell events were collected (ranging from 1100 to 11 000) which is an indication of cell rupturing and increased cellular debris following the freeze–thaw protocol. Based on the quantitative post-thaw data, there are no significant differences between cells treated with nanoparticles and in the absence of CPAs, which suggests that the nanoparticles do not provide any significant cryoprotective function to HeLa cells at the concentration of NPs used and freeze–thaw rates studied here.

2.5 Discussion

In order to determine the water transport parameters and optimal cooling rates across cellular treatments in this study, cell dimensions and inactive cell volumes of HeLa and Jurkat cells were obtained in this study. The cell diameter values for HeLa (~15 μm) and Jurkat (~12 μm) obtained in the present study are comparable to those reported in the literature; ~14–16 μm for HeLa cells (Deman and Bruyneel 1977; Nair 1981) and ~10–13 μm for Jurkat cells

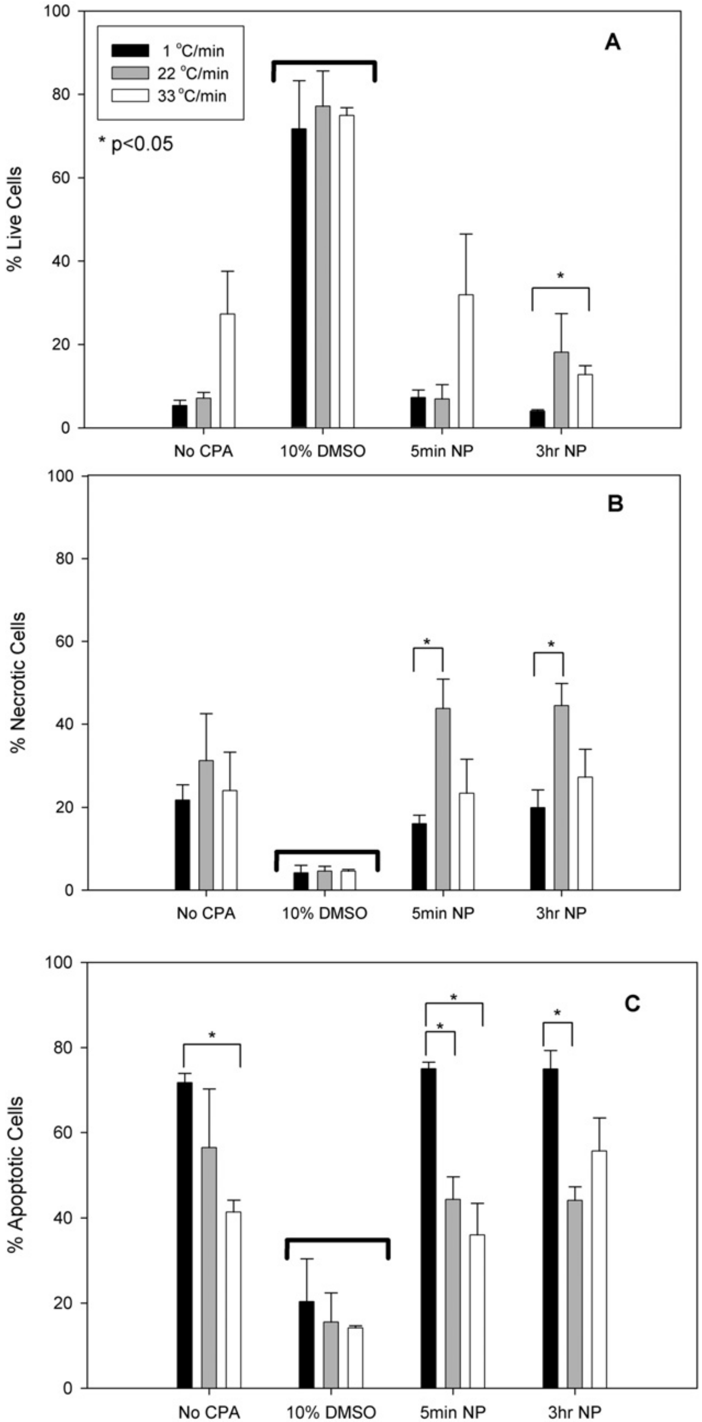

Figure 2.7 18 h post-thaw comparison of percentage of live, necrotic, and apoptotic HeLa cells are shown for the four treatments and the three cooling rates investigated: live (A), necrotic (B), and apoptotic (C). The error bars represent the standard error in the data. The horizontal bars denoted with asterisks (*) represent statistically significant differences between similar treatments. The bold horizontal bars above 10% DMSO data in all panels represents a significant difference from the corresponding data obtained for the other three treatments.

(Rosenbluth et al. 2006). Conversely, a lower average diameter value of the order of ~8 μm was reported by Chen *et al* (Chen et al. 2004) for Jurkat cells while a higher average diameter of ~20 μm was reported by Morrill and Robbins (Morrill and Robbins 1984) for HeLa cells. The inactive cell volume for the Jurkat cell obtained in this study (~$0.52V_o$) is comparable to a published value of $0.48V_o$ (Reuss et al. 2004). However, there is significant difference between the measured value of inactive cell volume of HeLa cells (~$0.45V_o$) in our experiment and the published value of $V_b = 0.21V_i$ by Morrill and Robbins (Morrill and Robbins 1984). These variations in cell size and hence the inactive cell volumes might be due to the growth conditions employed for HeLa cells at different laboratories (Masters 2002).

There was a significant increase in the measured values of reference membrane permeability, L_{pg} (or L_{pg} [cpa]) and activation energies E_{Lp} (or E_{Lp} [cpa]) obtained in the presence of NPs when compared with the corresponding values obtained in their absence for both HeLa and Jurkat cells (see table 2.1). Interestingly, there are no significant differences in the permeability values obtained in the presence of DMSO and in the absence of DMSO and NPs for both HeLa and Jurkat cells (table 2.1). However, there was a considerable increase in the measured activation energy values in the presence of DMSO and in the absence of DMSO and NPs. For both HeLa and Jurkat cells, the time of incubation (either 5 min or 3 h) with NPs did not show any marked effect on the water transport behaviour and thus there are no significant differences (<17%) in the L_{pg} (or L_{pg}[cpa]) and E_{Lp} (or E_{Lp}[cpa]) values in the presence and absence of NPs (table 2.1).

As stated earlier, the best-fit permeability parameters and the measured $\left(\frac{A_c}{V_o - V_b}\right)$ values were incorporated into equation (2.4) to predict the optimal rates of freezing for both HeLa and

Jurkat cells (table 2.1). It should be noted that, in the development of equation (2.4), the dynamics and kinetics of IIF have not been included (Toner 1993). Thus, if IIF occurs between −5 and −20 °C, then potentially even more water will be trapped in the HeLa and Jurkat cells than predicted by water transport alone and the optimal cooling rates obtained using equation (2.4) are overestimated. An examination of the optimal cooling rates reveals that, despite significant differences in the water transport behaviour and hence the permeability parameters obtained in the presence of NPs versus DMSO, the optimal cooling rates are statistically similar, if not exactly the same, for both HeLa and Jurkat cells. However, for both cell types, the optimal cooling rate measured in the absence of NPs or DMSO is significantly higher (30–40%). This is somewhat surprising, as the presence of CPAs are expected to increase the ability of the cell membrane to dehydrate at faster cooling rates (Smith et al. 1998). However a similar decrease in the predicted optimal cooling rates in the presence of CPAs was observed in canine spermatozoa (Thirumala et al. 2003), adipose tissue derived adult stem cells (Thirumala et al. 2005a) and in striped bass sperm cells (Thirumala et al. 2006).

An interesting phenomenon observed in this study was the atypical behaviour of lymphocytic Jurkat cells adhering to the culture plate when they were incubated in Opti-MEM and treated with NPs or DMSO. Results from MTT viability assays suggest that these cells are metabolizing and thus alive (data not shown). There are no published reports of Jurkat cells adhering to substrates other than specific ligands (e.g. fibronectin) or stimulated endothelial cells. A distinct possibility for the adherent behaviour of Jurkat cells could be due to possible stimulating factors present in Opti-MEM and the surface treatment of the culture plate. This is somewhat supported by the observed behaviour of Jurkat cells frozen and incubated in the absence of CPAs. However, there are several published reports of Jurkat cells cultured in Opti-

MEM that do not exhibit this adherent behaviour (Cui et al. 2003; Fadok et al. 2000; Sanders et al. 2000). Further understanding is needed to evaluate the Jurkat cell adhesion observed here and to distinguish between competing or complementary modes of the substrate and media in stimulating adhesion.

As shown in figure 2.7 and described earlier, NPs do not seem to provide any significant cryoprotective function to HeLa cells at the concentrations and freeze–thaw rates investigated in the present study. We have postulated several likely reasons for NPs not showing any cryoprotection. Firstly, the concentration of the NPs used in this study was lower than necessary to achieve some measurable cryoprotective effect. A thorough review of the literature suggests that cryoprotection by high molecular mass materials like polymers is feasible only at very high concentrations. These non-permeable polymeric CPA solutions act on a colligative basis and tend to have increasingly high viscosities at lower temperatures and form glasses readily at high temperatures by kinetically slowing down the ice crystal growth to zero (Connor and Ashwoods.Mj 1973). Moreover, all CPAs showing some cryoprotection do share a common characteristic of freezing-point depression (FPD) (Bischof 2006; Fuller 2004). FPD of polymers show a marked deviation from the linear relationship and increase dramatically at high concentrations. In our experiments with 10% NPs we observed essentially zero FPD, and the NP solution behaved like an isotonic solution. Conversely, a recent study suggested that the use of 10% polyvinylpyrrolidone (PVP) as CPA dramatically increased post-thaw survival of porcine primary adipocytes more than that could be achieved with 10% DMSO as the sole CPA (Li et al. 2006). Further studies are clearly needed to reconcile these disparate observations.

A second explanation for the minimal cryopreservative effect from NPs is that the water transport model for determining optimal cooling rates may not accurately predict the water

transport across the cell membrane when the freezing medium contains NPs. This suggests that further modifications and corrections might be needed to the water transport model (equations (2.1) and (2.2)) to enable it to accurately reflect cell freezing behaviour in the presence of NPs. For the purposes of this study, the use of the standard water transport model (equations (2.1, 2.2)) was deemed to be sufficient. However, efforts are currently underway in our laboratory to elucidate the necessary modifications to the water model and to further its use in the presence of NPs.

And finally, the palmitoyl NPs might not possess any cryoprotective action at lower temperatures and in fact might be having the opposite effect. For example, the post-thaw apoptotic response of HeLa cells indicates that the presence of NPs induces a significant increase in apoptosis at low freezing rates (1 °C min^{-1}) when compared to higher freezing rates (figure 2.7). As stated earlier, an increase in the cooling rate from 1 to 22 °C min^{-1} was accompanied with a significant increase in % necrotic HeLa cells treated and frozen with NPs. This striking result does suggest that NPs could be effective as an adjuvant to cryodestructive procedures. Interestingly, the presence of NPs significantly increased the percentage of apoptotic cells cooled at 1 °C min^{-1} (figure 2.7), a cooling rate that is similar to those experienced at the outer edges of a cryosurgical iceball where cell survival is typically the highest. However, it is important to note that a comparison of the % of apoptotic cells found when HeLa cells are frozen in the absence of CPAs and NPs is comparable to that obtained for HeLa cells frozen in the presence of NPs (figure 2.7) at the three cooling rates investigated and the volume fraction of NPs. As shown in table 2.2, in the absence of freezing temperatures, the presence of NPs during incubation was not cytotoxic and further encourages the use of palmitoyl NPs for *in vivo* applications. Similar non-

cytotoxic nature of gold nanoparticles, when incubated with human fibroblasts, was also reported by de la Fuente *et al* (de la Fuente et al. 2006).

Our observations suggest that the gold NPs used in our study are interacting with HeLa cells by some physiochemical means and are inducing apoptosis during the freeze–thaw process. This encourages the possibility of using gold NPs in a cryodestruction procedure and is supported by recent studies demonstrating that nanoparticles can potentially enhance and control thermal therapy outcomes through adjuvant (drug) delivery, tomographic visualization and inductive heating within the body (Bischof 2006). Since maximizing the killing effect of cryosurgery has been an important task both for clinical practice and for fundamental research, the association of apoptosis with NPs at low temperatures observed in the present study is of direct relevance for cryosurgical applications.

2.6 Conclusion

The aim of this study was to evaluate the freezing response of HeLa and Jurkat cells in the presence of commercially available nanoparticles, NPs (Palmitoyl Nanogold®, Nanoprobes) and a commonly used cryoprotective agent, DMSO. By fitting a model of water transport to the experimentally determined volumetric shrinkage data, the membrane permeability parameters were obtained. A generic optimal cooling rate equation was then used to predict the optimal rates of freezing HeLa and Jurkat cells in the presence and absence of DMSO and NPs. To further investigate the predicted optimal cooling rates, the cells were cooled at three controlled freezing rates in the presence and absence of DMSO and NPs using a commercially available controlled rate freezer. The post-thaw viability and apoptotic response of treated HeLa cells were evaluated after 18 h post-thaw incubation time. Jurkat cells demonstrated an increase in their adhesion after treatment and remain adhered to the culture plate, preventing their flow cytometric analysis.

For HeLa cells**,** the post-thaw results show that the presence of NPs increased the measured post-freeze apoptotic response at 1 °C min^{-1} when compared to higher cooling rates and suggests a possible therapeutic use of NPs in cryodestructive procedures.

2.7 References

Anchordoguy TJ, Rudolph AS, Carpenter JF, Crowe JH. 1987. Modes of interaction of cryoprotectants with membrane phospholipids during freezing. Cryobiology 24(4):324-331.

Arakawa T, Timasheff SN. 1985. The stabilization of proteins by osmolytes. Biophysical Journal 47(3):411-414.

Ashwoods M, Becker G, Warby C, Connor W. 1972. Protective action of various polymers, including polyvinylpyrrolidone, dextran, and hydroxyethyl starch against freezing damage to mammalian cells in tissue culture. Cryobiology 9(4):311.

Balakin KV, Savchuk NP, Tetko IV. 2006. In silico approaches to prediction of aqueous and DMSO solubility of drug-like compounds: Trends, problems and solutions. Current Medicinal Chemistry 13(2):223-241.

Baust JM, Van B, Baust JG. 2000. Cell viability improves following inhibition of cryopreservation-induced apoptosis. In Vitro Cell Dev Biol Anim 36(4):262-70.

Bevington P, Robinson D. 1992. Data Reduction and Error Analysis for the Physical Sciences. New York: McGraw-Hill College.

Bischof JC. 2006. Micro and nanoscale phenomenon in bioheat transfer. Heat and Mass Transfer 42(10):955-966.

Brewer JM, Pollock KGJ, Tetley L, Russell DG. 2004. Vesicle size influences the trafficking, processing, and presentation of antigens in lipid vesicles. Journal of Immunology 173(10):6143-6150.

Chen G, Chen N, Garner A, Kolb J, Swanson R, Beebe S, Joshi R, Schoenbach K. Conductivity in Jurkat cell suspension after ultrashort electric pulsing in; 2004; Kos, Greece. p 56-65.

Connor W, Ashwoods.Mj. 1973. Cryoprotection of mammalian cells in tissue-culture with polymers- possible mechanisms. Cryobiology 10(6):488-496.

Crowe JH, Carpenter JF, Crowe LM, Anchordoguy TJ. 1990. Are freezing and dehydration similar stress vectors- a comparison of modes of interaction of stabilizing solutes with biomolecules. Cryobiology 27(3):219-231.

Cui CB, Cooper LF, Yang XL, Karsenty G, Aukhil I. 2003. Transcriptional coactivation of bone-specific transcription factor Cbfa1 by TAZ. Molecular and Cellular Biology 23(3):1004-1013.

Daniel MC, Astruc D. 2004. Gold nanoparticles: Assembly, supramolecular chemistry, quantum-size-related properties, and applications toward biology, catalysis, and nanotechnology. Chemical Reviews 104(1):293-346.

de la Fuente JM, Berry CC, Riehle MO, Curtis ASG. 2006. Nanoparticle targeting at cells. Langmuir 22(7):3286-3293.

Deman JJ, Bruyneel EA. 1977. Thermal transitions in adhesiveness of HeLa cells- effects of cell-growth, trypsin treatment and calcium. Journal of Cell Science 27(OCT):167-181.

Devireddy RV, Fahrig B, Godke RA, Leibo SP. 2004. Subzero water transport characteristics of boar spermatozoa confirm observed optimal cooling rates. Molecular Reproduction and Development 67(4):446-457.

Devireddy RV, Raha D, Bischof JC. 1998. Measurement of water transport during freezing in cell suspensions using a differential scanning calorimeter. Cryobiology 36(2):124-155.

Diller KR. 2005. Bioheat and mass transfer as viewed through a microscope. Journal of Biomechanical Engineering-Transactions of the ASME 127(1):67-84.

Fadok VA, Bratton DL, Rose DM, Pearson A, Ezekewitz RAB, Henson PM. 2000. A receptor for phosphatidylserine-specific clearance of apoptotic cells. Nature 405(6782):85-90.

Fahy GM. 1986. The relevance of cryoprotectant toxicity to cryobiology. Cryobiology 23(1):1-13.

Farrant J. 1969. Is there a common mechanism of protection of living cells by polyvinylpyrrolidone and glycerol during freezing. Nature 222(5199):1175-&.

Fowler A, Toner M. Cryo-injury and biopreservation. In: Lee RC, Despa F, Hamann KJ, editors; 2005. New York Acad Sciences. p 119-135.

Fuller BJ. 2004. Cryoprotectants: The essential antifreezes to protect life in the frozen state. Cryoletters 25(6):375-388.

Hainfeld JF, Powell RD. New frontiers in gold labeling; 2000. Histochemical Soc Inc. p 471-480.

Hollister WR, Aby J. Mathew, John G. Baust, and Robert G. Van Buskirk. 1998. Effects of Freezing on Cell Viability and Mechanisms of Cell Death in a Human Prostate Cancer Cell Line. Molecular Urology 2(1):13-18.

Karow AM. 1991. Chemical cryoprotection of metazoan cells. Bioscience 41(3):155-160.

Kedem O, Katchalsky A. 1958. Thermodynamic analysis of the permeability of biological membranes to non-electrolytes. Biochimica Et Biophysica Acta 27(2):229-246.

Koopman G, Reutelingsperger CPM, Kuijten GAM, Keehnen RMJ, Pals ST, Vanoers MHJ. 1994. Annexin-V for Flow Cytometric Detection of Phosphatidylserine Expression on B-Cells Undergoing Apoptosis. Blood 84(5):1415-1420.

Levin RL, Cravalho EG, Huggins CE. 1976. Membrane model describing effect of temperature on water conductivity of erthryocyte-membranes at subzero temperatures. Cryobiology 13(4):415-429.

Li Y, Lu RH, Luo GF, Pang WJ, Yang GS. 2006. Effects of different cryoprotectants on the viability and biological characteristics of porcine preadipocyte. Cryobiology 53(2):240-247.

Lovelock JE. 1954. The protective action of neutral solutes against haemolysis by freezing and thawing. Biochemical Journal 56(2):265-270.

Lucke B, McCutcheon M. 1932. The living cell as an osmotic system and its permeability to water. Physiological Reviews 12(1):0068-0139.

Masters JR. 2002. HeLa cells 50 years on: the good, the bad and the ugly. Nature Reviews Cancer 2(4):315-319.

Mathew AJ, Baust JG, Van Buskirk RG. 1997. Optimization of hypothermosol for the hypothermic storage of cardiac cells - Addition of EDTA. In Vitro Toxicology 10(4):407-415.

Mazur P. 1960. Physical factors implicated in the death of microorganisms at subzero temperatures. Annals of the New York Academy of Sciences 85(2):610-629.

Mazur P. 1963. Kinetics of water loss from cells at subzero temperatures and likelihood of intracellular freezing. Journal of General Physiology 47(2):347-&.

McGrath JJ, Cravalho EG, Huggins CE. 1975. Experimental comparison of intracellular ice formation and freeze-thaw survival of HeLa S-2 cells. Cryobiology 12(6):540-550.

Meryman HT. 1974. Freezing injury and its prevention in living cells. Annual Review of Biophysics and Bioengineering 3:341-363.

Morrill GA, Robbins E. 1984. Changes in intracellular cations during the cell-cyle in HeLa cells. Physiological Chemistry and Physics and Medical Nmr 16(3):209-219.

Nair CN. 1981. Mon-valent cation metabolism and cytopathic effects of poliovirus-infected HeLa cells. Journal of Virology 37(1):268-273.

Nash T. 1966. Chemical constitution and physical properties of compounds able to protect living cells against damage due to freezing and thawing. In: Meryman HT, editor. Cryobiology. New York: Academic Press.

Pegg DE. 2002. The history and principles of cryopreservation. Seminars in Reproductive Medicine 20(1):5-13.

Pena FJ, Johannisson A, Wallgren M, Rodriguez-Martinez H. 2003. Assessment of fresh and frozen-thawed boar semen using an Annexin-V assay: a new method of evaluating sperm membrane integrity. Theriogenology 60(4):677-689.

Polge C, Smith AU, Parkes AS. 1949. Revival of spermatozoa after vitrification and dehydration at low temperatures. Nature 164(4172):666-666.

Rall WF. 1987. Factors affecting survival of mouse embryos cryopreserved by vitrification. Cryobiology 24(5):387-402.

Resh MD. 1999. Fatty acylation of proteins: new insights into membrane targeting of myristoylated and palmitoylated proteins. Biochimica Et Biophysica Acta-Molecular Cell Research 1451(1):1-16.

Reuss R, Ludwig J, Shirakashi R, Ehrhart F, Zimmermann H, Schneider S, Weber MM, Zimmermann U, Schneider H, Sukhorukov VL. 2004. Intracellular delivery of carbohydrates into mammalian cells through swelling-activated pathways. Journal of Membrane Biology 200(2):67-81.

Rosenbluth MJ, Lam WA, Fletcher DA. 2006. Force microscopy of nonadherent cells: A comparison of leukemia cell deformability. Biophysical Journal 90(8):2994-3003.

Rudolph AS, Crowe JH. 1985. Membrane stabiliization during freezing- the role of 2 natural cryoprotectants, trehalose and proline. Cryobiology 22(4):367-377.

Sanders SK, Crean SM, Boxer PA, Kellner D, LaRosa GJ, Hunt SW. 2000. Functional differences between monocyte chemotactic protein-1 receptor A and monocyte chemotactic protein-1 receptor B expressed in a Jurkat T cell. Journal of Immunology 165(9):4877-4883.

Smith DJ, Schulte M, Bischof JC. 1998. The effect of dimethylsulfoxide on the water transport response of rat hepatocytes during freezing. Journal of Biomechanical Engineering-Transactions of the Asme 120(5):549-558.

Takahashi T, Hirsh A, Erbe E, Williams RJ. 1988. Mechanism of cryoprotection by extracellular polymeric solutes. Biophysical Journal 54(3):509-518.

Thirumala S, Campbell WT, Vicknair MR, Tiersch TR, Devireddy RV. 2006. Freezing response and optimal cooling rates for cryopreserving sperm cells of striped bass, Morone saxatilis. Theriogenology 66(4):964-973.

Thirumala S, Devireddy RV. 2005. A simplified procedure to determine the optimal rate of freezing biological systems. Journal of Biomechanical Engineering-Transactions of the Asme 127(2):295-300.

Thirumala S, Ferrer MS, Al-Jarrah A, Eilts BE, Paccamonti DL, Devireddy RV. 2003. Cryopreservation of canine spermatozoa: theoretical prediction of optimal cooling rates in the presence and absence of cryoprotective agents. Cryobiology 47(2):109-124.

Thirumala S, Gimble JM, Devireddy RV. 2005a. Transport phenomena during freezing of adipose tissue derived adult stem cells. Biotechnology and Bioengineering 92(3):372-383.

Thirumala S, Zvonic S, Floyd E, Gimble JM, Devireddy RV. 2005b. Effect of various freezing parameters on the immediate post-thaw membrane integrity of adipose tissue derived adult stem cells. Biotechnology Progress 21(5):1511-1524.

Toner M. 1993. Nucleation of ice crystals in biological cells. In: Steponkus PL, editor. Advances in Low-Temperature Biology. London: JAI Press. p 1-52.

Wehner F, Olsen H, Tinel H, Kinne-Saffran E, Kinne RKH. 2004. Cell volume regulation: osmolytes, osmolyte transport, and signal transduction. Reviews of Physiology, Biochemistry and Pharmacology, Vol 148. Berlin: Springer-Verlag Berlin. p 1-80.

Williams RJ. 1983. The surface-activity of PVP and other polymers and their antihemolytic capacity. Cryobiology 20(5):521-526.

Williams RJ, Harris D. 1977. Distribution of cryoprotective agents into lipid interfaces. Cryobiology 14(6):670-680.

Yancey PH. 2005. Organic osmolytes as compatible, metabolic and counteracting cytoprotectants in high osmolarity and other stresses. Journal of Experimental Biology 208(15):2819-2830.

Yu TH, Liu J, Zhou YX. 2005. Selective freezing of target biological tissues after injection of solutions with specific thermal properties. Cryobiology 50(2):174-182.

Yuan S, KR D. Study of freezing biological systems using optical differential scanning calorimeter; 2001; Snowbird, UT. p 117-118.

CHAPTER 3. CHARACTERIZATION AND APPLICATIONS OF SERUM-FREE INDUCED ADHESION IN SUSPENSION CELLS

3.1 Introduction

In this study, we demonstrate that the serum content of different media plays an important role in inducing reversible cell adhesion. Adhesion of Jurkat cells in two distinct media formulations (serum-fortified and serum-free) to untreated polystyrene (PS), plasma-treated PS, and fibronectin-coated PS was compared. Additional analysis characterized the occurrence of this transient cell adhesion, including attachment rate, reversibility of attachment, and viability and preservation of phenotype in cells during and after attachment. As a demonstration of the utility of this technique, a few applications of adhered suspension cells in gene delivery, apoptosis detection, and electric-field effects studies are shown to be feasible using this approach, which would be otherwise difficult with freely-suspended cells.

The integration of non-adherent cell lines into increasingly more complex systems is limited by technologies used to attach them to a surface without altering their physiology. Techniques have been developed to orient suspension cell lines, but often only at the expense of disrupting their function (Malek and Fleming 1994; Manca et al. 1991; Wennemuth et al. 1998; Zell et al. 1999). These methods include suction (Deutsch and Weinreb 1994; Khine et al. 2005), centrifugal forces (Biran and Walt 2002), and artificial cell tethering (Shapiro and Hsu 1989). Suspension cell localization has also been directed by microstructures and surface modifications (Bratten et al. 1997; Deutsch et al. 2006; Inoue et al. 2001; Tan et al. 2001). These methods are often costly, time-consuming, not readily adaptable to structures of varying shape, and may not be amenable to reversible adhesion.

The ability to anchor normally non-adherent cells for a period of time onto a surface could prove useful for a number of cell culture assays. Transiently attaching suspension cell lines to a substrate has broad applications, such as implementing suspension cells into patterning schemes (Abhyankar and Beebe 2007). Suspension cell attachment is also critical to cell-biomaterial studies, in which these interactions have been characterized by adhesion assays and shear stress studies (Bergman and Zygourakis 1999; Lloyd et al. 1996; Neugebauer and Reichardt 1991). Additionally, transiently-adhered suspension cells could be used for tissue engineering applications, such as incorporation into scaffolding (Saim et al. 2000). Finally, tethered suspension cells may be utilized in lipid transfection, which is improved by adhesion (Keller et al. 1999). The capacity to adhere normally suspended cells enables their use in a wider range of biomedical, genetic engineering, and cellular studies that would otherwise be difficult.

The goal of this project was to better characterize the effect of serum on Jurkat cells adhering to different substrates. Jurkat lymphocytic cells, derived from human T-cell leukemia, are one of the most widely-used suspension cell lines, utilized in studies varying from anticancer drugs (Ko et al. 2000; Nyakern et al. 2006) to electric-field treatments (Deng et al. 2003; Frey et al. 2006; Vernier et al. 2004; Vernier et al. 2003). Lymphocytes, in particular, have been shown to be sensitive to surface protein concentrations and configurations related to adhesion and migration patterns (Bergman and Zygourakis 1999; Dimilla et al. 1992; Lawson and Maxfield 1995). Components of the cellular environment are particularly important in maintaining phenotypic characteristics of lymphocytes, known to activate and differentiate in response to various molecular signals. The protein conformation characteristic of the material's surface may incur an immune response as the cells recognize it as foreign (Rouhi 1999); therefore, the

reaction of immune system cells to foreign bodies must be considered while studying non-adherent immunological cell lines in drug discovery, cell therapy, and cell-based applications.

The observation of suspension Jurkat cells adhering to a tissue-treated substrate is an interesting phenomenon found when Jurkat cells are incubated in serum-free medium conditions. This atypical observation of lymphocytic Jurkat cells in OptiMEM-I, a type of serum free medium commonly used for cell imaging and lipid transfection procedures, was first observed in a study evaluating the behavior of cells in the presence of nanoparticles incubated in serum-free media (Thirumala 2007). No reports have characterized the transient adhesion of Jurkat cells, yet it has been noted in one case that seeding nonadherent cells in serum-free media and allowing them to settle and affix to the surface can form a loosely associated monolayer (LI-COR_Biosciences 2006). Despite this note, there are studies conducted with Jurkat cells in serum-free medium that do not reference any observed cell adherence (Li et al. 2002; Sun et al. 2006). Zhu and Joyce (2004) report that OptiMEM-I was found to promote human corneal endothelial cell (HCEC) attachment and induce a moderate proliferative response, as compared to typical culture media (Zhu and Joyce 2004). Nonetheless, serum-free media influences the adhesive behavior of the cells, likely depending on the cell type and substrate conditions.

Taken collectively, the literature points to the interaction between the presence of serum and the behavior of nonadherent cells. This is an important effect that has not been well-characterized. Chau and colleagues reviewed relevant supplemental components of serum-free media and how they influence cell growth rates and monoclonal antibody secretion of hybridoma culture (Glassy et al. 1988). Effects of serum on adhesion were the focus of Bradley and colleagues' work, showing that serum decreased Chinese hamster ovary (CHO) cell attachment to tissue culture polystyrene (Teare et al. 2001). There are few studies other than this particular

CHO study that specifically examine immediate modes of cell attachment on the order of minutes, rather than hours or days. While adhesive behavior and presence of serum on various adherent cell types (CHO, HCEC) is briefly mentioned as asides within more extensive, unrelated cell studies noted above, no detailed analysis of suspension cells serum-free media has yet been reported.

In this study we demonstrate that the serum content of different media plays an important role in induced-adhesion of suspension cells. The specific objectives were to characterize the adhesion of Jurkat cells in serum-fortified and serum-free conditions; to determine if this adhesion effect can be reversed; to examine uplifted cell behavior; and to demonstrate applications of this transient, serum-dependent adhesion for single-cell imaging analysis and improved gene delivery to suspension cells.

3.2 Materials and Methods

3.2.1 Cell Culture

Jurkat T lymphocyte cells (E6.1, ATCC) were maintained in 25 cm^2 flasks (BD Falcon, Franklin Lakes, NJ) with 5 mL of classical RPMI-1640 (RPMI) supplemented with 10% fetal bovine serum (FBS) and were incubated at 37°C in a humidified atmosphere containing 5% CO_2. HeLa cells (human epithelial carcinoma cells, American Type Culture Collection) were maintained in 25 cm^2 flasks (BD Falcon, Franklin Lakes, NJ) with 5 mL of Dulbecco's Modified Eagle's medium-reduced serum (DMEM-RS) supplemented with 3% fetal bovine serum (FBS) and incubated at 37 °C in a humidified atmosphere containing 5% CO_2. Opti-MEM® (Invitrogen) was a serum-free medium which was used for some of the experiments. Adhesion experiments were carried out in the presence and absence of FBS on Jurkat cells. Prior to all adhesion experiments, Jurkat cell concentrations were determined using a hemacytometer. All samples

used in the experiments were concentrated by centrifugation at 400xg for 5 min and resuspended in their respective media treatment to obtain a concentration of 1.6×10^6 cells/mL.

3.2.2 Brightfield Phase-contrast and Fluorescence Microscopy Imaging

For each of the adhesion experiments described, Jurkat cells were imaged by brightfield phase-contrast microscopy at 10X or 20X magnification. Images were acquired with an inverted Eclipse TS-100 Nikon Fluorescence microscope and a CoolSnapFX camera (Photometrics, Tucson, AZ). Fluorescent image processing was performed using MetaVue software (Universal Imaging Corporation, West Chester, PA).

3.2.3 Qualitative and Quantitative Representation of Attached Cells on Different Substrates

Cell adhesion assays were conducted on standard tissue culture polystyrene surfaces (Falcon, Franklin Lakes, NJ), untreated polystyrene surfaces (Nunc, Roskilde, Denmark), and fibronectin-coated (BD Biosciences, San Jose, CA) standard tissue culture polystyrene surfaces. Fibronectin is an absorbed extracellular matrix of proteins that promotes cell adhesion, for which a direct correlation has been found between the concentration of fibronectin on a surface and the percentage of Jurkat cells attached (Bergman and Zygourakis 1999). Jurkat E6.1 cells were seeded in 12-well plates in either RPMI (Hyclone, Logan, UT) medium with 10% fetal bovine serum, RPMI without serum, OptiMEM-reduced serum (Invitrogen Corporation, Carlsbad, CA), and OptiMEM with 10% fetal bovine serum. Cells were incubated for a period of one hour in 12-well plates, except in the time-course studies showing rapid attachment. After incubation, wells were aspirated and washed once with Calcium-Magnesium- free PBS. Brightfield microscopic images of precisely the same field of view, marked at the base of the dish by crosshairs etched with a razor blade, were taken prior to and following media removal. Images were acquired at 10X magnification from two distinct regions of at least three wells for each trial (n=6). Cell

counts were then conducted with image-processing NIH Image and Image J software (Wayne Rasband, NIH, MD) using the “Cell Counter” plug-in to gather quantitative data. The cell counts derived from these images are represented on a per area (cells/mm^2 with an imaged area of 0.59 mm^2) basis. All values are indicated as mean± SEM. Student’s t-test was employed, with $p \leq 0.05$ considered to be significant. Each “n” replicate was composed of a single image, and each treatment was conducted in triplicate.

3.2.4 Time-course of Adhesion for Serum-free OM and RPMI

Jurkat cells were seeded in tissue culture polystyrene wells for a period of 0, 5, 15, 30, and 60 minutes. For each time point, the cell wells were aspirated, washed with Ca-, Mg-free PBS, and imaged for subsequent analysis using the aforementioned cell count methods.

3.2.5 Time-course of Uplift for Resuspension in Serum-fortified Media

Cells were seeded for adherence in serum-free OptiMEM (OM) or RPMI for one hour, with appropriate serum-containing controls. The media and any unattached cells were then aspirated and replaced with their respective serum-containing mediums to observe the reversibility (re-suspension) of the transiently adhered cells. Images of wells at time points (t=0, 4, 8, 12, 24 hours) following media replacement were collected after aspiration and PBS wash. Cell counts are expressed as the relative normalized percentage of the maximum number of adhered cells at t=0.

3.2.6 Calcein-labeled Imaging and CD3-labeling of Uplifted Jurkat Cells

To determine if the adhered Jurkat cells maintained viability, cells were stained with CalceinAM, which is converted to green-fluorescent calcein after acetoxymethl ester hydrolysis in the presence of living intracellular esterases. Cells were allowed to adhere to the tissue culture polystyrene for 1hr, stained with 2uM Calcein in PBS (with Calcium and Mg) for 15minutes,

washed with PBS, and imaged at 40X. Brightfield and FITC images were acquired for OM and RPMI serum-free cell treatments, as well as unlabeled and necrotic controls.

Uplifted Jurkat cells were labeled with mouse anti-human CD3-PerCP(BD Biosciences catalog #347344) to determine if the transiently adhered cells still expressed CD3, a general T-cell marker that is not expressed on macrophages (Aoe et al. 1995). Jurkat cells in RPMI+FBS were used as the native control. Jurkat cells that had adhered in the OM and RPMI (serum-free counterparts) were also labeled with CD3-PerCP. Cell samples were centrifuged, aspirated, and incubated with the antibody (10uL) on ice for 30minutes. Cells were then washed in 1mL cold PBS, aspirated, and put in 250uL of 1% paraformadehyde for flow cytometry analysis.

Jurkat cell CD3-PerCP analyses were performed on a FACS Caliber flow cytometer (BD Biosciences, San Jose, CA) configured for single-color fluorescence measurements using 488-nm laser excitation. Scatter and fluorescence measurements were made on 30,000 cells per sample using Cellquest Pro software (BD Biosciences, San Jose, CA) and further analyzed using WinMDI 2.8 software (by Dr. J. Trotter, Scripps Institute, La Jolla, CA).

3.2.7 Evaluation of DNA Delivery to Adherent Jurkat Cells

Experiments were conducted to see if transiently-induced adhesion could improve delivery of DNA in the form of small oligonucleotides to Jurkat cells, which are known to be difficult to transfect (Zhao et al. 2006). Turbofect^{TM} was used as a cationic polymer transfection agent following the protocol instructions from Fermentas Life Sciences. Jurkat and HeLa cells (human epithelial carcinoma cells, American Type Culture Collection) were seeded in Permanox (Lab-Tek®) 8-well chambers. Suspension-state Jurkat cells were seeded in RPMI+FBS, while adherent-state Jurkat cells were allowed to attach to the tissue-treated substrate for 1hr in OM prior to DNA delivery. Adherent and suspension-state Jurkat cells were transfected with a 16-mer FAM-labeled oligonucleotide (5'-FAM-TAA AAC GAC GGC CAG T-3'; synthesized by

IDT). Polyplexes were prepared by mixing 1ug of oligonucleotide with 0.8ul of Turbofect stock reagent in 100ul OM for 15min at room temperature and then added drop-wise to culture wells in a 1:5 volumetric ratio (polyplex to cell media). Treated Jurkat and HeLa cells were incubated at 37°C in a CO_2 incubator for 24 hrs following polypex addition, and then fixed in 1% paraformaldehyde for flow cytometry analysis of transfection efficiency. Treated HeLa cells served as positive controls for oligonucleotide delivery, due to the ease of transfection of this common adherent cell line. Appropriate negative controls, including a control for delivery (DNA without transfection agent) and a transfection agent toxicity control (transfection agent only) were conducted in parallel.

3.2.8 Monitoring Adherent-state Jurkat Cells using Time-lapse Confocal Microscopy

Time-lapse microscopy has been used in recent studies to characterize the progression of apoptotic patways in real-time (Bouchier-Hayes et al. 2008). A Leica TCS SP2 spectral confocal & multiphoton system was used to monitor real-time responses of Jurkat cells in serum-free media. The system consists of a Leica DM IRE2 inverted microscope with a galvo-Z stage, equipped with Ar/Kr, He/Ne green, and He/Ne red lasers. Of the provided laser lines, excitation lasers at 488, 543, and 633nm were used in this experiment. Images were analyzed using Leica Confocal Software (LCS) Lite (Leica Microsystems Heidelberg GmbH).

3.2.9 Monitoring Adherent-state Jurkat Membrane Potential During E-field

Jurkat cells were labeled prior to time-lapse microscopy with $DiBAC_4(3)$ (bis-(1,3-dibarbituric acid)-trimethine oxanol; Invitrogen, Eugene, OR) as a quantitative measure of cellular depolarization and cell health. The lipophillic probe DiBAC exhibits changes in its transmembrane distribution and fluorescence in response to changes in the transmembrane potential (TMP) state of a cell. Labeling concentrations of DiBAC (250-500nM) were chosen

based on previous studies showing that DiBAC used as a voltage indicator should be used at low concentrations (<100nM) to avoid artifacts on transmembrane potential that are a result of the direct action of the molecule on potassium channels (Morimoto et al. 2007). Electric fields were applied to cell samples using a custom micro-electrode system for confocal imaging consisting of 76um diameter platinum wires affixed to a 1.5 coverglass substrate. Square wave voltages were applied (0 – 65Hz frequencies; 0 – 10V voltages; 0 – 17kV/m effective field strength) by output terminals on a DAQPad-6015 data acquisition system (National Instruments). Jurkat cells were transiently adhered to the imaging substrate by incubation in serum-free media as described above, and imaged for DiBAC fluorescence over 5 minutes following E-field exposure.

3.2.10 Real-time Monitoring of Apoptosis in Adherent-state Jurkat Cells

Apoptotic assays were performed in order to correlate cellular depolarization, as detected by single-cell DiBAC intensity and distribution patterns, to cell health at various time-points following induction of apoptosis. Studies of the patterns and kinetics of specific apoptotic events in Jurkat cells (including ionic homeostasis deregulation, phosphatidylserine exposure, blebbing, and nuclear condensation) were facilitated by inducing cells to adhere to substrates for continuous monitoring. Using time-lapse confocal microscopy, plasma membrane potential changes and phosphatidylserine externalization were monitored in real-time on a single-cell basis. Plasma membrane potential was determined by monitoring DiBAC (488/520nm); phosphatidylserine externalization was determined via AnnexinV-AlexaFluor 568 (578/603nm); and cell membrane integrity was determined via SYTOX Red (640/658nm). Fluorescent label profiles were analyzed within individual adherent cells for 60 minutes following induction of apoptosis. Necrotic cells were prepared by incubation in RPMI media with 4mM hydrogen peroxide for 18hr. For chemical apoptosis induction, cells were incubated in RPMI medium enriched with 10uM camptothecin (BD Biosciences).

3.3 Results and Discussion

3.3.1 Characterization of Adhesion

3.3.1.2 Effect of Serum on Jurkat Adhesion to Different Substrates

Brightfield images were collected and analyzed for cell counts to compare adhesion of Jurkat cells on different substrates. In RPMI and OM on tissue-treated substrate, supplementing the media with serum reduced the adhesive behavior seen without serum (see Fig. 3.1). Significant differences in effects due to serum are supported by $p<0.01$ between RPMI and RPMI+FBS and between OM and OM+FBS for the tissue-treated plate. Significant increase in adhered cells (932±116 cells/mm2) for the serum-deprived RPMI treatments and adhered cells (716±169cells/mm2) for the OM serum-deprived treatments are shown in Figure 3.1. For the fibronectin (FN)-coated-tissue-treated substrate, significant effects due to serum are supported between OM and OM+FBS ($p<0.01$) and RPMI and RPMI+FBS ($p<0.05$). As expected with the culture of Jurkat cells on a non-tissue treated surface, no significant attachment was observed in any media (Figure 3.1). A serum-dependent adhesion effect was observed on tissue-treated substrates, increased on FN-coated surfaces, and absent on non-treated plates. Thus, the role of serum was found to be critical to the rate of cell adhesion, similar to findings with adherent CHO cells by Bradley and colleagues (2001).

Additional studies were conducted to characterize this adhesion effect. Seeding cells in adhesion-promoting conditions and incubating on ice, a technique commonly used to prevent nonspecific protein-binding, did not prevent adhesion. Alternatively, wells coated with FBS and washed with Ca- and Mg-free PBS showed a marked decrease in adhesion. This suggests that the adhesion effect is related to the interaction between the cells, serum proteins, and charged surface. When the charge differentiation is not present, as in nontreated plates, or blocked, as in

cases where media is fortified with serum, Jurkat cells are less likely to experience nonspecific binding and adhere.

Figure 3.2 shows the kinetics of Jurkat cell adhesion over one hour in different media treatments on tissue-culture treated polystyrene. Serum-free OM cell treatment shows a rapid adhesion effect (100% cells adhered) occurring within 15 minutes, while the serum-free RPMI case resulted in only 24% of cells adhered (Fig. 3.2). An equivalent level of cell adhesion ("delayed" adhesion effect) occurs 45minutes later in the case of the serum-free RPMI treatment. The serum-containing cell treatments again show minimum level of adherence, even after 1 hour. Cells in OM were observed to have a higher rate of adhesion than cells in RPMI.

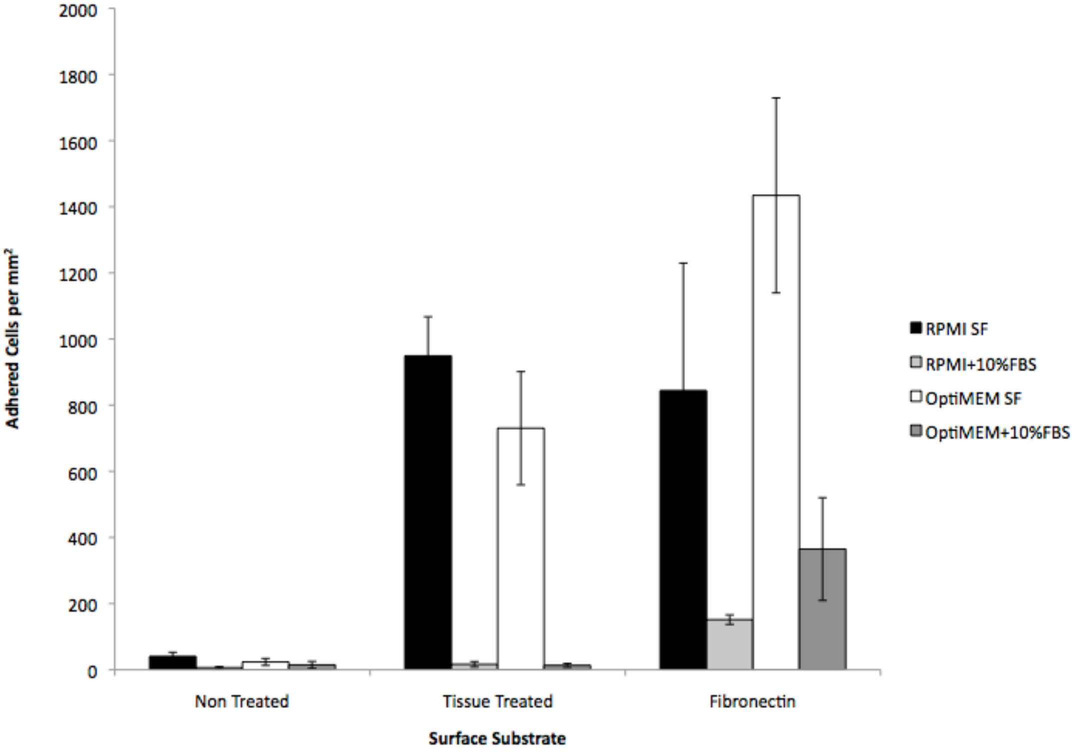

Figure 3.1 Attachment of Jurkat cells per mm^2 over three substrates in two media formulations under serum-fortified and serum-free conditions after one hour. Error bars denote standard error of the mean.

3.3.1.3 Validation of Adhered Cell Morphology and Viability

Calcein was used as a fluorescent viability indicator for the transiently attached Jurkat cells on tissue culture treated polystyrene. Brightfield imaging (Fig. 3.3A(I) and 3.3B(I)) shows healthy, round morphology of Jurkat cells in serum-free OM and RPMI treatments. Fig. 3.3A(II) and 3.3B(II) fluorescence images confirm that the attached Jurkat cells are viable with an equal distribution of calcein shown throughout the cell as seen in the brightfield-FITC overlays in Figs. 3.3A(III) and 3.3B(III). Fig. 3.3C shows the necrotic control (4mM H2O2) where the cells are much smaller in size (Fig. 3.3C(I)), indicative of dying cells. The dead cells also exhibit minimal calcein fluorescence as the calcein is observed leaking out of the cells (Fig. 3.3C(III)). This imaging data indicates that the serum-dependent cell adhesion does not disrupt gross cell behavior as the cells continue to maintain viability while adhered to the tissue-treated surface.

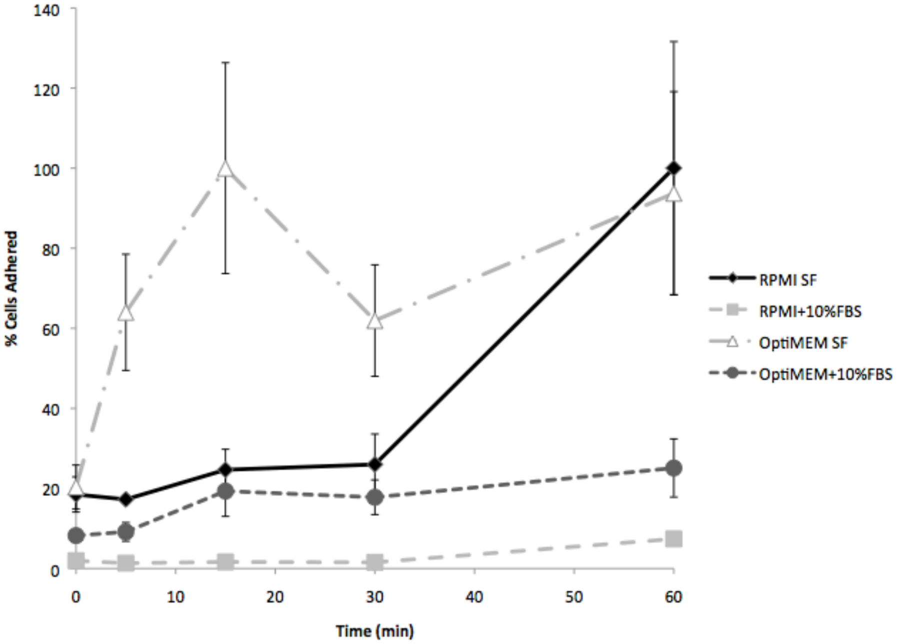

Figure 3.2 Time-course of Jurkat cell adhesion to tissue-treated polystyrene in two media compositions under serum-fortified and serum-free conditions. Cell counts are normalized based on the maximum number of cells attached for each media type. Error bars denote standard error of the mean.

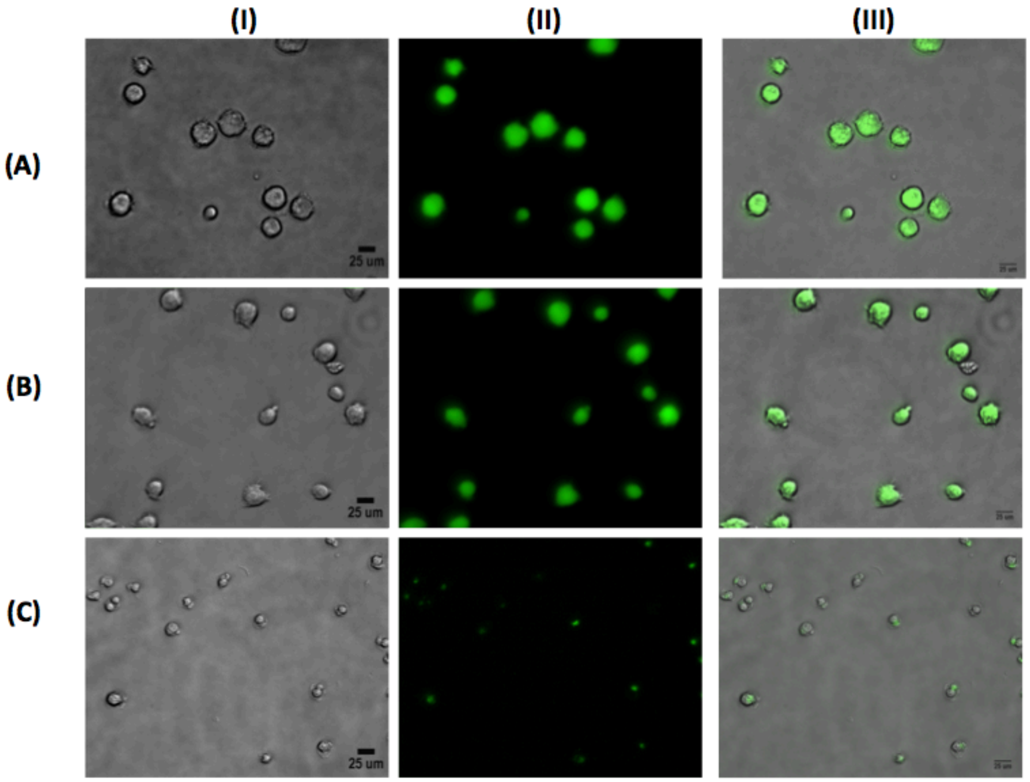

Figure 3.3 Representative BF and FITC images at 40X showing Jurkat cell viability after being attached to tissue culture polystyrene for 60min. (A) Jurkat cells attached via OM labeled with Calcein (I) BF, (II)FITC, (III) BF+FITC Overlay, (B) Jurkat cells attached via serum-free RPMI labeled with Calcein, (I) BF, (II)FITC, (III) BF+FITC Overlay (C) 4mM H_2O_2 Necrotic control, (I) BF, (II)FITC, (III) BF+FITC Overlay. Scale bar is 25um.

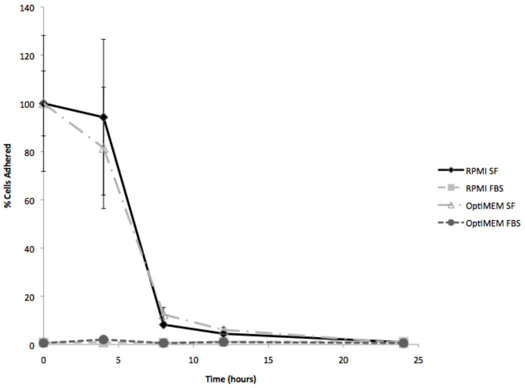

Figure 3.4 Reversal of transient adhesion of Jurkat cells in two media formulations under serum-fortified and serum-free conditions. Cells were seeded in tissue-treated polystyrene wells and observed over the course of 24 hours from initial attachment. Cell counts are normalized based on the maximum number of cells attached for each media type. Error bars denote standard error of the mean.

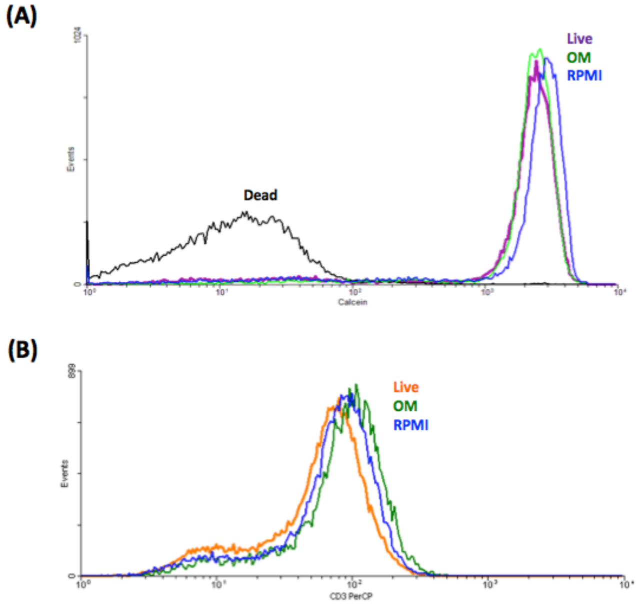

Figure 3.5 Representative histograms showing viability and preservation of T-cell marker of uplifted Jurkat cells (A) Calcein, FL1-Histogram Overlay of OM, RPMI, Live, and Dead Jurkat cells; (B) CD3-PerCP, FL3-Histogram Overlay of OM and RPMI-uplifted Jurkat cells, with RPMI+FBS suspension cells as a control. Jurkat cells were evaluated for viability and CD3 (T-cell marker) 24hrs following addition of serum-containing media.

3.3.2 Characterization of Cell Detachment, Viability, and Phenotype

Transiently adhered cells regained their suspension state when cells were returned to serum-fortified media. Figure 3.4 shows that ~90% of the cells in RPMI or OM have returned to suspension by 8 hours. Alternative methodologies were explored to return adhered cells to the suspension state. Jurkat cells were seeded in serum-free OM and allowed to adhere to the surface. Following aspiration of the OM and a PBS wash, trypsin was added to each well. After ten minutes of trypsinization, it was apparent that the adhesion had not been reversed (data not shown). Similarly, adherent cells left in serum-free media remained attached for at least 48h (data not shown,) but were not monitored beyond this time due to concerns over viability from lack of serum.

Flow cytometry data acquired provides evidence of viability and preservation of the CD3-T-cell marker in the uplifted Jurkat cells (Fig. 3.5). Live, OM-treated, and RPMI-treated Jurkat cells have similar calcein fluorescence, indicating that the uplifted cells are viable 24hrs following transient adhesion (Fig. 3.5A). These uplifted cells have also maintained the CD3 T-cell marker as shown in the histogram overlay (Fig. 3.5B). Jurkat cells induced to adhere to the tissue-treated polystyrene substrate in serum-free media are alive and still expressing CD3 T-cell marker; thus these cells had not differentiated.

3.3.3 Applications of Transiently-adhered Jurkat Cells

3.3.3.1 Increased Delivery of DNA Oligonucleotides to Adherent Jurkat Cells

Hematopoietic cells such as Jurkat cells are known to be difficult to transfect with non-viral vectors due to poor internalization of DNA complexes (Ogris et al. 2001). Promoting temporary adhesion of a suspension cell during the delivery process may be beneficial in transfecting cell types notably difficult to transfect. Flow cytometric quantification of labeled oligonucleotide fluorescence in cells provides evidence for higher transmembrane DNA delivery in adherent Jurkat cells versus those in suspension (Fig. 3.6). According to gated population and fluorescent marker analysis of the cytometry data, 1.7% of the suspension-state Jurkat cells were positive for FAM-oligo delivery, vs. 43.6% of the adherent-state Jurkat cells. These percentages may be compared to 79% FAM-oligo delivery in a control adherent cell line, HeLa, which are relatively easy to transfect and are often used in transfection studies. Jurkat cells are notoriously difficult to modify genetically using non-viral vector based gene transfer delivery systems (Zhao et al. 2006). There is some debate as to the source of the low transfectability of hematopoietic cells in their natural suspension state in culture. The low transfectability may be due to a lesser binding of DNA particles to the cell surface compared to that which occurs for adherent cell types (Papapetrou et al. 2005), thus calling for new techniques for inducing transient adhesion of

suspension cell lines. It should be noted that low transfection efficiency in hematopoietic cells may be due to poor transgene expression more so than inefficient delivery (Papapetrou et al. 2005), so additional studies are necessary to determine whether this transient adhesion approach can similarly improve genetic modification of Jurkat cells. However, the data found herein show enhanced DNA delivery can be achieved in a simple manner through serum-dependent adhesion techniques described previously.

3.3.3.2 Transmembrane Potential Changes Monitored in Single-cell in Real-time

Cell depolarization is an observed effect of electric-fields (E-fields) due to induced changes in ion gradients across the plasma membrane and membrane damage during relatively long and high strength fields. Plasma membrane potential and membrane permeability was analyzed herein via confocal fluorescent microscopy. Continuous monitoring of changes in DiBAC fluorescence in individual Jurkat cells was made feasible by their transient adhesion. Continuous monitoring of transmembrane potential in individual suspended Jurkat cells would be impossible due to their electrophoretic movement in E-fields strong enough to induce depolarization and membrane breakdown. Using techniques described for inducing adhesion, dye distribution changes in individual cells were visualized during (Fig. 3.7A) and 1 min after (Fig. 3.7B) electric-field. DiBAC fluorescence was studied over time up to 5 min following E-field, showing transient depolarization across the plasma membrane in moderate E-fields, with a maximum depolarization (DiBAC fluorescence intensity) 1 min after exposure (Fig. 3.7C). In order to track individual cells during time-lapse microscopy, it is sometimes necessary to immobilize suspension cells (Endlich et al. 2000). Methods devised here for inducing Jurkat cells to an adherent state in serum-free media for imaging purposes has permitted time-lapse

microscopy analysis of E-field cell manipulation without extensive or costly immobilization methods.

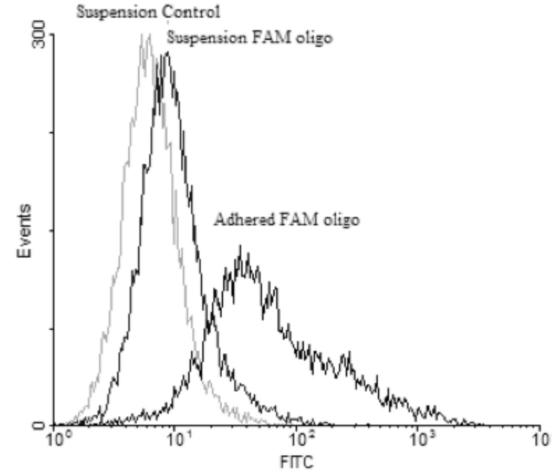

Figure 3.6 Histogram overlays showing increased FAM-labeled DNA oligonucleotide delivery to adhered Jurkat cells. Geometric mean values obtained via flow cytometry data analysis reveal greater delivery to adhered Jurkat cells (Suspension Control = 6.55; Suspension FAM oligo = 10.31; Adhered FAM oligo = 50). Gating analysis indicates that suspension state, 1.7% of cells contain FAM oligo, vs 43.6% of cells in the adhered state.

3.3.3.3 Evidence for Depolarization During Apoptosis

Single-cell monitoring of Jurkat cells in an aderent state was used to show that depolarization during apoptosis occurs prior to phosphatidylserine exposure on the outer plasma membrane leaflet (detected by AnnexinV-AlexaFluor 568) (Figure 3.8). DiBAC fluorescence intensity increased during intial stages of apoptosis, or within 30 minutes of camptothecin treatment (panel B), and was sustained after externalization of phosphatidylserine (panel C). Changes in DiBAC dye intracellular distribution were also observed upon breakdown of cell nucleus, or within 60min of camptothecin induction of apoptosis (panel D). Monitoring DiBAC fluorescence in a single cell over time provides evidence of marked depolarization of the plasma membrane within 60 minutes following induction of apoptosis via camptothecin. The distribution of DiBAC, a negatively charged dye molecule which is excluded from the intact nuclei of

healthy cells, was also shown to change markedly in late stages of apoptosis, due to permeabiliziation of the cell nucleus. Real-time monitoring of apoptosis on a single-cell basis has been accomplished previously (Bouchier-Hayes 2008,) albeit in adherent cell types. The serum-dependent adhesion technique developed herein has enabled the real-time monitoring of changes in AnnexinV and DiBAC labeling following apoptosis induction of suspension cells, without affecting normal cell cycle progression. This technique may prove useful for studies requiring continuous observation of individual suspension cells.

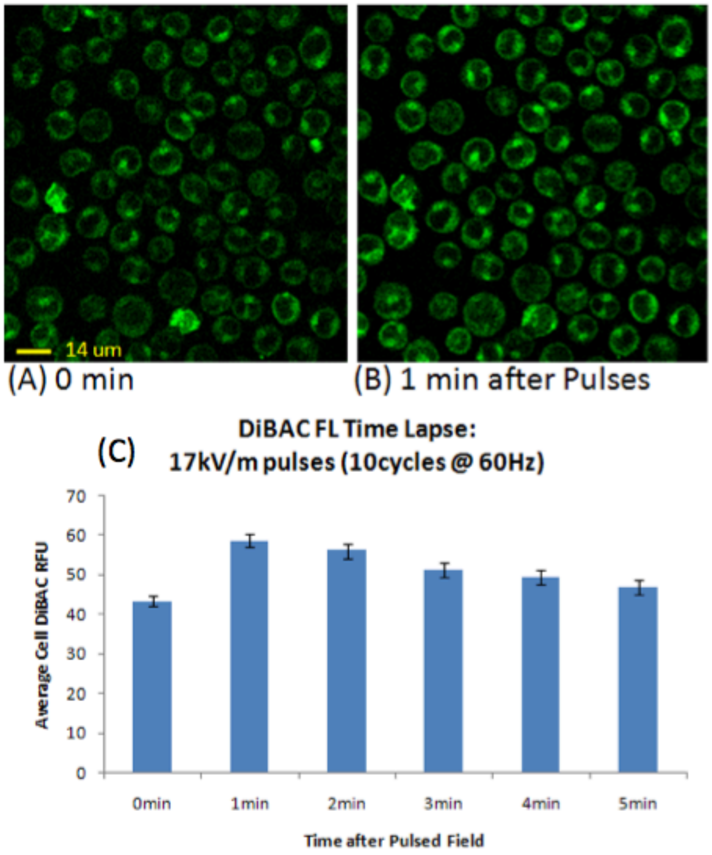

Figure 3.7 DiBAC fluorescence time-lapse microscopy showing transient depolarization of adherent Jurkat cells in the presence of e-field: (A) DiBAC image of attached Jurkat cells (0min), (B) DiBAC image of attached Jurkat cells (1min after e-field pulse application), and (C) Average whole-cell DiBAC intensity over time after electric-field application.

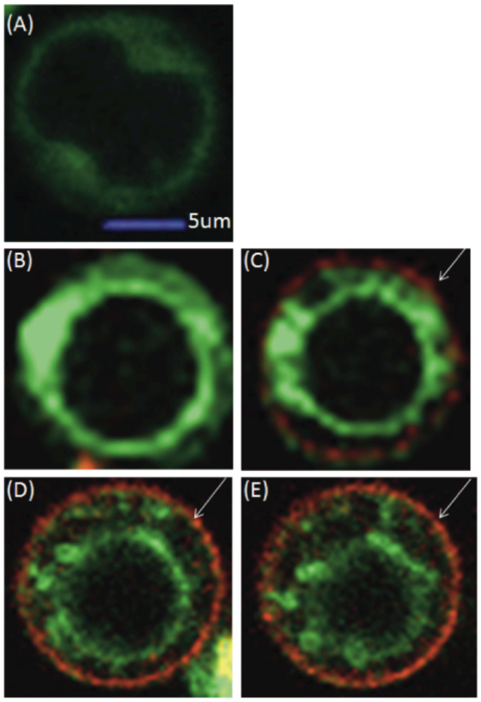

Figure 3.8 Time-lapse microscopy of an adhered Jurkat cell in serum-free media monitoring apoptosis events in real-time: (A) Live cell stained with DiBAC, (B) Early apoptotic cell (30min post-camptothecin treatment) showing depolarization of plasma membrane (increase in DiBAC dye concentration), (C) Apoptotic cell (30min post-camptothecin treatment) showing externalization of phosphatidylserine (binding by AnnexinV-AlexaFluor 568), (D) Apoptotic cell (45min post-camptothecin treatment) showing externalization of phosphatidylserine, (E) Apoptotic cell (60min post-camptothecin treatment) showing DiBAC distribution changes (breakdown of cell nucleus). Arrows indicate Annexin V-568 localized fluorescence.

3.4 Conclusion

The purpose of this study was to characterize the adhesion effect of serum on Jurkat cells, to resuspend these transiently adhered, viable cells, and to investigate several applications of this observed adhesive effect. There is a distinct relationship between the presence of serum in media and transient adhesion of Jurkat cells on tissue-treated polystyrene surfaces. Adhered Jurkat cells were resuspended and the cells were evaluated for viability and preservation of a T-cell marker (CD3) via fluorescent microscopy and flow cytometric analysis. Enhanced cellular delivery of DNA oligonucleotides was shown for the transiently adhered state. Under proper conditions

(serum and substrate), a single suspension cell was studied via fluorescence microscopy, which would otherwise prove difficult. This technique permitted DiBAC fluorescence time-lapse imaging of adhered Jurkat cells exhibiting transient depolarization in an electric-field, and we also show the ability to monitor progression of apoptosis in real-time by time-lapse microscopy of transiently adhered Jurkat cells in serum-free media. Further study is necessary to characterize integrin-mediated signal transduction pathways that may be altered by this transient adhesion that could change longer-term phenotypic profiles of these cells.

3.5 References

Abhyankar VV, Beebe DJ. 2007. Spatiotemporal micropatterning of cells on arbitrary substrates. Anal Chem 79(11):4066-73.

Aoe T, Okamoto Y, Saito T. 1995. Activated Macrophages Induce Structural Abnormalities of the T-Cell Receptor-Cd3 Complex. Journal of Experimental Medicine 181(5):1881-1886.

Bergman AJ, Zygourakis K. 1999. Migration of lymphocytes on fibronectin-coated surfaces: temporal evolution of migratory parameters. Biomaterials 20(23-24):2235-44.

Biran I, Walt DR. 2002. Optical Imaging fiber-based single live cell arrays: A high-density cell assay platform. Analytical Chemistry 74(13):3046-3054.

Bouchier-Hayes L, Munoz-Pinedo C, Connell S, Green DR. 2008. Measuring apoptosis at the single cell level. Methods 44(3):222-228.

Bratten CDT, Cobbold PH, Cooper JM. 1997. Micromachining sensors for electrochemical measurement in subnanoliter volumes. Analytical Chemistry 69(2):253-258.

Deng J, Schoenbach K, Buescher E, Hair P, Fox P, Beebe S. 2003. The effects of intense submicrosecond electrical pulses on cells. Biophysical Journal 84(4):2709-2714.

Deutsch M, Deutsch A, Shirihai O, Hurevich I, Afrimzon E, Shafran Y, Zurgil N. 2006. A novel miniature cell retainer for correlative high-content analysis of individual untethered non-adherent cells. Lab on a Chip 6(8):995-1000.

Deutsch M, Weinreb A. 1994. Apparatus for High-Precision Repetitive Sequential Optical Measurement of Living Cells. Cytometry 16(3):214-226.

Dimilla PA, Quinn JA, Albelda SM, Lauffenburger DA. 1992. Measurement of Individual Cell-Migration Parameters for Human Tissue-Cells. Aiche Journal 38(7):1092-1104.

Endlich B, Radford IR, Forrester HB, Dewey WC. 2000. Computerized video time-lapse microscopy studies of ionizing radiation-induced rapid-interphase and mitosis-related apoptosis in lymphoid cells. Radiation Research 153(1):36-48.

Frey W, White J, Price R, Blackmore P, Joshi R, Nuccitelli R, Beebe S, Schoenbach K, Kolb J. 2006. Plasma membrane voltage changes during nanosecond pulsed electric field exposure. Biophysical Journal 90(10):3608-3615.

Glassy M, Tharakan J, Chau P. 1988. Serum-free media in hybridoma culture and monoclonal-antibody production. Biotechnology and Bioengineering 32(8):1015-1028.

Inoue I, Wakamoto Y, Moriguchi H, Okano K, Yasuda K. 2001. On-chip culture system for observation of isolated individual cells. Lab on a Chip 1(1):50-55.

Keller H, Yunxu C, Marit G, Pla M, Reiffers J, Theze J, Froussard P. 1999. Transgene expression, but not gene delivery, is improved by adhesion-assisted lipofection of hematopoietic cells. Gene Therapy 6(5):931-938.

Khine M, Lau A, Ionescu-Zanetti C, Seo J, Lee LP. 2005. A single cell electroporation chip. Lab on a Chip 5(1):38-43.

Ko S, Johnson V, Chow S. 2000. Functional characterization of Jurkat T cells rescued from CD95/Fas-induced apoptosis through the inhibition of caspases. Biochemical and Biophysical Research Communications 270(3):1009-1015.

Lawson MA, Maxfield FR. 1995. Ca2+ and Calcineurin-Dependent Recycling of an Integrin to the Front of Migrating Neutrophils. Nature 377(6544):75-79.

Li X, Yang Y, Ashwell JD. 2002. TNF-RII and c-IAP1 mediate ubiquitination and degradation of TRAF2. Nature 416.

LI-COR_Biosciences. 2006. Technical Note: FAQs for Suspension Cells for ICW Protocols. 1. Handling Suspension Cells. Lincoln, NE: LI-COR Biosciences. p 1-4.

Lloyd AR, Oppenheim JJ, Kelvin DJ, Taub DD. 1996. Chemokines regulate T cell adherence to recombinant adhesion molecules and extracellular matrix proteins. Journal of Immunology 156(3):932-938.

Malek TR, Fleming TJ. 1994. Regulation of Il-2 Production by Ly-6a/E Independent of Its Glycosylphosphatidylinositol (Gpi)-Anchor. Journal of Cellular Biochemistry:300-300.

Manca F. 1991. Interference of monoclonal antibodies with proteolysis of antigens in cellular and in acellular systems. Ann. Ist. Super. Sanita 27:15-19.

Manca F, Fenoglio D, Pira GL, Kunkl A, Celada F. 1991. Effect of Antigen-Antibody Ratio on Macrophage Uptake, Processing, and Presentation to T-Cells of Antigen Complexed with Polyclonal Antibodies. Journal of Experimental Medicine 173(1):37-48.

Morimoto T, Sakamoto K, Sade H, Ohya S, Muraki K, Imaizumi Y. 2007. Voltage-sensitive oxonol dyes are novel large-conductance Ca2+-activated K+ channel activators selective for beta 1 and beta 4 but not for beta 2 Subunits. Molecular Pharmacology 71(4):1075-1088.

Neugebauer KM, Reichardt LF. 1991. Cell-Surface Regulation of Beta-1-Integrin Activity on Developing Retinal Neurons. Nature 350(6313):68-71.

Nyakern M, Cappellini A, Mantovani I, Martelli A. 2006. Synergistic induction of apoptosis in human leukemia T cells by the Akt inhibitor perifosine and etoposide through activation of intrinsic and Fas-mediated extrinsic cell death pathways. Molecular Cancer Therapeutics 5(6):1559-1570.

Ogris M, Steinlein P, Carotta S, Brunner S, Wagner E. 2001. DNA/polyethylenimine transfection particles: Influence of ligands, polymer size, and PEGylation on international and gene expression. Aaps Pharmsci 3(3):art. no.-21.

Papapetrou EP, Zoumbos NC, Athanassiadou A. 2005. Genetic modification of hematopoietic stem cells with nonviral systems: past progress and future prospects. Gene Therapy 12:S118-S130.

Rouhi AM. 1999. Contemporary biomaterials. Chemical & Engineering News 77(3):51-+.

Saim AB, Cao Y, Weng Y, Chang CN, Vacanti MA, Vacanti CA, Eavey RD. 2000. Engineering autogenous cartilage in the shape of a helix using an injectable hydrogel scaffold. Laryngoscope 110(10 Pt 1):1694-7.

Shapiro JA, Hsu C. 1989. Escherichia-Coli K-12 Cell-Cell Interactions Seen by Time-Lapse Video. Journal of Bacteriology 171(11):5963-5974.

Sun Y, Liu JL, Qian F, Xu Q. 2006. Nitric oxide inhibits T cell adhesion and migration by down-regulation of beta 1-integrin expression in immunologically liver-injured mice. International Immunopharmacology 6(4):616-626.

Tan J, Shen H, Saltzman WM. 2001. Micron-scale positioning of features influences the rate of polymorphonuclear leukocyte migration. Biophysical Journal 81(5):2569-2579.

Teare DOH, Emmison N, Ton-That C, Bradley RH. 2001. Effects of serum on the kinetics of CHO attachment to ultraviolet-ozone modified polystyrene surfaces. Journal of Colloid and Interface Science 234(1):84-89.

Thirumala S, Forman, J.M., Monroe, W.T., Devireddy, R.V. 2007. Freezing and post-thaw apoptotic behaviour of cells in the presence palmitoyl nanogold particles. Nanotechnology 18(195104).

Vernier P, Sun Y, Marcu L, Craft C, Gundersen M. 2004. Nanosecond pulsed electric fields perturb membrane phospholipids in T lymphoblasts. FEBS Letters 572(1-3):103-108.

Vernier P, Sun Y, Marcu L, Salemi S, Craft C, Gundersen M. 2003. Calcium bursts induced by nanosecond electric pulses. Biochemical and Biophysical Research Communications 310(2):286-295.

Wennemuth G, Eisoldt S, Bode HP, Renneberg H, Schiemann PJ, Aumuller G. 1998. Measurement of calcium influx in surface-fixed single sperm cells: efficiency of different immobilization methods. Andrologia 30(3):141-146.

Zell T, Kivens WJ, Kellermann SA, Shimizu Y. 1999. Regulation of integrin function by T cell activation - Points of convergence and divergence. Immunologic Research 20(2):127-145.

Zhao YB, Zheng ZL, Cohen CJ, Gattinoni L, Palmer DC, Restifo NP, Rosenberg SA, Morgan RA. 2006. High-efficiency transfection of primary human and mouse T lymphocytes using RNA electroporation. Molecular Therapy 13(1):151-159.

Zhu C, Joyce N. 2004. Proliferative response of corneal endothelial cells from young and older donors. Investigative Ophthallmology & Visual Science 45(6):1743-1751.

CHAPTER 4. LABEL-FREE, SINGLE-CELL VIABILITY DETECTION USING ELECTRICAL IMPEDANCE IN A PMMA MICROCHIP DEVICE

4.1 Introduction

4.1.1 Background on Cell Viability

Biological Micro-Electro-Mechanical Systems (BioMEMS) offer many advantages over conventional macroscale approaches to biomedical diagnostics, such as reduced reagents and power consumption, shorter reaction time, portability, low-cost, versatility, and potential for parallel, integrated operations (Bao et al. 2008). BioMEMS have the potential to change the ways in which many current cell-based biomedical studies are performed. The ability to design a microchip device to detect cell viability at the single-cell level in real-time has much potential for pharmacological drug screening or point-of-care diagnostics. In this chapter, we demonstrate a BioMEMS device that can differentiate between live and dead cells.

In many biomedical and biotechnology applications, it is important to distinguish between live and dead cells. There are two distinct forms of cell death, necrosis and apoptosis. Necrosis is an uncontrollable pathological form of cell death characterized by cell swelling, plasma membrane rupture, and inflammation. It is a result of chemical or physical damage to the cell (Kerr et al. 1972). Apoptosis is triggered by milder environmentally damaging stimuli, such as ultraviolet radiation or lack of growth factors. Apoptosis is a complex, tightly regulated programmed cell death (PCD), which is caused by internal or external cellular events. Apoptotic processes are important for maintaining tissue homeostasis, natural defense mechanisms, and the natural aging process (Vaux and Strasser 1996). Inappropriate regulation of apoptosis results in disease, such as cancer, developmental defects, and neurodegenerative diseases. Loss of cell membrane integrity is a very late event during apoptosis and is similar to the compromised cell membrane characteristic of necrosis. Dissimilar morphological and biochemical features are

used to differentiate between necrosis and apoptosis. For therapeutic intervention, a clear understanding and ability to detect apoptotic and necrotic events is important.

There are currently over 300 different cell viability and apoptosis detection kits on the market, yet all of these methods still have limitations for acquiring quantitative data of single cells (Valero et al. 2005; Wolbers et al. 2005). Early apoptosis and viability assays relied upon morphologic changes detected by light microscopy, electron microscopy, or flow cytometry using nuclear staining dyes (Koopman et al. 1994). Quantifying apoptosis by microscopy was inexact, and the nonvital dyes would only stain late apoptotic cells once the membrane was damaged. Stained cells can be viewed for qualitative results under a fluorescence microscope, using appropriate filters, and quantified by flow cytometry.

Notterman and colleagues mention the application of pharmacological effects on cell cycle and cell death which could be improved upon through real-time monitoring (Sohn et al. 2000) while Wang's group emphasizes the importance of a medical diagnostic tool for early detection and monitoring of cancer treatment efficacy, such as detection and quantification of apoptotic cells in a patient's blood before and during cancer treatment (Wang et al. 2002). Additionally, this device could be used for the analysis of human blood, such as when differential white blood count is used as an early disease indicator or for detecting and isolating fetal cells from the maternal circulation to test for prenatal genetic analysis as suggested by Holmes (Holmes et al. 2006). The miniaturized detection of apoptosis on a chip could also serve as a novel tool for better understanding cellular signaling pathways and disease. The need for early detection is a goal for clinical diagnoses and future point-of-care applications (Ahn et al. 2004). With the progression of micro-/nano-technology today, the ability to study viability in single cells in real-time without the use of fluorescent labels is becoming a reality.

4.1.2 Recent Viability Studies Using Microfluidic Platforms

There are several reports of studying cell behavior with optical-based BioMEMS devices, which aim to decrease analysis time, increase sensitivity, consume less reagents and cells, and allow for high-throughput screening. A microfluidic "cell-trap" device that manipulates cells by electroosmotic flow (EOF) was one of the first devices used to study apoptosis optically at the single-cell level (Valero et al. 2005). Most of the optical devices focus on fluorescent monitoring of a particular cellular or molecular target that forms the basis of the assay, such as mitochondrial membrane potential (Lu et al. 2004), DNA fragmentation (Kleparnik and Horky 2003), caspase release (Tabuchi and Baba 2004), intracellular calcium (Wheeler et al. 2003; Yang et al. 2002), or calcein/PI staining (Komen et al. 2008). One of the few non-fluorescent optical approaches reported is the use of thermal lens microscopy to monitor cytochrome c release (Tamaki et al. 2002).

There have been many recent developments to utilize electric analysis for detection and characterization of single cells in microfluidics (reviewed in Bao et al. 2008; Chao and Ros 2008; Spegel et al. 2008). Electroanalytical methods have various advantages over optical-based methods, such as minimal cell manipulation, reduced cell preparation/cost of reagents, potential for automation, amenability for miniaturization, ease for real-time monitoring, and sensitivity of detection. The applications for an electric-based MEMS device include disease diagnosis, drug screening, environmental monitoring, and a tool for better studying molecular cell biology and neuroscience (Bao et al. 2008). Electrical-based methods provide a non-invasive means of detecting and quantifying cell properties, such as cell size, membrane capacitance, and cytoplasm conductivity as a function of frequency (Cheung et al. 2005). Relevant dielectric properties of cells are described in terms of their application for cell-based detection. Electrical methods are easily integrated in microfluidic systems and show much promise due to their

relatively simpler and less expensive peripheral equipment (Yi et al. 2006a). Incorporation of this instrumentation at the microscale has been reported to cost \$4,000-\$5,000 for the electrical impedance-based method, and are the lowest compared to optical and mass spectrometric (MS) equipment, ranging from \$50,000 to 250,000 (Yi et al. 2006b).

4.1.3 Dielectric Properties of Cells

Dielectrophoresis (DEP) is the movement of polarizable particles that are placed in a non-uniform electrical field and is based on the difference in permittivities of the particles and surrounding media (Jones 1995; Pohl 1951; Wang et al. 2002). A cell has a dielectric constant that is significantly different than the surrounding buffer. Cellular DEP responses are studied as a function of applied electric field, allowing for single-cell discrimination of cell membrane capacitance and conductivity. The eukaryotic biological cell is typically modeled as a spherical particle with a conductive cytoplasm and capacitive cell membrane. The induced charge is not uniformly distributed across the cell; rather it is an induced dipole and is dependent on the relative polarizability of the particle with respect to the surrounding media. The DEP crossover frequency (f_{xo}) is the frequency where the DEP force switches from positive DEP (pDEP) to negative DEP (nDEP) and vice versa. By plotting f_{xo} x cell radius vs. conductivity of medium and determining the linear slope (provided medium conductivity > 0.01 mS/m), DEP crossover frequency and measured cell radius in a known conductivity medium can be used to approximate cell membrane capacitance and conductance values where $C_{MEM} = \frac{\sqrt{2}}{2\pi \text{slope}}$ (Wang et al. 2002). In summary, there are two major cell components that affect the overall impedance of a cell: membrane capacitance (related to membrane morphology- thickness and folds) and cytoplasm conductivity (related to intracellular ionic strength, pH, cell size, ionic materials). The relationship between the measured properties, such as cell membrane capacitance values, and

cell viability is important for the motivation of the proposed impedance-based differentiation of live and dead cells.

4.1.4 Electrical Impedance Spectroscopy (EIS)

Electrical impedance spectroscopy (EIS), also referred to as dielectric spectroscopy, is a noninvasive method for characterizing the dielectric properties of a sample (biological particle). An alternating current (AC) voltage is applied and the complex impedance (Z) of the sample between two electrodes is measured as the ratio of V to I, where I is the complex current and V is the AC voltage. Electrical impedance is usually represented as a phasor (magnitude and phase): $|Z| = \left|\frac{V_o}{I_o}\right|$ and $\angle Z = \theta$, where Vo is the AC voltage, Io is the resulting current, and θ is the phase shift. In Cartesian coordinates, impedance is a complex number, Z = R +jX, where j=$\sqrt{-1}$ and the real and imaginary parts of Z describe electrical resistance (R) and electrical reactance X_C (purely capacitive, no appreciable inductive component), and can be represented by appropriate electrical circuit elements in series (Cho et al. 2006). Thus, the total impedance is expressed as |Z| = $\sqrt{R^2 + X_C{}^2}$ and $\angle Z = \tan^{-1}\left(\frac{X_c}{R}\right)$.

Impedance characterization of cells is typically conducted by applying an AC potential between a pair of electrodes, which results in an electric field between the electrodes. When a cell crosses this field, it temporarily modifies the field, as well as the current, to enable detection of membrane and cytoplasm properties of the sample located between the electrodes. Impedance measurements have been determined for various cell types: blood cells (Gimsa et al. 1996), bacteria (Gomez-Sjoberg et al. 2005); on-chip blood differentiation (Cheung et al. 2005), L929 murine fibroblasts (Cho et al. 2008), human mesenchymal stem cells (Cho et al. 2009a; Cho and

Thielecke 2008) infected red blood cells (Kuttel et al. 2007), cardiomyocytes (Krinke et al. 2009), and yeast cells (Patel et al. 2008).

Impedance measurements over a wide range of frequencies can reveal important cell biophysical properties, such as cell morphology, physiological state, and viability/identity, on the basis of differences in cell size, membrane capacitance and cytoplasm conductivity (Vykoukal et al. 2009). When a biological cell experiences an AC field, it is polarized due to a charge accumulation at the phase boundaries (Kuttel et al. 2007). The measured impedance depends on the amount of polarization of the cell, the cell volume, and the applied frequency. At low frequencies (100 kHz to 1 MHz), the cell appears to be non-conducting and the capacitive cell membrane forms a barrier to the current and thus the measured impedance gives information on cell size or cell volume (Gawad et al. 2001; Schade-Kampmann et al. 2008). For intermediate frequencies (2-5 MHz), impedance measurements reveal electrical properties of the cell membrane, which becomes permeable for an electric field (Gawad et al. 2001; Pethig and Kell 1987). At higher frequencies (greater than 5 MHz), membrane polarization is lower (forming less barrier to the current) and more current flows through the cell, thus the impedance measurements convey more about the cell interior and cell structure properties (Cheung et al. 2005).

Dielectric properties of eukaryotic cells and changes involved in cell viability have brought much attention to the dielectric differences that have been reported for live, apoptotic, and necrotic cells. This non-optical tool could have applications in oncology, haematology, or toxicology. Impedance-based methods on microfluidic platforms are currently being widely used to study cells. However, there is still no published account of impedance-based, label-free, flow-through cell viability detection of individual cells on a chip.

4.1.5 Objectives

Impedance on-chip cell experiments described here aim to differentiate live and dead cells to determine if impedance magnitude and phase measurements are sensitive enough to discern cell viability, thus providing a label-free method for assaying cell viability. Based on the DEP-related dielectric changes described for cells undergoing apoptosis and necrosis described earlier (Labeed et al. 2006; Pethig and Markx 1997; Wang et al. 2002), we believe these membrane and dielectric cell differences will permit such discrimination. The purpose of this study is to determine if electrical impedance measurements alone can be used to evaluate cell viability (live vs. necrotic cell), allowing for label-free, real-time quantitative flow-through analysis on the single-cell level without the use of an expensive fluorescent microscope or flow cytometer.

4.2 Materials and Methods

4.2.1 Microfluidic Chip Design and Fabrication of Polymer-based Device

Microfabrication of the microfluidic chip involves a series of steps (Fig. 4.1A), beginning with hot-embossing a 76 um Pt wire into 3.2 mm thick PMMA substrate wafer (GoodFellow Corp (PA)). Hot-embossing is carried out at 160 °C for 4min. Prior to embossing, the Pt wire is threaded through holes drilled in PMMA with the use of a custom AutoCAD® (Autodesk, Inc.) design template. PMMA was selected as the substrate due to its good machinability and ability to form structures, minimal nonspecific binding of cells to the surface, and clear optical properties for visualizing the cells through the microchannel (Adams et al. 2008). Micromachining is used to clear the 50 um-wide channel and cut the 76 μm diameter Pt wire (resistivity of 10.6 μΩ-cm (20°C), Sigma-Aldrich) to form the integrated sidewall Pt microelectrodes. A high precision micromilling machine (KERN MMP 2522, KERN Micro- and Feinwerktechnik GmbH & Co.KG; Germany) with a 50 um drill bit was used to form the sidewall electrode pair. Fig. 4.2A

shows the overall chip layout of the single 50 um-wide microchannel (Fig. 4.2B) and the integrated cell sensing electrodes (Fig. 4.2C).

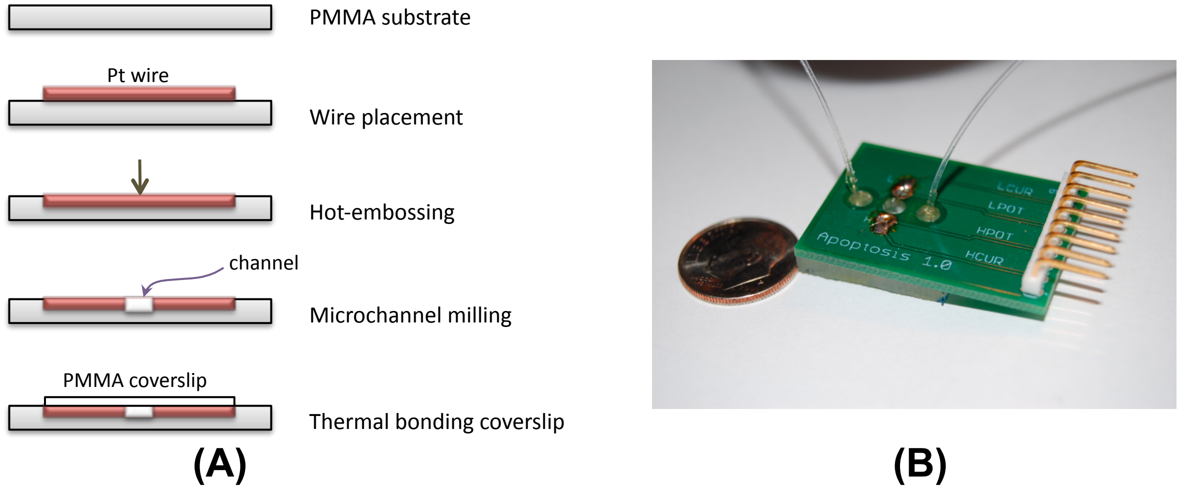

Figure 4.1 (A) Illustration showing the microfabrication steps in fabricating a PMMA chip with milled-through Pt wire to create integrated sidewall electrodes, (B) Prototype microchip for detection of cell viability. Printed circuit board was designed for fixturing to the impedance analyzer.

After thorough cleaning of the PMMA channel, thermal fusion bonding of the coverslip is performed. During thermoplastic fusion bonding, the PMMA microchip and coverslip (0.125 mm thick) pair is dried with N_2 gas, aligned and clamped together between two glass plates (Adams et al. 2008), and placed in 50 °C oven for 10 min, followed by 105 °C for 40 min, and 2 hrs at 50 °C before unclamping the coverslip-sealed PMMA chip. FITC leak tests are performed to ensure that the chip has a complete seal and the buffer/cells will successfully flow through the microchannel. The chip fabrication is completed (Fig. 4.1B) when the microfluidic fittings and tubing are secured at the inlet/outlet (for infusing cell samples). Teflon FEP Tubing (1/32" or 793.75um OD) (Upchurch Scientific, Oak Harbor, WA) was epoxied at the inlet and outlet of the PMMA chip device and fitted to 25G leur and 1mL leur-lock plastic syringe (Becton Dickinson, Franklin Lanes, NJ, USA). The Pt microelectrode leads are conductive epoxied (Cotronics Corp.,

Brooklyn, NY) to a custom printed circuit board PCB (Advanced Circuits, Aurora, CO) that was used to connect with the BNC test leads of the impedance analyzer for cell and buffer experiments.

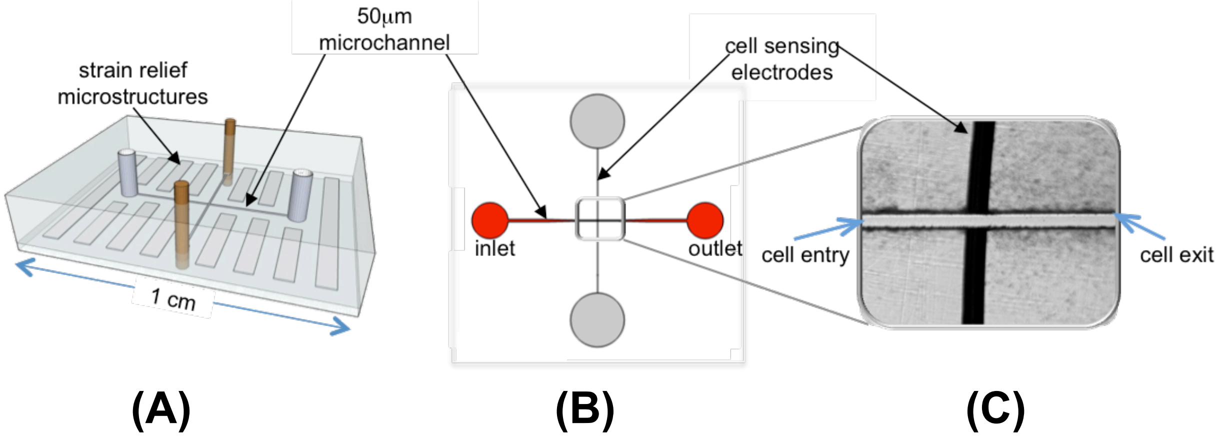

Figure 4.2 Schematics showing the following: (A) 3D diagram of the cell viability PMMA chip, (B) simplified design of the single channel layout, (C) integrated cell sensing electrodes consisting of cylindrical Pt electrodes that were 76um in diameter with a 50um spacing between the pair of electrodes.

4.2.2 Instrumentation

An overview of the important apparatus equipment used for this BioMEMS study is shown in Fig. 4.3. NE-500 syringe pumps (New Era Pump Systems, Inc; Wantagh, NY) were controlled via MS-DOS to provide pressure-driven flow. The syringe pump was programmed to generate a flow rate of 1 uL/hr to maintain optimal flow rate of single cells past the detection electrodes. The linear velocity of 73 um/sec was calculated from the cross-sectional area of the microchannel and the programmed volumetric flow rate (Q of 1uL/hr with Area of 50 umx76 um). Tracking cells via optical microscopy over the known distance of the 76 um-wide electrodes was performed to validate the linear cell velocity.

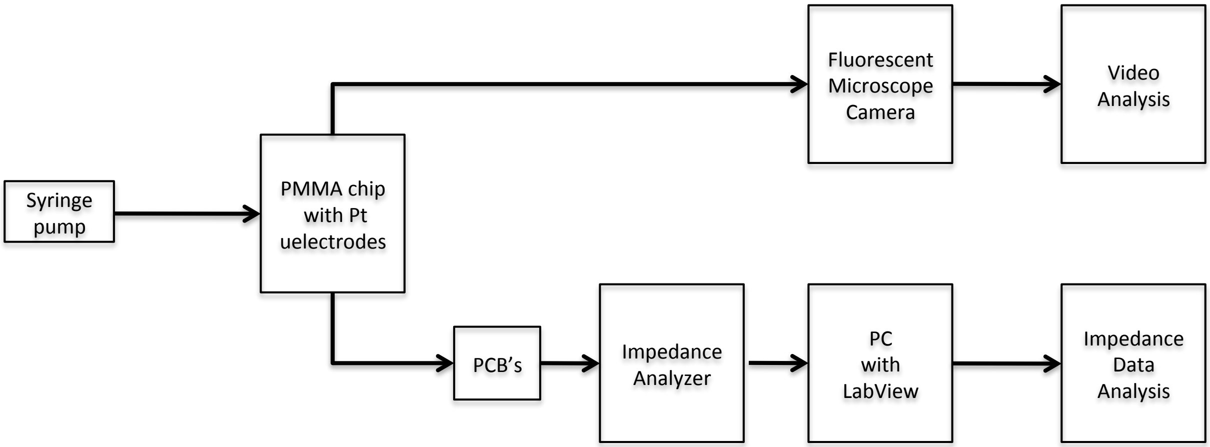

Figure 4.3 Overview of the instrumentation involved in operating the cell viability impedance-based microchip device, including the microscope required for optical validation.

Brightfield and fluorescence video microscopy were used to confirm viability and correlation to the acquired impedance signals. Images were acquired with an inverted Eclipse TS100 Nikon fluorescence microscope using 10× and 20× objective lenses and a CoolSnapFX camera (Photometrics, Tucson, AZ). Image processing was performed on a Windows computer using MetaVue software (Universal Imaging Corporation, West Chester, PA). Time-lapse images were acquired to determine cell velocimetry (ranging from 25-75 um/sec). Cells were monitored in the chip using either fluorescence or brightfield microscopy. FITC stream acquisition was acquired at 3 frames per second (fps) to capture calcein fluorescence with an exposure time of 250 ms.

Electrical signals were obtained using an Agilent E4980A high precision LCR meter with 1-m test cable leads (Agilent Technologies, Irvine, CA) at an operating voltage of and over a frequency range of 20 kHz to 2 MHz. The impedance analyzer was self-calibrated using short- and open- calibrations before the buffers or cells were analyzed. Data acquisition was performed using a National Instruments VI with custom programming (National Instruments, Austin, TX). Measurements were acquired for in-flow, single cells at a single frequency over time. Cells

moved at a velocity of 25-75 um/s. From the recorded data, the magnitude and phase signals were compared with the acquired video data.

4.2.3 Cell Culture

Jurkat T lymphocyte cells (E6.1, ATCC) were maintained in 25 cm^2 flasks (BD Falcon, Franklin Lakes, NJ) with 5 mL of classical RPMI-1640 (RPMI) supplemented with 10% fetal bovine serum (FBS) and were incubated at 37°C in a humidified atmosphere containing 5% CO_2. For the dead experimental control, Jurkat cells were incubated in a 12-well plate with 4mM H2O2 in RPMI for 18 hr prior to analysis. Impedance experiments were carried out in a low conductivity buffer at physiological pH, ~300mOsm. All samples used in the experiments were concentrated by centrifugation at 400 x g's for 5 min and resuspended in appropriate low-conductivity cell buffer to obtain a concentration of $1x10^5$ cells/mL for impedance measurements.

To determine if Jurkat cells maintained viability in the various low-conductivity cell buffers, a time-course experiment was conducted in which cells were incubated in each buffer for 30min, 4hr, and 24hr. Calcein-AM (Invitrogen) was used to assess viability. CalceinAM is converted to green-fluorescent calcein after acetoxymethl ester hydrolysis in the presence of living intracellular esterases. Cells were labelled with 2uM Calcein in PBS (with Calcium and Mg) for 15minutes, washed with PBS, and resuspended in 300ul PBS for flow cytometry. Flow cytometry analyses were performed on a FACS Caliber flow cytometer (BD Biosciences, San Jose, CA) configured for single-color fluorescence measurements using 488-nm laser excitation. Scatter and fluorescence measurements were made on 30,000 cells per sample using Cellquest Pro software (BD Biosciences, San Jose, CA) and gated based on live cell control (Region1).

4.2.4 Electron Microscopy

Jurkat cell suspension (~1ml) was extracted into a syringe containing an equal volume of 4% glutaraldehyde in 0.1M sodium cacodylate buffer, pH7.2. The fluid was diluted with 6 ml 2% glutaraldehyde in 0.1M buffer. Draw the mixture to a 10ml syringe with a Swinney filter holder fitted with a 13 mm diameter 5um pore polycarbonate filter. Filtered and fixed the cell suspension for 4 hours. Then was washed 4X in 0.1M cacodylate buffer containing 0.02M glycine during, post-fixed in 2% osmium tetroxide for 1 hr, rinsed in water, *en bloc* stained in 0.5% uranyl acetate in the dark for 1 hr, rinsed in water, dehydrated in an ethanol series. For transmission electron microscopy (TEM), the filter paper was removed from the syringe and cut in half. The dehydrated sample was infiltrated in 1:1 ethanol:LR White resin for 1 hr, infiltrated in pure LR White for 1 hr, and embedded in LR White overnight at 60 °C. Ultra-thin sections (80-90 nm) were cut with an Ultracut E, Reichert-Jung. Austria ultramicrotome, mounted on collodion-coated copper grids, stained with Reynolds lead citrate, and examined with a JEOL 100CX transmission electron microscope operated at 80 kV. For scanning electron microscopy (SEM), the remaining half of the filter paper used. The filter paper with cells was soaked in Hexamethyldisilazane (HMDS) twice in 30 min. Samples were air dried at room temperature and mounted on SEM stubs. Cell specimens were coated with 25 nm gold palladium using a Hummer II Sputter Coater, and examined on a Cambridge S-260 scanning electron microscope.

4.2.5 Impedance and Video Experiments

4.2.5.1 Cell Buffer and List Sweep Impedance Measurements

The following buffers (Air, dI water, TG+Sucrose+BSA (25mM TRIS, 192 mM Glycine, 83mM sucrose, and 1%BSA), and 1mM PBS at RT) were characterized by pH, osmolarity, and conductivity prior to testing in the chip device. Conductivity measurements were performed using a conductivity meter (Omega, #VDH-7X, Stamford, CT) and Osmolarity using an

osmometer (Wescor Inc., #5520, Logan, UT). Electrical impedance magnitude and phase data of different media (air, DI water, PBS, Tris-Glycine+Sucrose) were collected by list sweep measurements which were performed over the frequency range of 20kHz to 2MHz using the impedance analyzer.

The following buffers: Air, dI water, TrisGly+Sucrose+BSA (25mM TRIS, 192 mM Glycine, 83mM sucrose, and 1%BSA), and 1mM PBS at RT) were characterized by pH, osmolarity, and conductivity prior to testing in the chip device. Optimal cell buffer properties include low conductivity (<1.5mS/cm), physiological osmolarity (300mOsm for cell water balance), and physiological pH (~7.4) for maintaining healthy cells for impedance measurements. Standard 10 mM phosphate-buffered saline (PBS) conductivity is too high (refer to Table 4.1) for being able to acquire sensitive, single-cell impedance-based cell measurements, while dI water, 1 mM PBS, and 25mM TRIS+192 mM Glycine osmolarity is too low for maintaining cell volume/health for cell viability measurements. The custom 25 mM Tris, 192 mM Glycine, 83 mM Sucrose, and 1%BSA low-conductivity cell buffer was selected and deemed ideal for subsequent cell-based impedance measurements.

Table 4.1 Optimization of cell buffers, which maintain cell viability (low conductivity, physiological pH and osmolality) and are compatible with impedance detection.

Cell Buffer Solution	**Conductivity (mS/cm)**	**Osmolality (mM/kg)**	**pH**
dI Water	0.002 ± 0.04	0	6.4
25 mM Tris, 192 mM Glycine	0.35 ± 0.04	180	8.3
25mMTris-192mMGlycine + 83mMSucrose + 1%BSA	1.2 ± 0.04	292	7.6
1 mM PBS	1.2 ± 0.04	56	7.4
10 mM PBS	9.3 ± 0.04	300	7.4

It is important to monitor and preserve parameters of the cell media, such as osmolarity, pH, and conductivity, to maintain eukaryotic cell viability and also maintain compatibility with

the impedance measurement system. The viability of the cells is an important parameter and has been discussed pertaining to a recent microbiology impedance detection scheme that employed tris-glycine+tween20 buffer (33.5 μS/cm), which has extremely low osmolarity and likely imparted significant stress on the cells that were being tested (Banada et al. 2006; Gomez et al. 2001). Often supplemented with sucrose (8.5% (w/v)) and dextrose (0.3% (w/v)), phosphate buffered saline (PBS) is commonly used as the base for the surrounding cell media with reported conductivities ranging from 0.05 mS/cm to 0.56 mS/cm (Broche et al. 2007; Cheng et al. 2007; Cheung et al. 2005; Kuttel et al. 2007; Labeed et al. 2006). Thus, the choice of media should take into consideration both low-conductivity compatibility and the ability to maintain cell viability (Wang et al. 2007).

4.2.5.2 Impedance Signal of Single Cells (Live and Dead)

For the impedance cell measurements, the measurement time was set to short (~5.6 ms) scans taken at 1, 1.5, 1.8, and 2 MHz. Labview impedance data was time-stamped and saved for comparative analysis with video data. The data was further processed with signal processing to smooth out the baseline drifts by normalizing and local averaging (mean-filter) similar to algorithms applied for CD4 on-chip counting (Wang et al. 2008). The cell concentration was adjusted to $\sim 1\text{x}10^5$ cells mL^{-1} to obtain an appropriate density of cells flowing through the microfluidic device. Appropriate cell viability control treatments (live and dead (4mM H_2O_2)) were conducted, where Calcein AM was used as a fluorescent viability indicator. Video stream acquisition was collected on the microscope for correlating video with electrical signals.

4.2.5.3 Video Analysis

To analyze fluorescent videos of live and dead cells to validate electrical measurements, region intensity measurements were collected for live and dead cells for a constant region of

interest (ROI). The average signal intensity was analyzed as relative fluorescence intensity (with respect to the background in the microchannel image).

4.2.5.4 Statistical Analysis

Video analysis experiments with live and dead cells were conducted to obtain appropriate number of cell events (with n=20-25 for each control treatment as described in each experiment). All values are indicated as mean ± SEM. Student's t-test was employed, with $p \leq 0.01$ considered to be significant. For electrical impedance magnitude and phase data analysis, each "n" replicate was composed of at least 20 cell events.

4.3 Results and Discussion

4.3.1 Buffer Characterization

Toxicity of cell buffers at 0.5, 4, and 24 hrs was evaluated via flow cytometry to ensure that cell health was maintained for on-chip cell viability testing (Fig. 4.4). Time points were chosen based on practicality of conducting routine cell experiments where 4 hr would be the longest time cells would be held in the cell buffer in the inlet tubing of the chip. Cells held in 1 mM PBS for any duration tested were not viable, based on calcein staining with no significant difference from the necrotic treatment yielding 8.28 ± 0.41% live cells. There was no significant difference in the percentage of live cells for cells treated with the custom Tris-Gly+Sucrose+BSA buffer at 30min (88.50 ± 0.92%) or 4 hr (89.66 ± 0.28%) as compared to the control held in RPMI+10%FBS (at 30min, 87.15 ± 1.24% and at 4hr, 91.06 ± 0.91%). Thus, the Tris-Gly+Sucrose+BSA solution was deemed acceptable to maintain cell viability before and during on-chip analysis.

The characteristic complex impedance, including magnitude and phase, of various cell buffers in the microchip device is shown in Fig. 4.5. Similar to the results shown by Cho et al. (Cho et al. 2006), air had the highest magnitude (2.06 Mohms at 2 MHz) over the 20kHz to

2MHz frequency spectrum and was found to have an approximately 90 °phase shift, similar to an ideal capacitor. De-ionized water (0.002 mS/cm) and the custom Tris-Glycine buffer (supplemented with sucrose and BSA (1.2 mS/cm)) had magnitudes of 630 kohms and 81.6 kohms respectively at 2 MHz. Standard 10 mM PBS, with the highest conductivity (9.3 mS/cm), has the lowest resistance (54.2 kohms) at 2MHz (Fig. 4.5A).

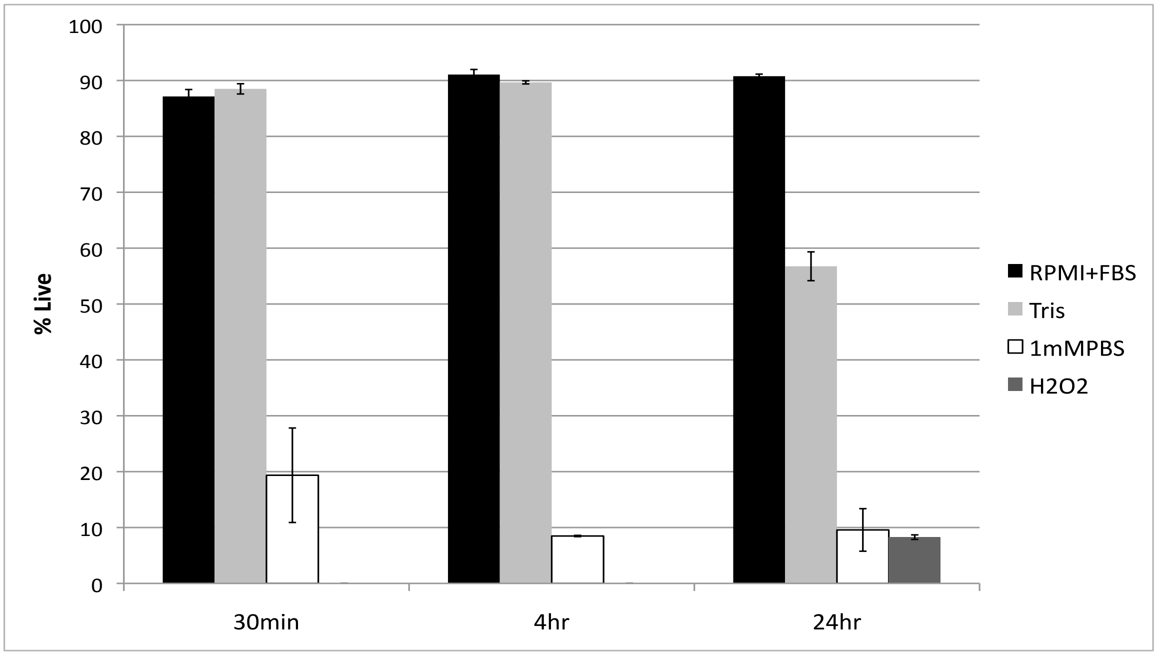

Figure 4.4 Time course of Calcein-labeled Jurkat cells in various cell buffers, RPMI+FBS (Live), TrisGly+Sucrose+BSA (Tris), 1mM PBS, and 4mM H_2O_2 (dead). Percent live is based on flow cytometry gating analysis of Calcein+ cells (30,000 cell events collected; n=3).

The resistance measured in the microchannel was calculated in Eq. 4.1 as a function of the electrode gap, conductivity of the buffer, and area of exposed electrodes by using the 50-µm wide chip geometry and conductivity of buffer solutions (shown in Table 4.1).

$$R = \frac{L}{\sigma_b A_{electrode}} \qquad \text{(Eq. 4.1)}$$

R = resistance due to buffer in the microchannel
L = electrode gap (cm)
σ = buffer conductivity (mS/cm)
A = Area of exposed electrode (cm^2)

Therefore according to Eq. 4.1, given a channel width of 50 μm and an electrode diameter of 76 μm and 1.2 mS/cm Tris-Glycine+Sucrose+BSA cell buffer, the resistance in the microchannel is 91.85 kohms, which is very close to the measured value of 81.6 kohms at 2 MHz. However, the theoretical calculated resistance values for dI water (55.1 Mohms) and 10 mM PBS (11.85 kohms) are not as close to the 2 MHz measured values of 0.63 Mohms and 54.2 kohms respectively. Differences between measured and theoretical values could be attributed to impurities in the buffer, fouling of materials on the electrodes, or slight variations in electrode geometry. The phase of Tris-Glycine (Sucrose+BSA) was -41.8 degrees, while water was -74.8 degrees and PBS was -70.1 degrees at 2 MHz (Fig. 4.5B). It's advantageous to select the buffer with the higher phase, so the system will be more sensitive to detect capacitive changes when a cell is present at the electrodes. In order to maximize sensitivity, the Tris-Gly+Sucrose+BSA buffer was chosen in this system based on low conductivity.

4.3.2 Detection of Cells On-chip

Experiments were conducted to determine if a single cell would have a detectable impedance signal in the microdevice and to find the optimal frequency for acquiring cell measurements. Live cell events were found to correlate with a measured change in impedance phase signal. Relative changes in magnitude and phase were collected for recorded cell events at 1.5, 1.8, and 2 MHz (Fig. 4.6). Relative changes in magnitude at 1.5 and 1.8 MHz were observed as peaks while there is a much smaller relative change in magnitude for a live cell at 2 MHz (Fig. 4.6A). Larger changes in phase were observed for live cell events at 1.8 and 2 MHz while the 1.5 MHz signal is less distinct (Fig. 4.6B). Based on the measured relative change in phase data and increased signals from live cells, the frequency of 2 MHz was selected for subsequent cell analysis. Data was also collected at 100kHz but did not yield appreciable signals

for magnitude and phase (data not shown). The selected frequency of 2 MHz was also chosen by Han and Frazier using a cell capturing cavity and micro-EIS system to distinguish between human breast cancer cells at different pathological (Han and Frazier 2006). In conclusion, the 2 MHz frequency was selected to be ideal for determining the largest Jurkat cell signal for subsequent cell studies given the configuration of this device.

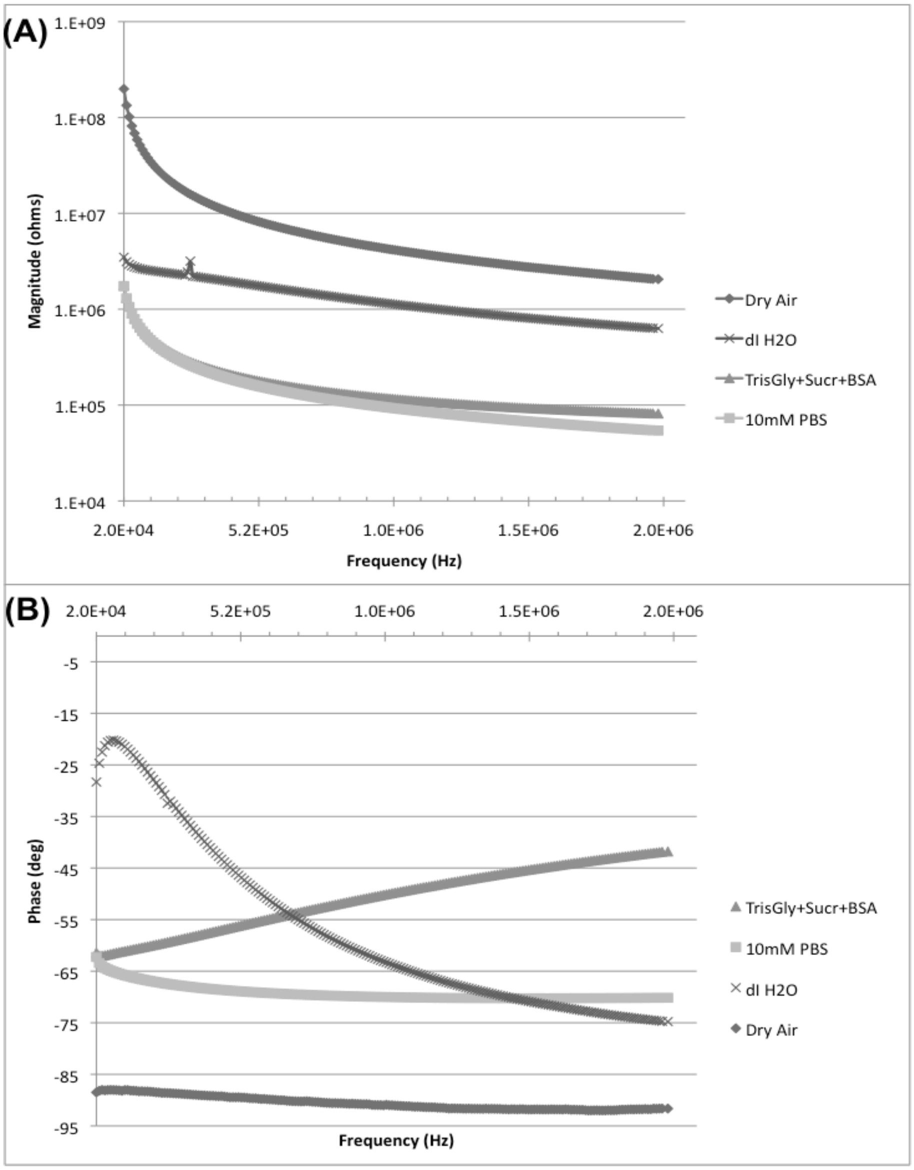

Figure 4.5 Complex impedance (A) Magnitude and (B) Phase of cell buffer solutions (10 mM PBS (9.3 mS/cm), TrisGly (1.2mS/cm), dI water (0.002 mS/cm) as a function of frequency (20kHz- 2 MHz) in the microchip device.

4.3.3 Electron Microscopy of Live and Dead Cells

Electron microscopy imaging was used to qualify differences in membrane morphology and cell size for live and dead Jurkat cells used in this study (Fig. 4.7). TEM indicates a qualitative spatial analysis of the inner cell after fixing, embedding, and staining, while SEM describes the overall cell surface based on shape modifications and membrane alterations. Electron micrographs for live cells (Fig. 4.7A, C) show a rounded cell shape, with complex morphology exhibiting many folds in the cell membrane whereas the dead cell (Fig. 4.7B, D) exhibits a perforated outer membrane and decreased cell size. Similarly, transmission electron (TEM) micrographs show the compromised cell membrane of the dead cell (Fig. 4.7D) while preservation of the intact cell membrane is evident in the live cell (Fig. 4.7C).

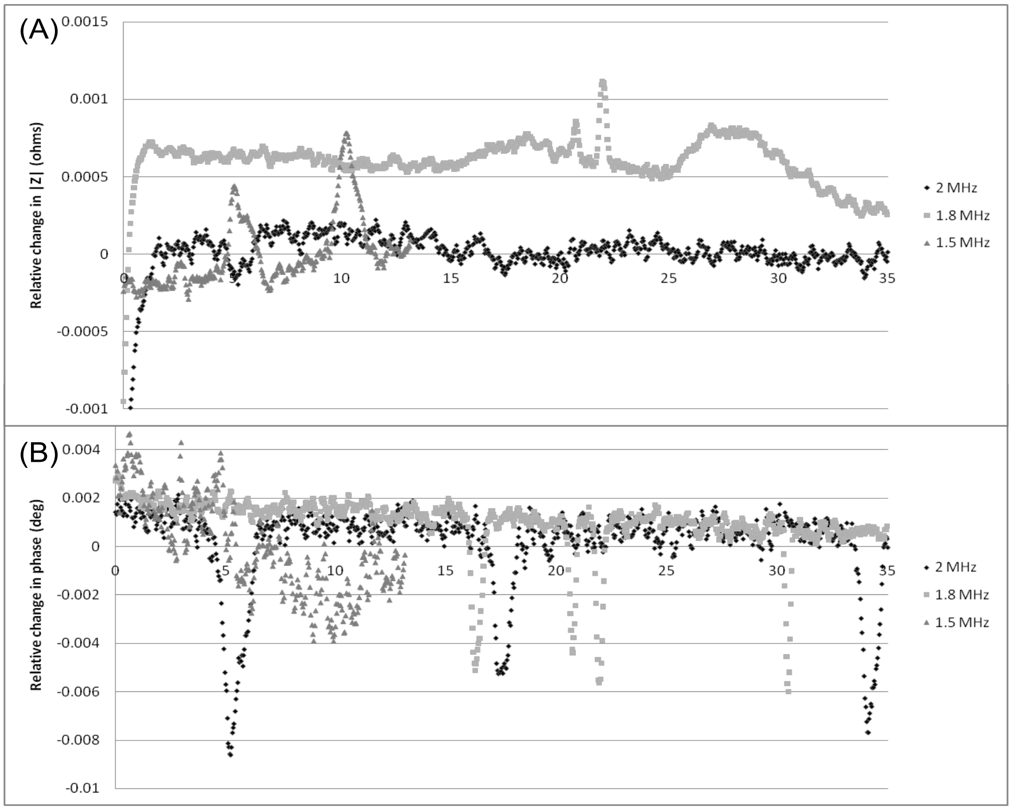

Figure 4.6 Relative change in impedance magnitude (A) and phase (B) for fixed-frequencies (1.5, 1.8, and 2 MHz) of live Jurkat cells passing between Pt electrodes in the microchip device.

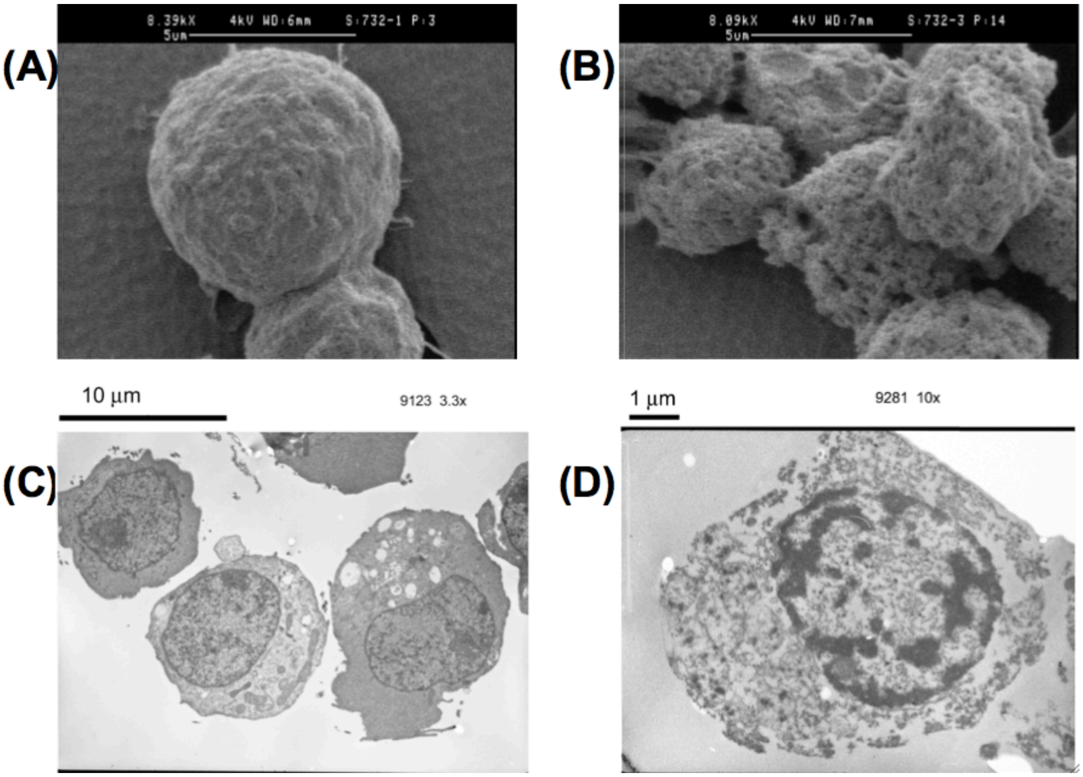

Figure 4.7 Scanning electron micrographs of Jurkat cells (A) Live cell, (B) Dead (4mM H2O2-treated) cell (scale bar: 5um). Transmission electron micrographs of Jurkat cells (C) Live cell (scale bar: 10um), (D) Dead (4mM H2O2-treated) cell (scale bar: 1um)

Wang et al. monitored the morphology of the cell membrane during apoptosis by SEM imaging and correlated these changes to measured membrane capacitance (Wang et al. 2002). As the apoptotic HL-60 cells formed "blebs," there was an increase in smooth areas on the surface of the membrane over a four-hour time frame (images shown in Chapter 1, Fig. 1.16). The increase in smooth areas was suggested to be a result of a loss of microvilli and other membrane features. This decrease in morphological complexity correlated with the observed decrease in membrane capacitance as the cells progressed through apoptosis. Additionally, the crossover frequencies for the necrotic HL-60 cells were in the megahertz range and widely different from the live cell populations (Chapter 1, Fig. 1.17)(Wang et al. 2002), thus supporting the impedance differences observed here between live and necrotic Jurkat cells in our device.

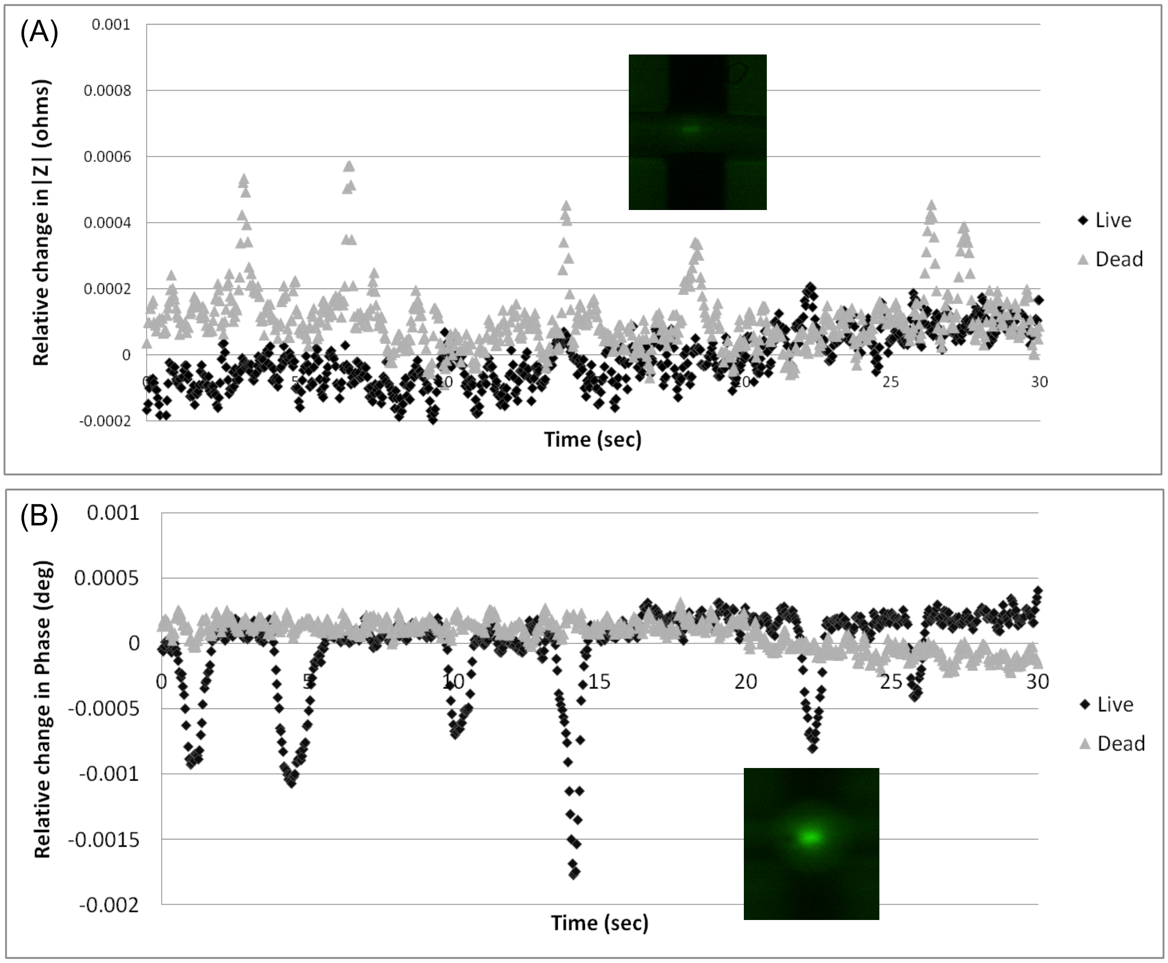

Figure 4.8 Relative change in (A) magnitude, (B) phase for live and dead cells at 2 MHz, where dead cells exhibit noticeable change in magnitude and live cells exhibit a change in phase. Representative FITC images of calcein-labeled dead and live cell events at the detection electrodes are shown in (A) and (B) respectively.

4.3.4 Comparison of Live and Dead Cells at 2MHz

Relative changes in impedance magnitude and phase of live and dead cells detected on-chip at 2 MHz are shown in Fig. 4.8. Dead cells were found to exhibit a change in magnitude (Fig. 4.8A), while live cells exhibit a characteristic change in phase at 2 MHz (Fig. 4.8B). The calcein fluorescence intensity of live and dead cells can be discerned from the cell events shown within each plot. Thus, the viability of a cell can be determined by the complex impedance measurement of the cell event that is collected. Cell size and membrane capacitance govern the impedance signal measured at 2 MHz (Gawad et al. 2001). Other reports in literature describe a

decrease in phase, and concomitant increase in magnitude for impedance-based detection (100 Hz to 5 MHz) of whole bovine chromaffin cells as their ion channels were blocked compared to unblocked chromaffin cells; similar trends were seen in magnitude and phase differences in breast cancer cell lines at 100 kHz (Cho et al. 2009b; Han and Frazier 2006; Han et al. 2007).

The relative change in magnitude and phase data acquired from individual cells can be represented as a 2D plot, similar to multiparameter flow cytometric data analysis (Fig. 4.9). The population distribution illustrates that live and dead cells can be differentiated with the fabricated PMMA microchip device and complex impedance measurements acquired at 2MHz using the Agilent impedance analyzer. Live and dead cell measurements were plotted as a relative change in magnitude vs. relative change in phase at 2 MHz (Fig. 4.9A) and shows clear separation of live and dead cells. Live cells experienced a significantly greater relative change in phase ($0.0007 \pm 8.3 \times 10^{-5}$ deg) compared to the dead cell control ($4.2 \times 10^{-5} \pm 3.1 \times 10^{-5}$ deg), while the dead cells experienced a significantly greater relative change in magnitude ($0.00054 \pm 4.2 \times 10^{-5}$ ohms) compared to the live cells ($6.5 \times 10^{-5} \pm 3.4 \times 10^{-5}$ ohms) (Fig. 4.9B).

In order to obtain optical validation of cell viability based on relative Calcein fluorescence observed from Jurkat cells flowing through the device, relative fluorescence intensity for live and dead cells was compared (20 cells for each treatment were analyzed). Live cells had a significantly higher level of relative fluorescence units (30.3 ± 2.9 RFU) compared to dead cells (4.5 ± 0.9 RFU) (Fig. 4.10). The live cells experienced high levels of Calcein fluorescence, with a relatively larger amount of fluorescence than the dead cells by a factor of 6. Calcein has also been used by van den Berg's group recently for optically determining on-chip viability of adherent cells (Komen et al. 2008).

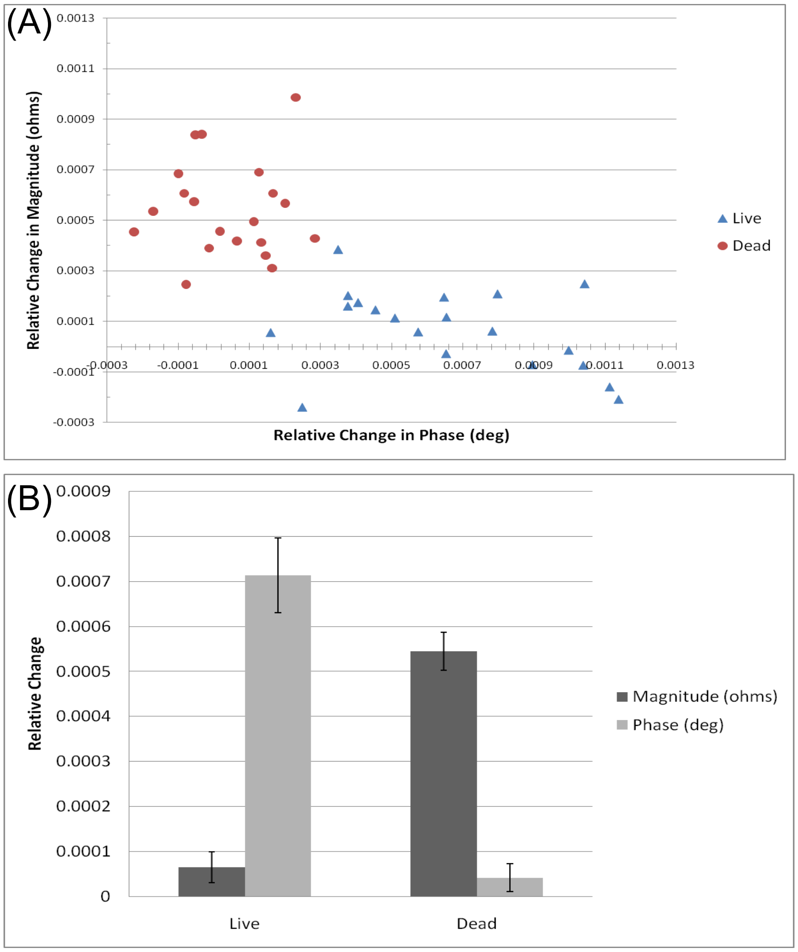

Figure 4.9 (A) Representative 2D plot of change in magnitude versus change in phase, illustrating that live and dead cells can be differentiated using the designed microchip device with impedance measurements at 2MHz, (B) Bar graph illustrating the relative change in magnitude and phase for live (n=20) and dead cells (n=20).

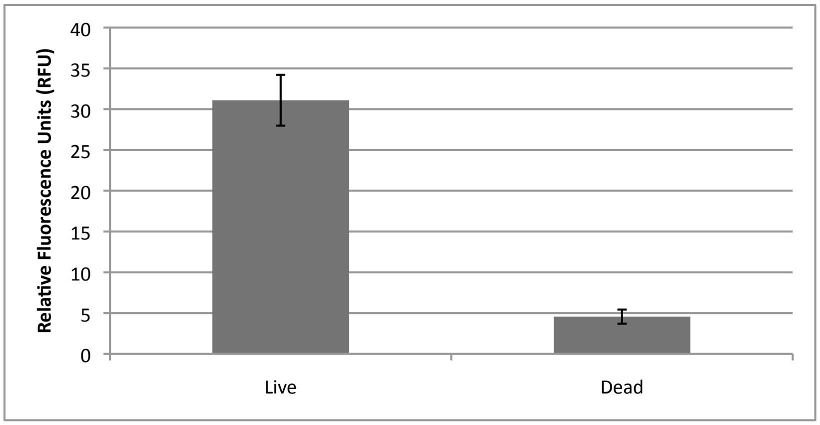

Figure 4.10 Fluorescence measurements (RFU) of Calcein-stained Live and Dead cells using a constant region of interest (ROI) to verify viability status of cells for electrical impedance measurements (n=20).

In Fig. 4.11, a mixed sample of live and dead cells was interrogated with the PMMA microchip device to assess cell viability on the basis of impedance data at a fixed frequency of 2 MHz. The impedance magnitude and phase data reveals a live cell event, subsequently followed by several dead cells, and shows that it is possible to discriminate between live and dead cells within a mixed sample**.**

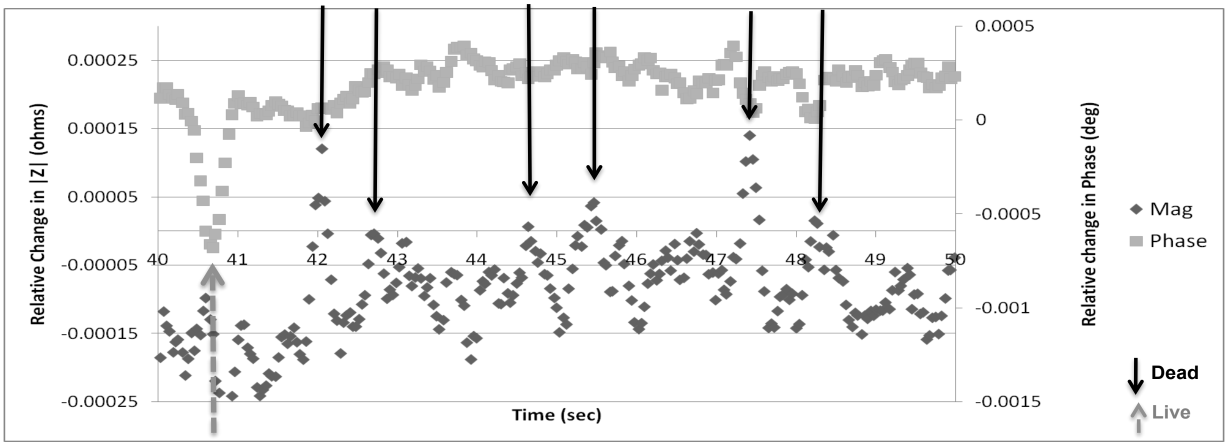

Figure 4.11 Impedance magnitude and phase plot overlays (at 2 MHz) for a mixed (live and dead) sample with grey and black arrows indicating live and dead cell events.

4.4 Conclusion

Studies on the electric analysis of cells are often conducted on the basis of static cell vs. flowing cell measurements, either acquiring bulk measurements or single-cell measurements. Static measurements are useful for determining the density of cells, physiological activity of cells and metabolic substances released. Bulk cell measurements have been reported that use impedance spectroscopy for cell detection and counting using cell lysate in a microfluidic device (Cheng et al. 2007), which found that the impedance magnitude at 760Hz (measured using an Agilent 4284 LCR meter) is a function of number of cells captured on-chip and was successfully able to measure bulk cell concentration using impedance spectroscopy. However this cell lysate device lacks the single-cell detection of whole cells. Other bulk measurement studies employ the

use of static cells to quantify morphological changes in cells and determination of virus infection of cells (Cho et al. 2007; Giaever and Keese 1993).

For single-cell, static impedance measurements, microfabrication methods have been used to create microcantilever arrays to differentiate normal and abnormal red blood cells (RBCs) (Cho et al. 2006). In another single-cell study, a microhole apparatus was fabricated so that negative pressure could be used to capture individual T-lymphoma cells in order to study biologically relevant changes of the cell membrane by conducting impedance measurements at 0.1 to 1 kHz (Cho et al. 2008; Cho and Thielecke 2007; Huang et al. 2003; James et al. 2008).

Impedance measurements of flowing cells employ the use of microfluidic channels and are important for developing high-throughput applications with single-cell resolution. Electroanalytical cell diagnostic applications have advanced considerably since the first electrodes were incorporated into a microfluidic device (Ayliffe et al. 1999), in which magnitude and phase impedance measurements were used to differentiate between human polymorphonuclear leukocytes and teleost fish red blood cells (Ayliffe et al. 1999). Latex beads and erythrocytes impedance studies revealed that different cell sizes, membrane capacitances, and cytoplasm conductivities could be differentiated with impedance using an impedance analyzer (Cheung et al. 2005; Gawad et al. 2001). For example, Renaud and colleagues demonstrated a label-free differentiation of particles and red blood cells (RBCs) with an on-chip cytometer (30 um-wide electrodes) using impedance spectroscopy (350 kHz to 20 MHz) (Cheung et al. 2005). Another MEMS-based cytometer method was employed on the basis of cellular DNA content to detect apoptosis- in which apoptotic cells have less DNA content than live diploid cells (Sohn et al. 2000). The “capacitance cytometry” technique was based on the observed linear relationship between DNA content of eukaryotic cells and the change in

capacitance that is observed when an individual fixed cell passes across a 1-kHz electric field (Sohn et al. 2000). There is no report within the capacitance cytometry discussion to show that the signal of this device could be a function of cell viability; however, it is worthy to note that capacitance changes at 1kHz can be measured at the single-cell level. A Voltametric method was used to study apoptosis in K562 cells using a small flow chamber assembled with a 3-electrode system and a voltametric analyzer (Feng et al. 1999). A measured decrease in faradic response of apoptotic cells is related to the electrochemical activity of cells and was reported to be a function of the apoptotic-altered electrochemical cell activity. The significance of this voltammetric method is relevant for the electrical impedance detection methods and shows potential for being able to sensitively monitor cell viability changes in the early stages (Feng et al. 1999).

Cell death is associated with a large change in dielectric properties, which is important for the purposes of detection. Pethig and Markx have described how a dying cell undergoes important changes in dielectric properties (Pethig and Markx 1997). The cell membrane of a live cell consists of a highly insulating lipid bilayer, which contains many proteins, while the cell interior contains membrane-covered particulates (mitochondria, vacuoles, nucleus, and dissolved charged molecules). The conductivity of the cell interior (1 S/m) is 10^7 times more conductive than the cell membrane (10^{-7} S/m) (Pethig and Markx 1997). Upon cell death, a necrotic cell's cell membrane becomes permeable, and its conductivity increases by a factor of 10^4 as the cell contents are dispersed into the surrounding medium.

Membrane capacitance is a critical parameter to consider when comparing live and dead cells. Membrane capacitance describes the surface of the membrane that acts as a barrier, accumulating ionic species in response to the applied electric field, while membrane conductance is a measure of the net transport of ionic species through pores and ion channels, which is

influenced by an applied electric field. Alterations in the DEP properties, the “dielectric-phenotype,” which are related to capacitance and conductivity of membrane, cell size, and intracellular components have been described for apoptotic and necrotic cells and demonstrate potential for applications related to quantification of cell viability (Wang et al. 2002). Alterations in cytoplasm conductivity, membrane capacitance, and dielectrophoretic properties have also been studied for various cell types (HL-60, K562, and adherent cell lines) (Arndt et al. 2004; Labeed et al. 2006; Wang et al. 2002).

Several studies have examined dielectric cell properties related to cell viability using dielectrophoretic methods, which incorporate microscopy and optical observations (to determine cell diameter and cross-over frequency). Dielectrophoretic techniques have been demonstrated to have potential for detecting and quantifying normal, apoptotic, and necrotic cells using a human myelogenous leukemia cell line (HL-60), in which the cell main membrane was the main focus of study (Wang et al. 2002). Early apoptotic cells were observed to undergo an increase in cytoplasm conductivity (0.28 to 0.50 S/m), loss of cell volume, and change in membrane capacitance. The nature of this DEP data is based on single-cell measurements that were manually collected. The biophysical parameters from DEP of K562 cells (Labeed et al. 2006) were determined by applying the collected data with best-fit modeling using the single-shell model. Lymphoma cells have also been modeled as double-shell model because of their large, round nuclei which occupies more than 1/3 of the intracellular space (having a mean nuclear volume of 40%) (Irimajiri et al. 1979). In the case of dying yeast cells, the mode of cell death has been reported to be important, especially in the case of solubilization of the membrane, which results in greater changes in membrane capacitance (Patel et al. 2008). These studies show that

dielectric properties of cells differ among various cell populations and can be used to assess different stages of cell viability.

Electric cell-substrate impedance sensing (ECIS) is an impedance method applied for monitoring cell behavior of adherent cells. In ECIS, cells are grown in chambers equipped with floor electrodes. These cells are exposed to a weak AC field, and the cell plasma membrane acts as an insulator, changing the impedance of the electrode as the field goes around or through the cells. ECIS measures impedance differences as a function of cell density, cell-cell interaction, cell morphology, and interaction between the cells and electrodes (Giaever and Keese 1993). ECIS-Zθ (Applied BioPhysics, Inc., Troy, NY), the real-time cell-based system (RT-CES®) (ACEA Biosciences Inc., San Diego, CA), and the CellKey™ System (MDS Analytical Technologies, Sunnyvale, CA), based on cellular dielectric spectroscopy, are several recently developed commercial platform systems that allow for measuring the impedance of a population of adhered cells while the majority of applications of ECIS are cell transport, signal transduction, proliferation, and toxicology. Bioelectrical impedance has also been used to successfully monitor apoptosis based on changes in cell shape of immobilized adherent endothelial cells grown on planar 2 mm diameter gold-film electrodes (Arndt et al. 2004), although ECIS methods are not able to be directly incorporated into a flow-through system as shown here.

The differential analysis of live and dead cells was demonstrated here without necessitating the need for precisely modeling changes in resistive and capacitive properties of live and dead cells. Similarly, Olivia and colleagues studied fast cell-by-cell analysis of infected RBC's for discriminating infected vs. non-infected cells without measuring the absolute dielectric cell properties (Kuttel et al. 2007). The equivalent circuit model (ECM) for this PMMA microfluidic impedance-based chip system is a function of cell size, dielectric properties

of the buffer and cell, and microelectrode chip geometry. Changes in cell size and membrane integrity (capacitance) of live and dead cells are likely to contribute to the measured complex impedance changes at 2 MHz. The influence of cell behavior (C_{mem} and cytoplasm conductivity) on impedance has been examined theoretically for a similar microelectrode system where the modeling efforts combined Maxwell's Mixture theory (MMT) with ECM for a parallel electrode design (Sun et al. 2008). This particular model illustrated a measurable change in impedance magnitude at 2 MHz as the membrane capacitance changes, which suggests that live and dead cells could exhibit the relative differences measured within our study.

A novel polymer-based cell viability microchip was designed, fabricated, and tested as a non-optical, impedance-based system for detecting Jurkat cell viability. An advantage of this system would be the ability to collect cell viability information on the single-cell level based on a characteristic electrical signal, rather than relying on microscopy or flow cytometry. Fluorescent video imaging is combined with quantitative electroanalytical data using an impedance analyzer and Calcein viability indicator to discriminate live and necrotic cells. In order to study the cellular impedance measurements at the single-cell level, it was essential that the microdevices be fabricated with the particular cell type in mind, while having the flexibility of changing a few dimensions for any future cell-specific applications, thus the 50-um wide x 76-um deep channel will likely work for many mammalian cells. The integrated sidewall electrode design success is in agreement with recently reported advantages of the parallel-facing, sidewall electrodes over the planar electrodes (Cho et al. 2009b; Sun et al. 2007; Sun et al. 2008). We are currently employing methods to model the electric field in the microchip in order to design the most sensitive electrode design and chip geometries for interrogation of 12 μm- diameter Jurkat cells. This study provides a basis for conducting microfluidic flow-through cell viability studies in

real-time without the use of expensive fluorescent labels. Ultimately, all of these parameters are important for furthering the realm of quantitative BioMEMS for high-throughput and point-of-care diagnostic applications.

4.5 References

Adams AA, Okagbare PI, Feng J, Hupert ML, Patterson D, Gottert J, McCarley RL, Nikitopoulos D, Murphy MC, Soper SA. 2008. Highly efficient circulating tumor cell isolation from whole blood and label-free enumeration using polymer-based microfluidics with an integrated conductivity sensor. Journal of the American Chemical Society 130(27):8633-8641.

Ahn CH, Choi JW, Beaucage G, Nevin JH, Lee JB, Puntambekar A, Lee JY. 2004. Disposable Smart lab on a chip for point-of-care clinical diagnostics. Proceedings of the Ieee 92(1):154-173.

Arndt S, Seebach J, Psathaki K, Galla HJ, Wegener J. 2004. Bioelectrical impedance assay to monitor changes in cell shape during apoptosis. Biosensors & Bioelectronics 19(6):583-594.

Ayliffe HE, Frazier AB, Rabbitt RD. 1999. Electric impedance spectroscopy using microchannels with integrated metal electrodes. Journal of Microelectromechanical Systems 8(1):50-57.

Banada PP, Liu YS, Yang LJ, Bashir R, Bhunia AK. 2006. Performance evaluation of a low conductive growth medium (LCGM) for growth of healthy and stressed Listeria monocytogenes and other common bacterial species. International Journal of Food Microbiology 111(1):12-20.

Bao N, Wang J, Lu C. 2008. Recent advances in electric analysis of cells in microfluidic systems. Analytical and Bioanalytical Chemistry 391(3):933-942.

Broche LM, Bhadal N, Lewis MP, Porter S, Hughes MP, Labeed FH. 2007. Early detection of oral cancer - Is dielectrophoresis the answer? Oral Oncol 43(2):199-203.

Chao TC, Ros A. 2008. Microfluidic single-cell analysis of intracellular compounds. Journal of the Royal Society Interface 5:S139-S150.

Cheng X, Liu YS, Irimia D, Demirci U, Yang LJ, Zamir L, Rodriguez WR, Toner M, Bashir R. 2007. Cell detection and counting through cell lysate impedance spectroscopy in microfluidic devices. Lab on a Chip 7(6):746-755.

Cheung K, Gawad S, Renaud P. 2005. Impedance spectroscopy flow cytometry: On-chip label-free cell differentiation. Cytometry Part A 65A(2):124-132.

Cho S, Becker S, von Briesen H, Thielecke H. 2007. Impedance monitoring of herpes simplex virus-induced cytopathic effect in Vero cells. Sensors and Actuators B-Chemical 123(2):978-982.

Cho S, Castellarnau M, Samitier J, Thielecke H. 2008. Dependence of impedance of embedded single cells on cellular behaviour. Sensors 8(2):1198-1211.

Cho S, Gorjup E, Thielecke H. 2009a. Chip-based time-continuous monitoring of toxic effects on stem cell differentiation. Annals of Anatomy-Anatomischer Anzeiger 191(1):145-152.

Cho SB, Thielecke H. 2007. Micro hole-based cell chip with impedance spectroscopy. Biosensors & Bioelectronics 22(8):1764-1768.

Cho SB, Thielecke H. 2008. Electrical characterization of human mesenchymal stem cell growth on microelectrode. Microelectronic Engineering 85(5-6):1272-1274.

Cho Y, Kim HS, Frazier AB, Chen ZG, Shin DM, Han A. 2009b. Whole-Cell Impedance Analysis for Highly and Poorly Metastatic Cancer Cells. Journal of Microelectromechanical Systems 18(4):808-817.

Cho YH, Yamamoto T, Sakai Y, Fujii T, Kim B. 2006. Development of microfluidic device for electrical/physical characterization of single cell. Journal of Microelectromechanical Systems 15(2):287-295.

Feng J, Cheng K, Luo GA, Wang RJ, Wang DB. 1999. A voltammetric method for analyzing the apoptosis of K562 cells. Analytical Communications 36(11-12):379-381.

Gawad S, Schild L, Renaud P. 2001. Micromachined impedance spectroscopy flow cytometer for cell analysis and particle sizing. Lab on a Chip 1(1):76-82.

Giaever I, Keese CR. 1993. A Morphological Biosensor for Mammalian-Cells. Nature 366(6455):591-592.

Gimsa J, Muller T, Schnelle T, Fuhr G. 1996. Dielectric spectroscopy of single human erythrocytes at physiological ionic strength: Dispersion of the cytoplasm. Biophysical Journal 71(1):495-506.

Gomez R, Bashir R, Sarikaya A, Ladisch MR, Sturgis J, Robinson JP, Geng T, Bhunia AK, Apple HL, Wereley S. 2001. Microfluidic Biochip for Impedance Spectroscopy of Biological Species. Biomedical Microdevices 3:201-209.

Gomez-Sjoberg R, Morisette DT, Bashir R. 2005. Impedance microbiology-on-a-chip: Microfluidic bioprocessor for rapid detection of bacterial metabolism. Journal of Microelectromechanical Systems 14(4):829-838.

Han A, Frazier AB. 2006. Ion channel characterization using single cell impedance spectroscopy. Lab on a Chip 6(11):1412-1414.

Han A, Yang L, Frazier AB. 2007. Quantification of the heterogeneity in breast cancer cell lines using whole-cell impedance spectroscopy. Clinical Cancer Research 13(1):139-143.

Holmes D, Morgan H, Green NG. 2006. High throughput particle analysis: combining dielectrophoretic particle focussing with confocal optical detection. Biosens Bioelectron 21(8):1621-30.

Huang Y, Sekhon NS, Borninski J, Chen N, Rubinsky B. 2003. Instantaneous, quantitative single-cell viability assessment by electrical evaluation of cell membrane integrity with microfabricated devices. Sensors and Actuators a-Physical 105(1):31-39.

Irimajiri A, Hanai T, Inouye A. 1979. Dielectric theory of multi-stratified shell-model with its application to a lymphoma cell. Journal of Theoretical Biology 78(2):251-269.

James CD, Reuel N, Lee ES, Davalos RV, Mani SS, Carroll-Portillo A, Rebeil R, Martino A, Apblett CA. 2008. Impedimetric and optical interrogation of single cells in a microfluidic device for real-time viability and chemical response assessment. Biosensors & Bioelectronics 23(6):845-851.

Jones TB. 1995. Electrical forces and torques on bioparticles. Electrostatics 1995. p 135-144.

Kerr JFR, Wyllie AH, Currie AR. 1972. Apoptosis - Basic Biological Phenomenon with Wide-Ranging Implications in Tissue Kinetics. British Journal of Cancer 26(4):239-257.

Kleparnik K, Horky M. 2003. Detection of DNA fragmentation in a single apoptotic cardiomyocyte by electrophoresis on a microfluidic device. Electrophoresis 24(21):3778-83.

Komen J, Wolbers F, Franke HR, Andersson H, Vermes I, van den Berg A. 2008. Viability analysis and apoptosis induction of breast cancer cells in a microfluidic device: effect of cytostatic drugs. Biomedical Microdevices 10(5):727-737.

Koopman G, Reutelingsperger CPM, Kuijten GAM, Keehnen RMJ, Pals ST, Vanoers MHJ. 1994. Annexin-V for Flow Cytometric Detection of Phosphatidylserine Expression on B-Cells Undergoing Apoptosis. Blood 84(5):1415-1420.

Krinke D, Jahnke HG, Panke O, Robitzki AA. 2009. A microelectrode-based sensor for label-free in vitro detection of ischemic effects on cardiomyocytes. Biosensors & Bioelectronics 24(9):2798-2803.

Kuttel C, Nascimento E, Demierre N, Silva T, Braschler T, Renaud P, Oliva AG. 2007. Label-free detection of Babesia bovis infected red blood cells using impedance spectroscopy on a microfabricated flow cytometer. Acta Tropica 102(1):63-68.

Labeed FH, Coley HM, Hughes MP. 2006. Differences in the biophysical properties of membrane and cytoplasm of apoptotic cells revealed using dielectrophoresis. Biochimica Et Biophysica Acta-General Subjects 1760(6):922-929.

Lu H, Gaudet S, Schmidt MA, Jensen KF. 2004. A microfabricated device for subcellular organelle sorting. Anal Chem 76(19):5705-12.

Patel PM, Bhat A, Markx GH. 2008. A comparative study of cell death using electrical capacitance measurements and dielectrophoresis. Enzyme and Microbial Technology 43(7):523-530.

Pethig R, Kell DB. 1987. The passive electrical properties of biological systems: their significance in physiology, biophysics and biotechnology. Phys Med Biol 32(8):933-70.

Pethig R, Markx GH. 1997. Applications of dielectrophoresis in biotechnology. Trends in Biotechnology 15(10):426-432.

Pohl HA. 1951. The motion and precipitation of suspensoids in divergent electric fields. Journal of Applied Physics 22(7):869-871.

Schade-Kampmann G, Huwiler A, Hebeisen M, Hessler T, Di Berardino M. 2008. On-chip non-invasive and label-free cell discrimination by impedance spectroscopy. Cell Proliferation 41(5):830-840.

Sohn LL, Saleh OA, Facer GR, Beavis AJ, Allan RS, Notterman DA. 2000. Capacitance cytometry: measuring biological cells one by one. Proc Natl Acad Sci U S A 97(20):10687-90.

Spegel C, Heiskanen A, Skjolding LHD, Emneus J. 2008. Chip based electroanalytical systems for cell analysis. Electroanalysis 20(6):680-702.

Sun T, Gawad S, Green NG, Morgan H. 2007. Dielectric spectroscopy of single cells: time domain analysis using Maxwell's mixture equation. Journal of Physics D-Applied Physics 40(1):1-8.

Sun T, Green NG, Morgan H. 2008. Analytical and numerical modeling methods for impedance analysis of single cells on-chip. Nano 3(1):55-63.

Tabuchi M, Baba Y. 2004. Self-contained on-chip cell culture and pretreatment system. J Proteome Res 3(4):871-7.

Tamaki E, Sato K, Tokeshi M, Sato K, Aihara M, Kitamori T. 2002. Single-cell analysis by a scanning thermal lens microscope with a microchip: Direct monitoring of cytochrome c distribution during apoptosis process. Analytical Chemistry 74(7):1560-1564.

Valero A, Merino F, Wolbers F, Luttge R, Vermes I, Andersson H, van den Berg A. 2005. Apoptotic cell death dynamics of HL60 cells studied using a microfluidic cell trap device. Lab on a Chip 5(1):49-55.

Vaux DL, Strasser A. 1996. The molecular biology of apoptosis. Proceedings of the National Academy of Sciences of the United States of America 93(6):2239-2244.

Vykoukal DM, Gascoyne PRC, Vykoukal J. 2009. Dielectric characterization of complete mononuclear and polymorphonuclear blood cell subpopulations for label-free discrimination. Integrative Biology 1(7):477-484.

Wang LS, Flanagan L, Lee AP. 2007. Side-wall vertical electrodes for lateral field microfluidic applications. Journal of Microelectromechanical Systems 16(2):454-461.

Wang XJ, Becker FF, Gascoyne PRC. 2002. Membrane dielectric changes indicate induced apoptosis in HL-60 cells more sensitively than surface phosphatidylserine expression or DNA fragmentation. Biochimica Et Biophysica Acta-Biomembranes 1564(2):412-420.

Wang YN, Kang YJ, Xu DY, Chon CH, Barnett L, Kalams SA, Li DY, Li DQ. 2008. On-chip counting the number and the percentage of CD4+T lymphocytes. Lab on a Chip 8(2):309-315.

Wheeler AR, Throndset WR, Whelan RJ, Leach AM, Zare RN, Liao YH, Farrell K, Manger ID, Daridon A. 2003. Microfluidic device for single-cell analysis. Analytical Chemistry 75(14):3581-3586.

Wolbers F, Haanen C, Andersson H, Van den Berg A, Vermes I. 2005. Chapter 8, Analysis of Apoptosis on Chip: Why the move to chip technology? In: Berg HAaAvd, editor. Lab-on-Chips for Cellomics Micro and Nanotechnologies for Life Science. Netherlands: Kluwer Academic Publishers. p 197-224.

Yang MS, Li CW, Yang J. 2002. Cell docking and on-chip monitoring of cellular reactions with a controlled concentration gradient on a microfluidic device. Analytical Chemistry 74(16):3991-4001.

Yi CQ, Li CW, Ji SL, Yang MS. 2006a. Microfluidics technology for manipulation and analysis of biological cells. Analytica Chimica Acta 560(1-2):1-23.

Yi CQ, Zhang Q, Li CW, Yang J, Zhao JL, Yang MS. 2006b. Optical and electrochemical detection techniques for cell-based microfluidic systems. Analytical and Bioanalytical Chemistry 384(6):1259-1268.

CHAPTER 5. CONCLUSIONS AND FUTURE DIRECTIONS

5.1 Conclusion

The goal of this project was to combine molecular and microdevice methods to characterize and quantify viability of single cells. Fluorescent-based assays were optimized for adherent HeLa and suspension Jurkat cells and were used as a tool for validation of a microfabricated diagnostic device. Cell and substrate/surface interactions were also considered for designing a microfluidic device that can be used to characterize cell viability for quantitative biomedical and cell biology applications, which require label-free, real-time monitoring of cells.

A review of current literature in the area of cell viability and microfluidic platforms was presented in the first chapter. Also, electrochemical properties of eukaryotic cells and electrochemical changes involved in cell viability have brought much attention to the dielectric differences that have been reported for live, apoptotic, and necrotic cells. However, there is still no published account of an impedance-based, label-free, single-cell viability detection of flowing cells on a chip.

In Chapter 2, studies were conducted to evaluate the freezing response of HeLa and Jurkat cells in the presence of commercially available nanoparticles, NPs (Palmitoyl Nanogold®, Nanoprobes) and a commonly used cryoprotective agent, DMSO. By fitting a model of water transport to the experimentally determined volumetric shrinkage data, the membrane permeability parameters were obtained. A generic optimal cooling rate equation was then used to predict the optimal rates of freezing HeLa and Jurkat cells in the presence and absence of DMSO and NPs. To further investigate the predicted optimal cooling rates, the cells were cooled at three controlled freezing rates in the presence and absence of DMSO and NPs using a commercially available controlled rate freezer. The post-thaw viability and apoptotic response

of treated HeLa cells were evaluated after 18 h post-thaw incubation time. Jurkat cells demonstrated an increase in their adhesion after treatment and remain adhered to the culture plate, preventing their flow cytometric analysis. For HeLa cells, the post-thaw results show that the presence of NPs increased the measured post-freeze apoptotic response at 1 °C min^{-1} when compared to higher cooling rates and suggests a possible therapeutic use of NPs in cryodestructive procedures.

Cell-substrate interactions and cell viability were quantified using light and fluorescent microscopy. Here, experiments were conducted to characterize the adhesion effect of serum on Jurkat cells, to resuspend these transiently adhered, viable cells, and to investigate several applications of this observed adhesive effect. There is a distinct relationship between the presence of serum in media and transient adhesion of Jurkat cells on tissue-treated polystyrene surfaces. Adhered Jurkat cells were resuspended and the cells were evaluated for viability and preservation of a T-cell marker (CD3) via fluorescent microscopy and flow cytometric analysis. Enhanced cellular delivery of DNA oligonucleotides was shown for the transiently adhered state. Under proper conditions (serum and substrate), a single suspension cell was studied via fluorescence microscopy, which would otherwise prove difficult. This technique permitted DiBAC fluorescence time-lapse imaging of adhered Jurkat cells exhibiting transient depolarization in an electric-field, and we also show the ability to monitor progression of apoptosis in real-time by time-lapse microscopy of transiently adhered Jurkat cells in serum-free media.

A novel polymer-based cell viability microchip was designed, fabricated, and tested as a non-optical, impedance-based system for detecting Jurkat cell viability at the single-cell level as discussed in Chapter 4. An advantage of this system would be the ability to collect cell viability

information on the single-cell level based on a characteristic electrical signal, rather than relying on microscopy or flow cytometry. Fluorescent video imaging was combined with quantitative electroanalytical data using an impedance analyzer and Calcein viability indicator to discriminate live and necrotic cells. In order to study the cellular impedance measurements at the single-cell level, it was essential that the microdevices be fabricated with the particular cell type in mind, while having the flexibility of changing a few dimensions for any future cell-specific applications- thus the 50-um wide x 76-um deep channel will likely work for many mammalian cells. The integrated sidewall electrode design success is in agreement with some of the recently reported advantages of the parallel facing, sidewall electrodes over the planar electrodes (Cho et al. 2009b; Sun et al. 2007; Sun et al. 2008). The work in chapter 4 provides a basis for conducting cell viability studies in real-time without the use of expensive fluorescent labels or optical instrumentation.

The overall objective of this dissertation was to combine molecular and microfabrication methods to characterize and quantify viability of single cells. Fluorescent flow-based assays were optimized and employed as a tool for optical validation of cell viability using a microfluidic diagnostic device. Biological cell properties, media parameters, and surface/substrate interactions were also evaluated and considered in the design of the microfluidic chip device to characterize cell viability for quantitative biomedical and cell biology applications, which strive for label-free, real-time monitoring of single cells in a flow-through device. From the fluorescence and electrical impedance data collected, the proof-of-concept for rapid, electroanalytical quantification and characterization of Jurkat cell viability on a microfluidic chip platform is demonstrated. This device has the potential for various label-free cell biology applications, such as identifying cell phenotype/behavior, characterizing stem cell differentiation, or evaluating

nanotechnology-related applications, such as efficiency of nanoparticle- or carbon nanotube-uptake in cells, that are beyond the resolution and capabilities of optical techniques. Thus, the acquired electrical impedance measurements of single cell events discussed within this dissertation show promise for furthering the realm of BioMEMS for high-throughput, point-of-care diagnostic applications.

5.2 Future Considerations

The project findings presented here allow for a new quantitative technique for monitoring and evaluating cell viability of single cells. Application of this device for additional quantitative cell applications, such as apoptosis, could be further characterized by employing an improved video camera that is capable of simultaneous/rapid, two-color fluorescence for assessing live, necrotic, and apoptotic cells. Further modeling of the electric field in the microchip and the cell as an equivalent circuit model (ECM) could provide for additionally enhanced iterations of chip designs to determine the optimal electrode geometry (though not necessarily within the capabilities of microfabrication resources at this time) and optimal frequency (possibly at frequencies beyond 2 MHz of the Agilent impedance analyzer) for discrimination of live and necrotic Jurkat cells. Thus, the following future directions address additional applications, modeling features, and instrumentation alternatives that could be considered.

5.2.1 Applications of the Microchip Device

The future of an apoptosis lab-on-a-chip would be beneficial for diagnostics. Apoptosis, programmed cell death, is a major target of drug discovery in fields, such as oncology, gerontology, and recombinant biotechnology (Feng et al. 1999; Valero et al. 2005). A BioMEMS microchip for detecting single-cell apoptosis in a sensitive, targeted, quantitative method in real-time has enormous potential for high-throughput pharmacological screening of

drugs. There is much literature describing the critical need for an apoptosis chip device; however, a successful apoptosis device to detect single cells has yet to be reported.

While working on this dissertation, fluorescent-based apoptosis assays were optimized with Jurkat cells using confocal microscropy to adequately differentiate live, apoptotic, and necrotic controls (Fig. 5.1). However, our inability to complete apoptosis on-chip studies is due to lack of microscope optical validation capabilities. The possibility of sorting live and dead cells downstream from the detection electrodes could be approached with electrokinetic cell manipulation while employing hydrodynamic focusing techniques such as the bead shown in Fig. 5.2. Also, further explorations were conducted with Jurkat cells labeled with palymitodyl-Nanogold nanoparticles (used in Chapter 2) to perform TEM and SEM imaging to confirm Au-NP's on membrane surface in order to determine if the impedance-based system could be capable of quantifying and confirming nanoparticle-labelled cells. However due to the combination of the EM protocol's repeated wash steps and the 1 nm-nanoscale of the gold nanoparticles, the NP-loaded cells were not able to be optically validated (images not shown) for subsequent impedance exploration.

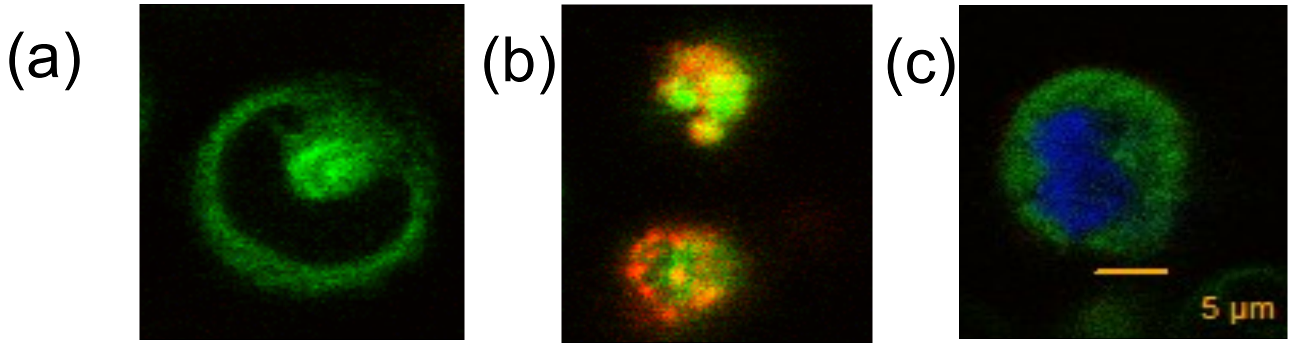

Figure 5.1 Confocal images using 63X (a) Live cell with DiBAC, (b) Apoptotic (10 uM Camptothecin for 4hrs) (AnnexinV+), (c) Necrotic (4 mM H2O2 for 18hrs) (Sytox+). Scale bar is 5 um.

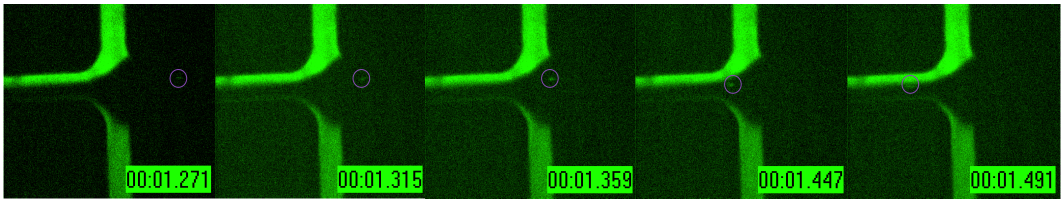

90° HD focusing (1:1 sheath:sample flow rate) – FITC bead focused in 15μ/hr (1xTris-glycine) flow
* 45° HD focusing geometry also tested

Figure 5.2 Cellular and microfluidic control methods, such as hydrodynamic focusing, were examined as a technique for positioning the cell/particle along the centerline of the channel future downstream cell sorting applications.

5.2.2 Modeling

CoventorWare^{TM} microfluidic simulation software (Coventor, Inc. Cary, NC), including CoventorWare Designer^{TM} and Analyzer^{TM} software, was used to create chip designs and perform microfluidic simulations. Two- and three-dimensional simulations were performed in order to model a biological cell (using a single-shell model) passing by sidewall and coplanar electrodes in which an electric field is applied within a microchannel (Fig. 5.3). Using this software, the applied electric field (5μA AC sine wave), electrode geometry (width and spacing), and properties of the surrounding buffer were also defined for the 76 um diameter electrodes in a 50 um-wide channel completed filled with 1.2 mS cm^{-1} buffer (Fig. 5.4). These simulations were used to improve understanding of electrode geometry (size and spacing) and provide the groundwork for the projected change in electric field. A 2-dimensional simulation of the fringe effects is shown in Fig. 5.5; these fringe effects have been reported to have a greater effect on impedance measurements as cell size increases (Sun et al. 2008) The results from these simulations indicated that the sidewall electrode design is more sensitive than the co-planar microelectrode configuration. This is congruent with the parallel facing electrode design that was reported to have improved sensitivity as compared to planar designs and supports the findings that the microelectrode dimensions should ideally be comparable to particle size (latex

bead used in confocal optical detection and other theoretical modeling approaches)(Holmes et al. 2006; Sun et al. 2007; Sun et al. 2008).

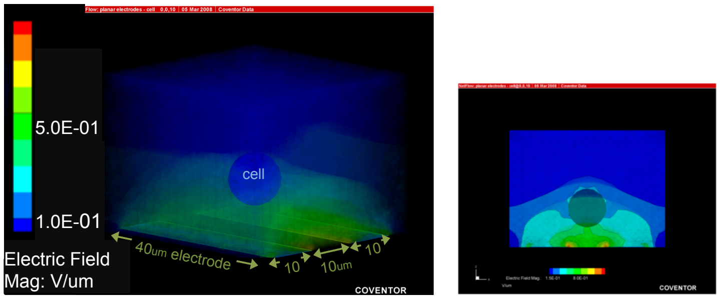

Planar electrodes

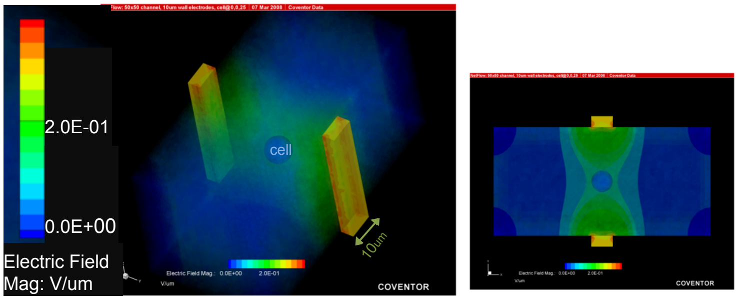

Side wall electrodes

Figure 5.3 (top) Electric field distribution within a 10 um-wide microchannel with 10 um-wide (top) coplanar, (bottom) sidewall electrodes with a single 10 um-diameter cell present at the electrodes and cell buffer completely filling the channel (σ_{buffer} =1.2 mS cm^{-1}) CoventorWare^{TM} microfluidic simulation software (Coventor, Inc. Cary, NC).

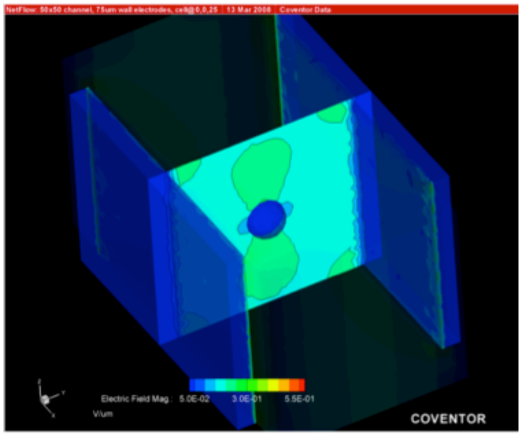

Figure 5.4 Representative image showing the distribution of electric field in the 50 um-wide microchannel with 75 um-wide sidewall microelectrodes,with a single 10 um-diameter cell present at the electrodes and cell buffer completely filling the channel (σ_{buffer} =1.2 mS cm^{-1}) CoventorWare^{TM} microfluidic simulation software (Coventor, Inc. Cary, NC).

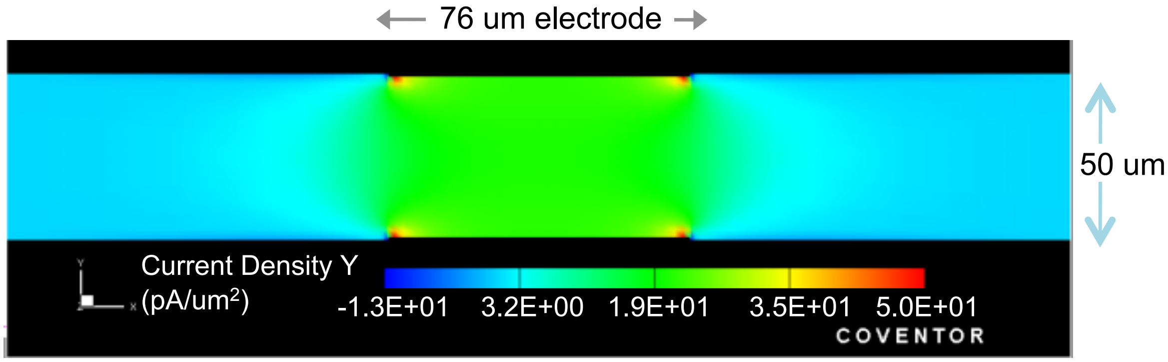

Figure 5.5 Two-dimensional simulation showing DC current density profile and fringe effects at the 76 um-wide microelectrodes when 5V applied at electrodes in 50 um-wide channel filled with water (CoventorWare^{TM} microfluidic simulation software, Coventor, Inc. Cary, NC).

By combining dielectric cell properties and fluid dynamics, the representative equivalent circuit model (ECM) for this microchip/electrode system (Fig. 5.6) could be determined and created in SPICE electrical circuit modeling software (Cadence, Inc., USA) for validating the measured change in capacitance and resistance when a cell is present at the electrodes. Electrical double dayer (Cdl) is the electrode-electrolyte interface impedance, which is gradually reduced as the frequency increases (above 1 MHz) and the sensitivity of the system for detecting cell properties improves (Sun et al. 2008). SPICE model output could be used to better describe the measured change in capacitance and resistance when a live vs. dead cell is present at the electrodes. Thus, by combining Comsol and SPICE ECM's, there is the potential to predict the magnitude and phase changes expected as a function of frequency for live, dead (and possibly apoptotic) cells, which experience changes in membrane capacitance related to viability (Sun et al. 2008).

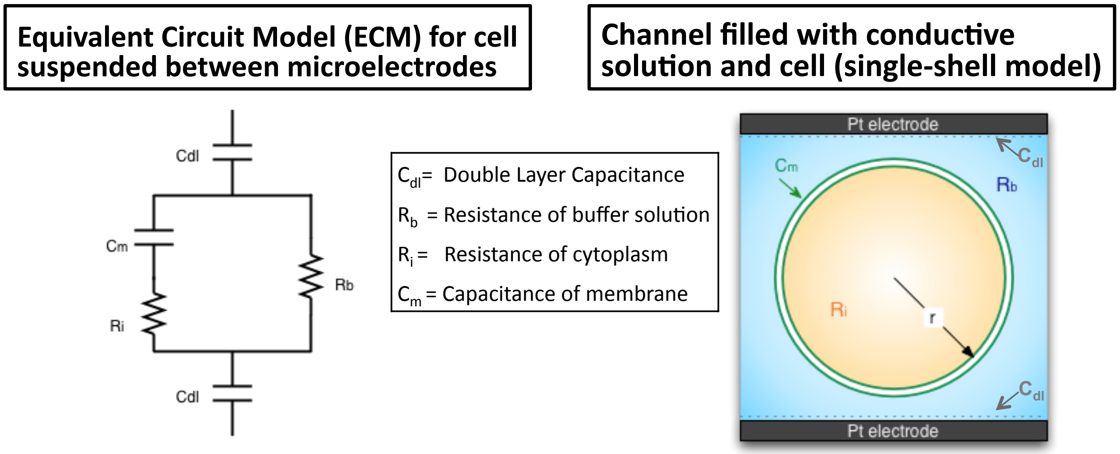

Figure 5.6 Equivalent electrical circuit model of eukaryotic biological cell suspended in buffer solution at detection electrodes in the microfluidic chip, where R_b is equivalent resistance of the cell buffer. C_m is equivalent capacitance of the cell membrane. R_i is equivalent resistance of the cytoplasm. C_{DL} is the electrical double layer capacitance.

5.2.3 Electrode Alternatives for Improved Production of BioMEMS Chip Device

For improving production of these devices, more advanced methods for incorporating electrodes into PMMA microdevices could be considered, such as the side-wall electrode design in which the electrodes are vertically located in the side walls of SU-8 microchannels by using multilayer SU-8 lithography (Wang et al. 2007). According to Wang et al. (2007), the electrode width and spacing were accurately defined by the photolithography and the height (30μm) by the electroplating time. To improve alignment and ensure that the electrodes will be embedded in the channel, the microchannel was designed to be ~5μm wider than the gap between the electrodes. Also, another group has added silver particles to SU8 (an epoxy photoresist used in soft LIGA lithography) to characterize its use as a conductive composite photoresist for patterning microelectrodes (Jiguet et al. 2005). The conductive composite structure was found to have stable dielectric properties from room temperature to glass-transition temperature, and can be loaded with higher silver particles to decrease electrode resistance. The electrical

conductivity of the SU8-silver composite ranged 0.0001-1 Ω-cm, depending on the silver volume fraction added and thermal treatment applied (Jiguet et al. 2005).

In a collaborative effort with John Osiri, we explored using a commercially available silver-nanoparticle-embedded SU-8 product (Jiguet et al. 2005) and making our own Pt-SU8 nanocomposite as a comparison to the milled-wire approach. The conductive SU8 composites (60um thick, 1 cm wide, and 3cm long) were cured on a PMMA substrate (Fig 5.7), and electrical properties were measured using a potentiostat (Parstat 2273). The use of this approach as a microelectrode alternative has potential for future, improved fabrication methods.

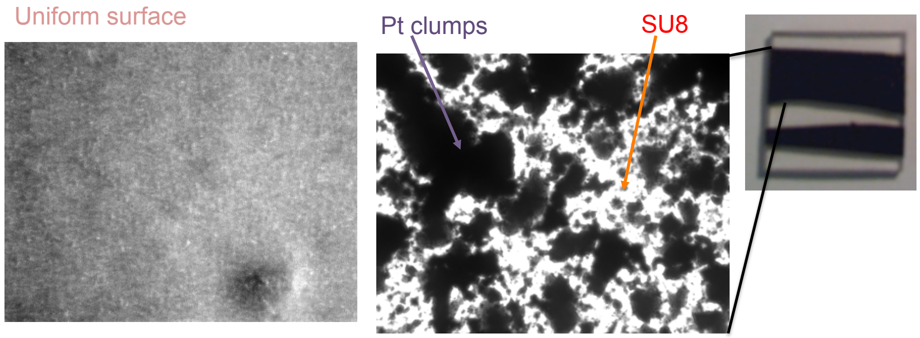

SU8-20%-Ag-after UV curing (commercially purchased)

SU8-Pt- No surfactant was used and Unsonicated sample

(a) (b) (c)

Figure 5.7 SU8-Ag nanocomposites that were explored as microelectrode alternative (A) 40X image of uniform SU8-20%Ag after curing, (B) SU8-Pt nanocomposite with clumps, (C) Nanocomposite that was applied and cured on PMMA substrate.

Production of the current PMMA chip design involves much tedious, sustained steps, and the micromilling of the Pt wire is not an exact, guaranteed technique for each chip. For example, 25% of the chips fabricated with this approach result in a "poor" milled-through electrode, such as the burr shown in Fig. 5.8. While the chip fabrication used throughout Chapter 4 has been sufficient for establishing proof-of-concept for the differential analysis of live and dead cells at

the single-cell level, this current fabrication method does not lend itself to high-throughput fabrication given the need to mill through each chip/wire.

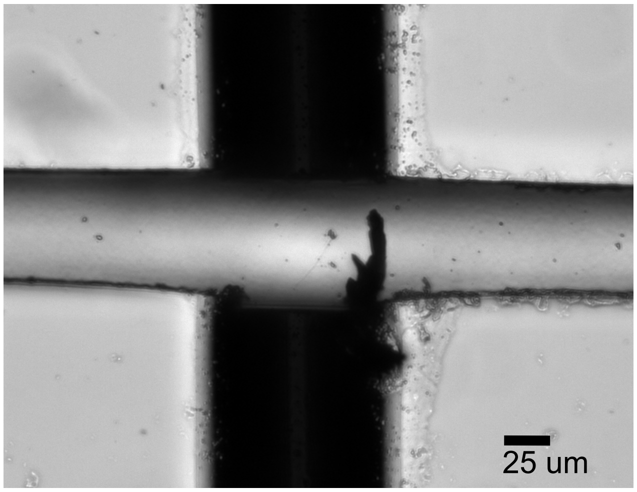

Figure 5.8 Demonstration of "poor" milled-through electrode where a burr obstructs the microchannel.

Additional techniques that have been used to create 3D microelectrodes include: one group that has created carbon 3-D microelectrodes using a carbon SU-8 process, in which the distance between the electrodes can be precisely controlled using lithography (Park and Madou 2005) and another group that fabricated a 3D silicon electrode using silicon (single crystal) with <100> crystallographic orientation, p-type, heavy-doped (conductive) with a resistivity in the range of 1-1.5 μΩ-cm (Tay et al. 2007). Ultimately, more extensive, continued modeling and the advent of more advanced, robust high-precision microelectrode fabrication technologies are important for improvements of this quantitative, sensitive impedance-based BioMEMS device for discriminating cell viability at the single-cell level.

5.3 References

Holmes D, Morgan H, Green NG. 2006. High throughput particle analysis: combining dielectrophoretic particle focussing with confocal optical detection. Biosens Bioelectron 21(8):1621-30.

Jiguet S, Bertsch A, Hofmann H, Renaud P. 2005. Conductive SU8 photoresist for microfabrication. Advanced Functional Materials 15(9):1511-1516.

Park BY, Madou MJ. 2005. 3-D electrode designs for flow-through dielectrophoretic systems. Electrophoresis 26(19):3745-3757.

Sun T, Green NG, Gawad S, Morgan H. 2007. Analytical electric field and sensitivity analysis for two microfluidic impedance cytometer designs. Iet Nanobiotechnology 1(5):69-79.

Sun T, Green NG, Morgan H. 2008. Analytical and numerical modeling methods for impedance analysis of single cells on-chip. Nano 3(1):55-63.

Tay FEH, Yu LM, Pang AJ, Iliescu C. 2007. Electrical and thermal characterization of a dielectrophoretic chip with 3D electrodes for cells manipulation. Electrochimica Acta 52(8):2862-2868.

Wang LS, Flanagan L, Lee AP. 2007. Side-wall vertical electrodes for lateral field microfluidic applications. Journal of Microelectromechanical Systems 16(2):454-461.

APPENDIX A: AUTHORIZATION FOR REPRODUCTIONS

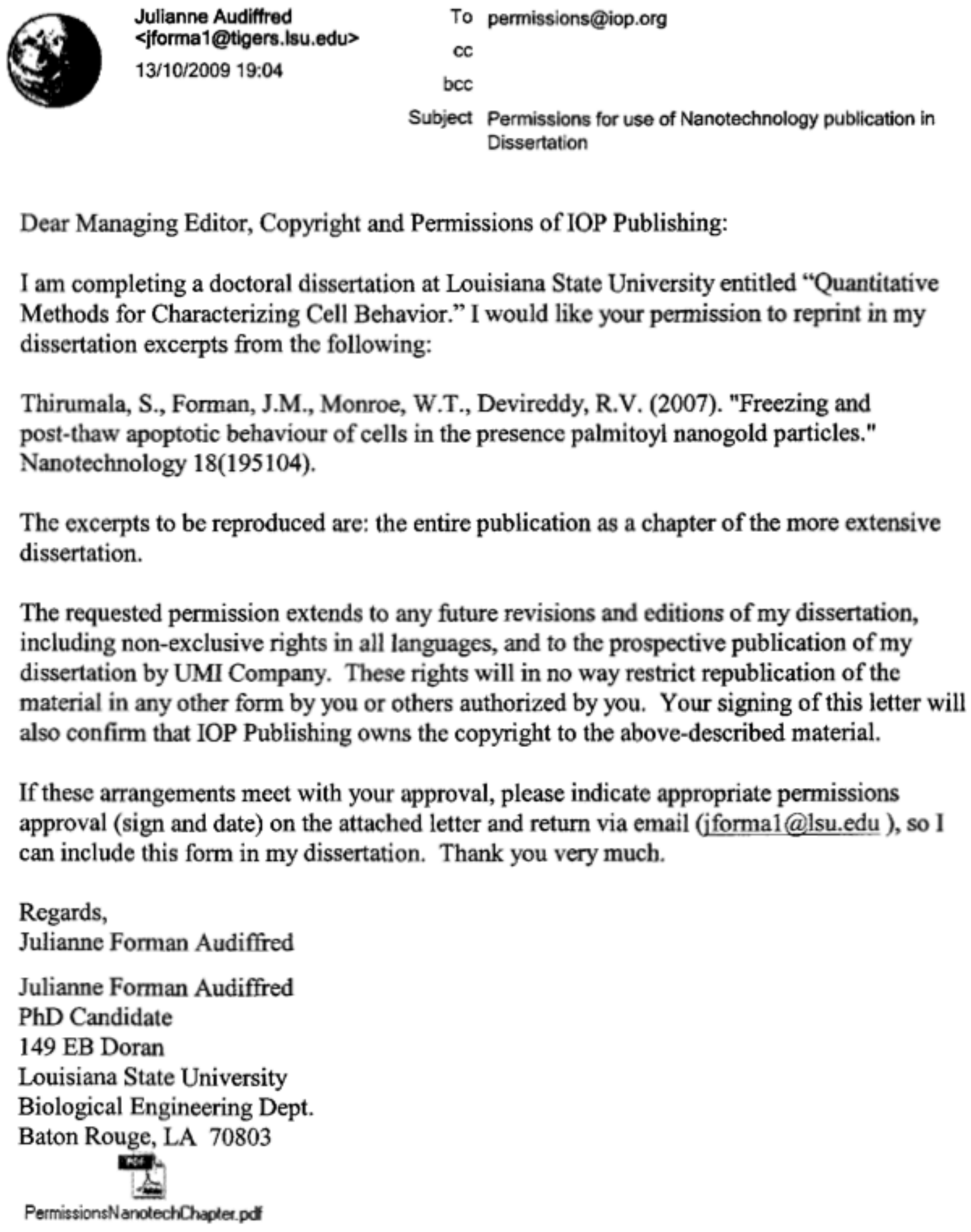

Julianne Audiffred
<jforma1@tigers.lsu.edu>
13/10/2009 19:04

To permissions@iop.org
cc
bcc
Subject Permissions for use of Nanotechnology publication in Dissertation

Dear Managing Editor, Copyright and Permissions of IOP Publishing:

I am completing a doctoral dissertation at Louisiana State University entitled "Quantitative Methods for Characterizing Cell Behavior." I would like your permission to reprint in my dissertation excerpts from the following:

Thirumala, S., Forman, J.M., Monroe, W.T., Devireddy, R.V. (2007). "Freezing and post-thaw apoptotic behaviour of cells in the presence palmitoyl nanogold particles." Nanotechnology 18(195104).

The excerpts to be reproduced are: the entire publication as a chapter of the more extensive dissertation.

The requested permission extends to any future revisions and editions of my dissertation, including non-exclusive rights in all languages, and to the prospective publication of my dissertation by UMI Company. These rights will in no way restrict republication of the material in any other form by you or others authorized by you. Your signing of this letter will also confirm that IOP Publishing owns the copyright to the above-described material.

If these arrangements meet with your approval, please indicate appropriate permissions approval (sign and date) on the attached letter and return via email (jforma1@lsu.edu), so I can include this form in my dissertation. Thank you very much.

Regards,
Julianne Forman Audiffred

Julianne Forman Audiffred
PhD Candidate
149 EB Doran
Louisiana State University
Biological Engineering Dept.
Baton Rouge, LA 70803

PermissionsNanotechChapter.pdf

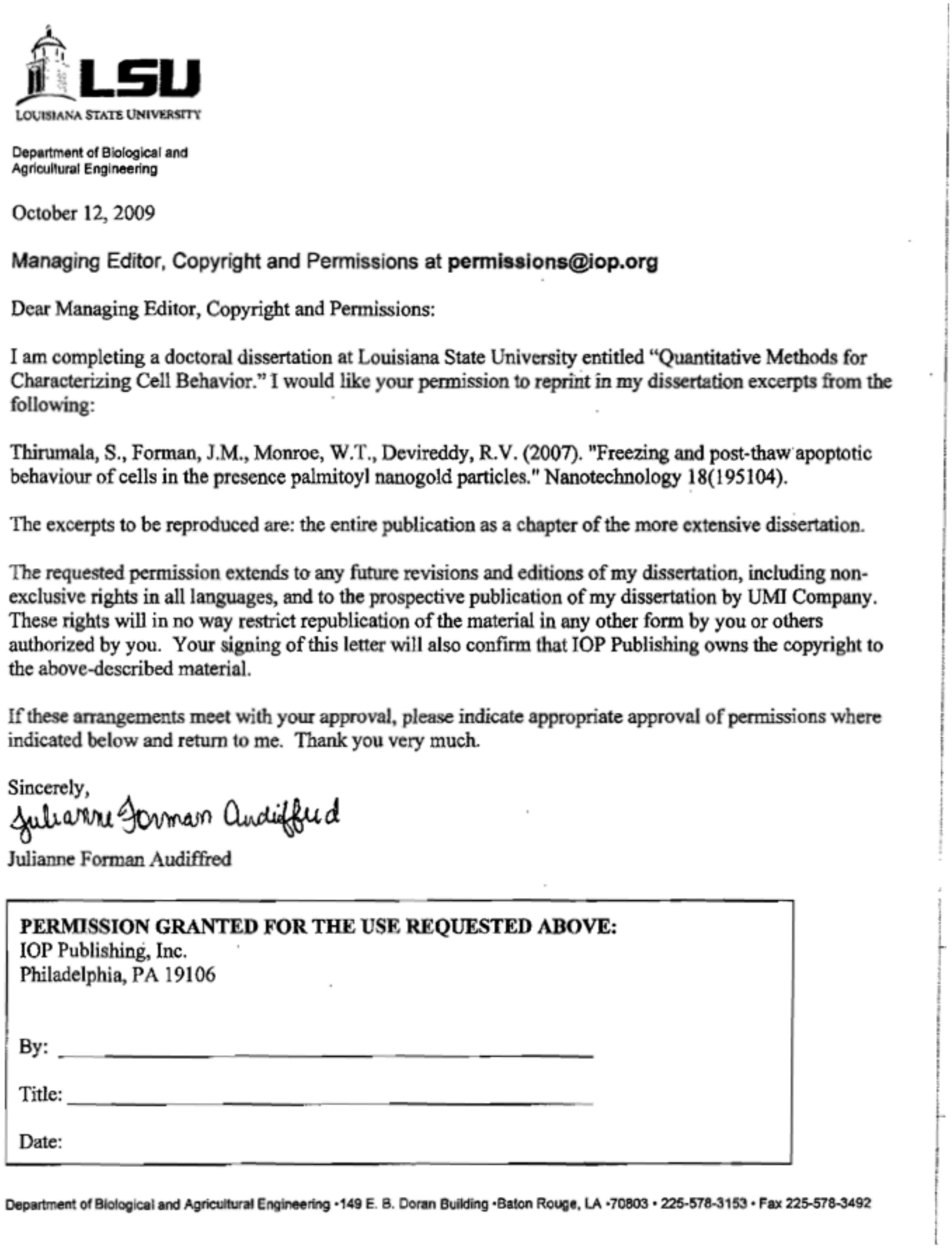

LSU
LOUISIANA STATE UNIVERSITY

Department of Biological and
Agricultural Engineering

October 12, 2009

Managing Editor, Copyright and Permissions at **permissions@iop.org**

Dear Managing Editor, Copyright and Permissions:

I am completing a doctoral dissertation at Louisiana State University entitled "Quantitative Methods for Characterizing Cell Behavior." I would like your permission to reprint in my dissertation excerpts from the following:

Thirumala, S., Forman, J.M., Monroe, W.T., Devireddy, R.V. (2007). "Freezing and post-thaw apoptotic behaviour of cells in the presence palmitoyl nanogold particles." Nanotechnology 18(195104).

The excerpts to be reproduced are: the entire publication as a chapter of the more extensive dissertation.

The requested permission extends to any future revisions and editions of my dissertation, including non-exclusive rights in all languages, and to the prospective publication of my dissertation by UMI Company. These rights will in no way restrict republication of the material in any other form by you or others authorized by you. Your signing of this letter will also confirm that IOP Publishing owns the copyright to the above-described material.

If these arrangements meet with your approval, please indicate appropriate approval of permissions where indicated below and return to me. Thank you very much.

Sincerely,
Julianne Forman Audiffred
Julianne Forman Audiffred

PERMISSION GRANTED FOR THE USE REQUESTED ABOVE:
IOP Publishing, Inc.
Philadelphia, PA 19106

By: ______________________________

Title: ______________________________

Date:

Department of Biological and Agricultural Engineering • 149 E. B. Doran Building • Baton Rouge, LA • 70803 • 225-578-3153 • Fax 225-578-3492

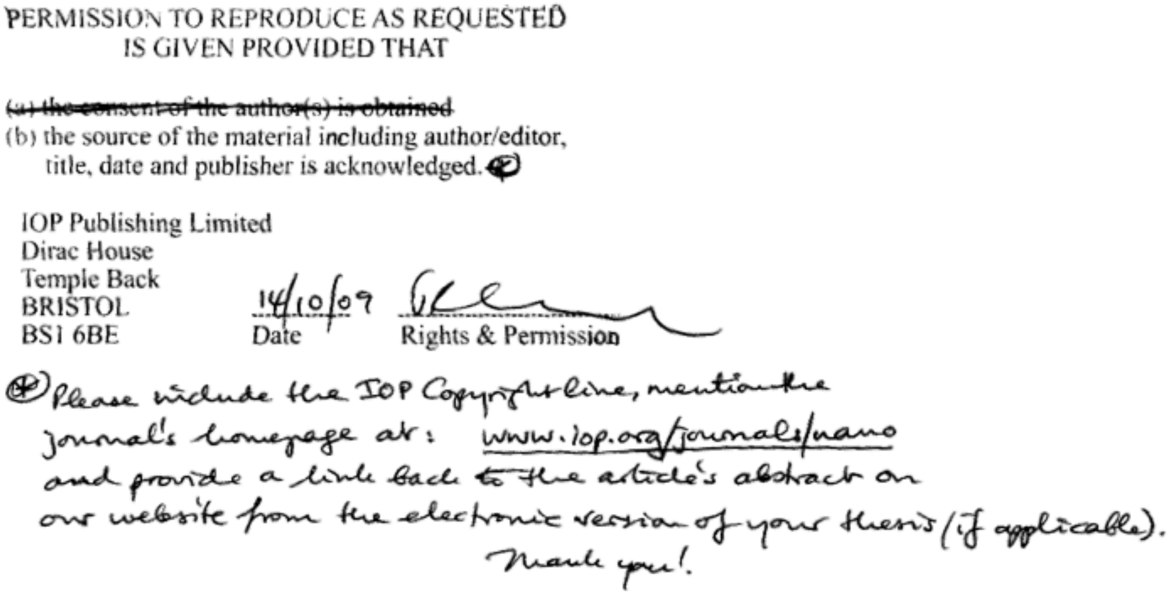

PERMISSION TO REPRODUCE AS REQUESTED
IS GIVEN PROVIDED THAT

~~(a) the consent of the author(s) is obtained~~
(b) the source of the material including author/editor,
title, date and publisher is acknowledged. ⊕

IOP Publishing Limited
Dirac House
Temple Back
BRISTOL
BS1 6BE

14/10/09
Date

Rights & Permission

⊕ Please include the IOP Copyright line, mention the journal's homepage at: www.iop.org/journals/nano and provide a link back to the article's abstract on our website from the electronic version of your thesis (if applicable).

Thank you!

APPENDIX B: EXPERIMENTAL PROTOCOLS

B.1. Flow-based Methods

B.1.a. Flow Cytometry-Annexin V/SYTOX Green Fluorescent Validation Protocol

A. Observe and take brightfield images of cells seeded in 12-well plate before harvesting
   1) Induce apoptosis for positive apoptotic-control (staurosprine) and necrosis for necrotic control (2mM H_2O_2)

B. Harvest cells
   1) Keep floaters (for HeLa cells) in 5mL Falcon flow cytometry tubes
   2) Wash 0.6 mL PBS
   3) Add 0.6mL 0.25% trypsin. Allow 5-7 minutes for cells to detach from the bottom of the dish.
   4) Add 0.6 mL of DMEM-RS (+3% FBS)
   5) Transfer cells in solution to 5 mL cytometer tube
   6) Spin down at 2.4rpm on mini-spin for 5minutes
   7) Aspirate carefully using 1 mL pipettor

C. Stain (Staining steps are done under the hood with the light off)
   1) Add 100 mL of prepared 1X Annexin Binding Buffer (Molecular Probes Vybrant#3 kit) to achieve cell density of $1x10^6$ cells/mL
      i. Add 5mL Annexin V-FITC
      ii. Add 1 mL Propidium Iodide (100ug/mL)
      (Note: Double glove when using PI, and dispose of PI tips appropriately)
   2) Keep tubes protected from light
   3) Vortex gently and incubate cells for 15 minutes covered in the dark at room temperature
   4) Spin down at 2.4rpm on mini-spin for 5minutes
   5) Aspirate carefully
   6) Add 300 mL PBS (with Calcium and Magnesium) to each tube for flow cytometry

D. Run flow cytometry at Veterinary Medicine
   1) Take labeled sheet and numbered tubes to Vet Med with cell sample tubes covered in foil and on ice
   2) Analyze samples on flow cytometer using appropriate filter settings

B.2. Cell-Substrate Interactions

B.2.a. Fluorescent Microscopy- Jurkat Annexin V-AlexaFluor-568/SYTOX Green

1. Seed Jurkat cells in 12-well plates using hemocytometer (target cell density for staining 18hrs: 1x10^6 cells/mL)
    i. Dilute cell suspension as needed for targeted seeding density
    ii. Add 0.6mL mL cell suspension/well
2. Perform treatments (Live, Dead, Apoptotic, and Live-unlabelled as control)
    i. Live – RPMI+FBS only
    ii. Necrotic- 2mM H_2O_2 – 18 hrs
    iii. Apoptotic - 10 μM Camptothecin (4-6hrs) (stock CPT is 2mM soln)
3. Harvest Cells
    i. Spin down at 1.9rpm on mini-spin for 5min
    ii. Aspirate and resuspend cells in 0.6 mL cold PBS
    iii. Centrifuge for 5 min @ 1.9 rpm on mini-spin
4. Validate desired cell density with hemocytometer cell count
    i. Use 10 μL of cell suspension – slowly pipette to notch at edge of hemocytometer
    ii. View at 10X – Cell Count of main grid (volume = 0.0001 ml) *Omit cells touching lateral sides of main grid from count
    iii. Use Excel Cell-Count Calculator to determine total cell #
5. Resuspend cells in AnnexinV-Binding Buffer (100 μL)
    i. Or Based on cell count: Add buffer to final conc. of **1x10^6 cells/mL** :
6. Add Stains
    i. Add 5uL Annexin V-AlexaFluor-568 (per 100 μL cell suspension)
    ii. Add 1uL SYTOX Green (5 μM) --- 1 μL (per 100 μL suspension) = 50nM conc.
7. Incubate at RT --- 15 minutes (cover with foil)
8. Centrifuge (5 min at 1.9 rpm on mini-spin),
9. Aspirate and resuspend with 100 μL PBS+Ca+Mg
10. Image cells using BF and FL microscopy (FITC and TX RED filter sets) at 20X

*Expected Results: Live - Low SYTOX+, Low Annexin V+; Dead-High SYTOX+, High Annexin V+; Apoptotic-Only Annexin V+

SYTOX Green --- Raw Reagent 5mM soln in DMSO (Rec Eukaryotic staining: 10nM - 1μM)

- **Dilution to 5 μM SYTOX**: add 1 μL of 5mM SYTOX to 1000 μL of solution
- 1 μL of 5 μM SYTOX added to 100 μL of cell susp = 50 nM SYTOX
- *within range: 10nM - 1 μM

Annexin V-568 --- Range: 5-25μL per 100 μL cell suspension

Annexin-V Binding Buffer: 10mM HEPES, 140mM NaCl, 2.5 mM $CaCl_2$ --- pH 7.4

1) Add 0.130 g HEPES, 0.409 g NaCl, 0.018g $CaCl_2$
2) Add 40 ml HPLC water
3) pH 40 ml of soln. &add 1 M NaOH or 1 N HCL as necessary to reach pH = 7.4
    a. Added 100 + 5μL (total 105 μL) of HCL (started at pH=9.5)
4) Add 10ml HPLC water to reach final volume of 50ml

B.2.b. MTT Cell Proliferation Assay Protocol

Required Materials:

MTT Reagent (Cat. TA5355)	Fridge (Rm 102, shelf 4)
MTT Detergent (whirlpak bag)	JFA drawer at RT
RPMI (with Serum)	Fridge (Rm 102, shelf 4)
PBS (CMF)	Fridge (Rm 102, shelf 4)
OptiMEM	Fridge (Rm 102, shelf 4)

This assay has been used to measure cell proliferation of jurkat and hela cells as a result of photoexposure and variations in substrate. The entire assay takes 3 days to complete and has to be done in a sterile environment to prevent contamination.

1. Incubate the cells in 12-well plate over night (+8hrs) post-treatment
2. Retrieve cells from incubator, and under the sterile hood
    a. Add 60 uL MTT reagent to each well, including the RPMI blank wells.
3. Incubate the cells for 2-4 hours.
4. Retrieve cells from incubator and check for a purple precipitate that should form.
    a. This should be clearly visible to the naked eye after 2-4 hours and will appear as dark purple “dirt”.
5. Once this is visible, under the sterile hood,
    a. Add 600 uL MTT detergent.
    b. Be sure to pipette slowly as this detergent tends to be very bubbly. **DO NOT SHAKE the cell solution!** Incubate the cells over night (8+ hours).
6. Measure the absorbance of each well at 570 nm on spectrophotometer.
    a. Blank the spectrophotometer using 80 microliters of the RPMI, MTT, and Detergent solution found in 2 of the 12 wells.
        i. There is a program on the spectrophotometer already configured named “MTT”.
    b. Use 80 uL of each cell solution to measure the absorbance at 570 nm. Pipette very slowly and do not completely empty the pipette each time a cuvette is filled. This helps to prevent bubbles in the cuvette that would cause the spectrophotometer to give an inaccurate reading. **Do not read the absorbance of a cuvette with bubbles in it**!
    c. Refill a new cuvette.
    d. Save data to a floppy disk, frequently checking on a computer to ensure your data has been saved. **NEVER TRUST YOUR DATA WILL BE ON THE FLOPPY DISK! ALWAYS DOUBLE CHECK!**

Analyze the data on Excel using the Absorbance at 570 nm. Average the Absorbance of live controls and divide each individual treatment by the average to get % control. Calculate standard error. Generate a bar graph with this data (+error bars).

B.2.c. Adhesion Cell Count Protocol

The following protocol was conducted to determine qualitative and quantitative representations of transiently attached cells.

1. Cell adhesion assays were conducted on various 12-well substrates (standard tissue-treated polystyrene, non tissue-treated polystyrene, and fibronectin-coated standard tissue-treated polystyrene).
2. Seed Jurkat E6.1 cells (ECAC, Sigma) in 12-well plates in either RPMI-RS (Hyclone, Logan, UT) medium with 3% bovine serum, RPMI without serum, OptiMEM-reduced serum, OptiMEM with 3% fetal bovine serum, Calcium/Magnesium-free PBS (CMF-PBS), and PBS with Calcium and Magnesium.
3. Incubate cells for a period of one hour except in the time-course studies showing rapid attachment.
4. Aspirate and wash cells with Calcium- and Magnesium-free PBS.
5. Imaging
    a. Bright field microscopic images of precisely the same field of view, marked at the base of the dish by crosshairs etched with a razor blade, were taken both prior to and following media removal.
    b. Images were taken at 10X magnification from two distinct regions of at least two wells for each trial.
6. Perform cell counts
    a. Cell countes were conducted with a “Cell Counter” ImageJ plug-in to gather quantitative data.

B.3. Microfabrication of Chips

B.3.a. PMMA and Electrode Preparation

1. Cutting Pt wire (76um) into appropriate lengths using a razor blade
2. CAD drawing- stencil for alignment
3. Drilling of holes to thread wire (1/16" bit)
4. Thread Pt wire and secure on opposite side
    a. Place sheet of paper on bottom- ensures uniform surface to assist in thermal bonding
5. Dry overnight

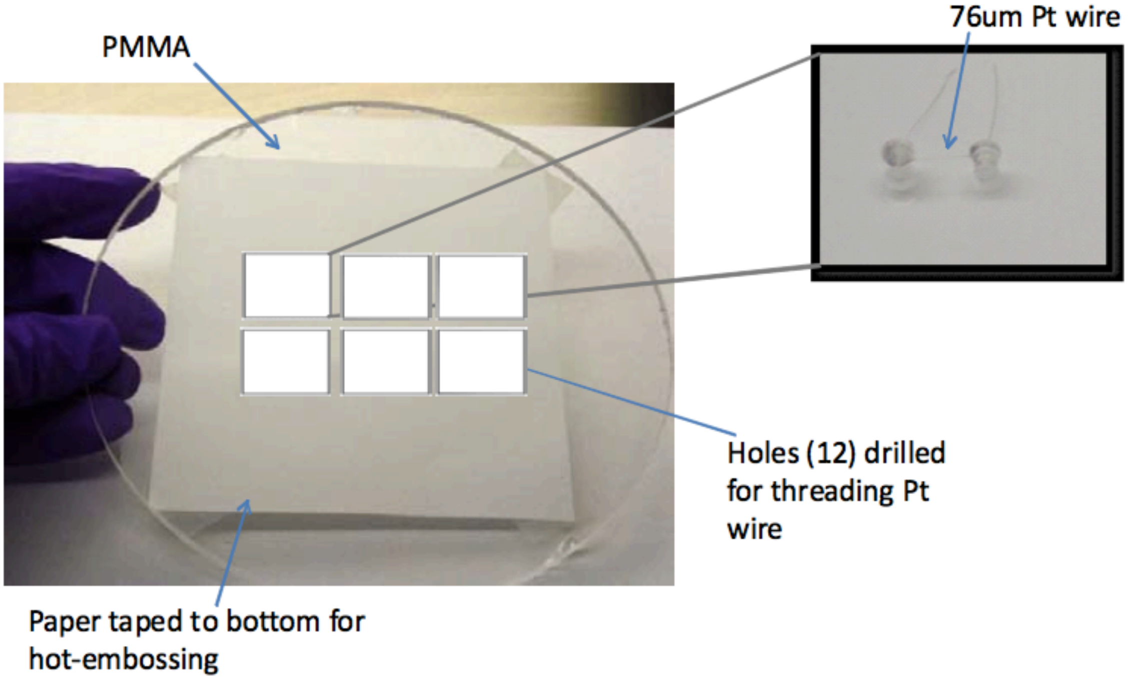

B.3.b. Hot-embossing wire into PMMA(and drying)

<u>**HOT-EMBOSSING WIRE INTO PMMA**</u>

1. After threaded wire-PMMA chip has dried in oven overnight
2. Hot-emboss wire at 160^{o}C for 4min
3. Allow to cool before removing from clamping device

<u>**(OPTIONAL)SURFACE PRETREATMENT EXPERIMENTAL PROTOCOL**</u>

UV surface modification was evaluated to evaluate its need for increasing hydrophilicity (wetability) of the PMMA microchannel to improve flow of cell buffer solution and cells through the 25-um wide x 30-um deep microchannel (Wei et al. 2005).

1. Prepare the PMMA chip
    a. Sonicate 20min with dIH2O (small concentration of IPA)
    b. Dry with Nitrogen gas

    c. Inspect microchannel using microscope
2. Expose Microchannel and coverslip to UV light (254nm at 15mW/cm2) for 8min
    a. Allow PMMA to cool
    b. Rinse with IPA and dIH2O
    c. Dry with Nitrogen gas

B.3.c. Direct Micromilling of Microchannel

MICROMILLING

1. Micromilling of 50-um wide microchannel was performed using a high-precision micromilling (KERN MMP, KERN Micro-und) (precision within +1micron; resolution = 0.0001mm; tools as small as 25microns in diameter)
2. Carefully inspect microchannel and electrode area under stereomicroscope

B.3.d. Washing and Thermoplastic Fusion Bonding

WASHING AND THERMOPLASTIC FUSION BONDING PROTOCOL

Thermoplastic fusion bonding is based on Tg of PMMA; applied pressure in forced convection oven and post-bonding cooling.

1. Cut PMMA polymer into individual chips (such as 20mmx20mm)
    a. Cut the coverslips to size
2. Rinse any oil off chip using Isopropyl Alcohol
3. Use mild surfactant to wash (with toothbrush)
4. Rinse chip off with dIH2O and alcohol
5. Sonicate (15min)
6. Dry the chips with Nitrogen gas
7. Prep the coverslips (0.125 mm thickness PMMA coverslips- cut with scissors/papercutter)
    a. Wash, Rinse, Sonicate
    b. Dry with compressed air
8. Position coverslip so that it covers inlet and outlet
    a. For the guiding channel electrode design, place coverslip so that small amount of wire remains exposed at the electrode reservoir ends
9. Clamp glass plates around assembled chip + coverslip
    a. Glass plates were cut to size of PMMA chip
    b. Binder clips (all-metal) were placed on all sides to apply even pressure
10. Use forced convection oven
    a. Pre-set oven with T_i= 50^{o}C
    b. Set T_f= 108^{o}C for 40min.
    c. Set oven to 50^{o}C and wait 2hrs for cool down
11. Inspect using optical microscope to observe any damage/deformation during thermal bonding
    a. Perform sealing test using gas or air to check for bubbles

B.3.e. Drill Holes for Connecting Posts to Pt Wire & Apply Conductive Epoxy

DRILLING AND APPLICATION OF GOLD POSTS

1. Drilling of holes near the end of Pt wire was done using 1/16" drill bit
2. Gold posts were secured into drilled hole
    a. Conductive paste was used to ensure that the wire and post had a good connection
3. Used Multimeter to verify good connection between the posts-conductive epoxy

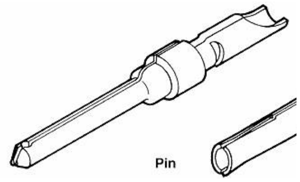

B.3.f Outfit Chip with Microfluidic Fittings

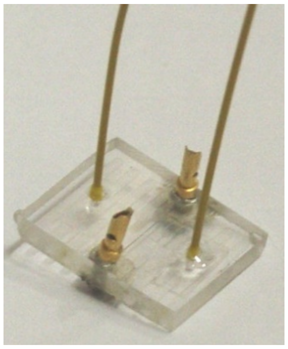

1. Apply clear (5min.) epoxy to end of all-polymer capillary (OD 770um)
    a. Make sure have appropriate leur-to GC capillary leur-lock adapter
2. Allow to harden for a few minutes (so doesn't flow in and block inlet/outlet)
3. Place in inlet/outlet and hold in place for a few minutes
4. Perform sealing test using air or water
5. Evaluate chip using FITC leak test with pressure driven flow before performing cell experiments

B.4. Syringe Pumps & Detection System

B.4.a. Syringe Pump Operation Using MS-DOS (Pump Terminal Emulator)

Required Materials:

Syringe Pumps (NE-500) Microscope computer (Rm 102)
(http://www.syringepump.com/oem.htm)

Summary for Operating NE-500 Syringe Pumps in "PumpTerm"

A. To assign address to Pump 01, disconnect Pump 00 from COM port and connect 01.
   1) Make sure Pump 00 and 01 are not connected to each other.
   2) Type 1ADR and enter in the DOS window. (This sets the pump address to 01).
   3) Change the connection back to 00 being connected to COM port and 00 and 01 connected to each other.

B. After setting the address of each pump, we can now send parameters into DOS to program the two pumps.
   1) For pump 00,
      a. RAT 100MH (since the diameter is set to 8.5, keep within the range)
      b. DIA 8.5
      c. VOL 500
      d. RUN
   2) For pump 01,
      a. 1RAT 100MH
      b. 1DIA 8.5
      c. 1VOL 500
      d. *RUN (This runs both the pumps simultaneously)

Extra Notes: To run the pumps in Lab view, simply set the parameters in the VI and hit on "run" in the toolbar menu. It allows us to run just one of the pumps (in 1 direction).

B.5. Impedance Analyzer and LabView VI

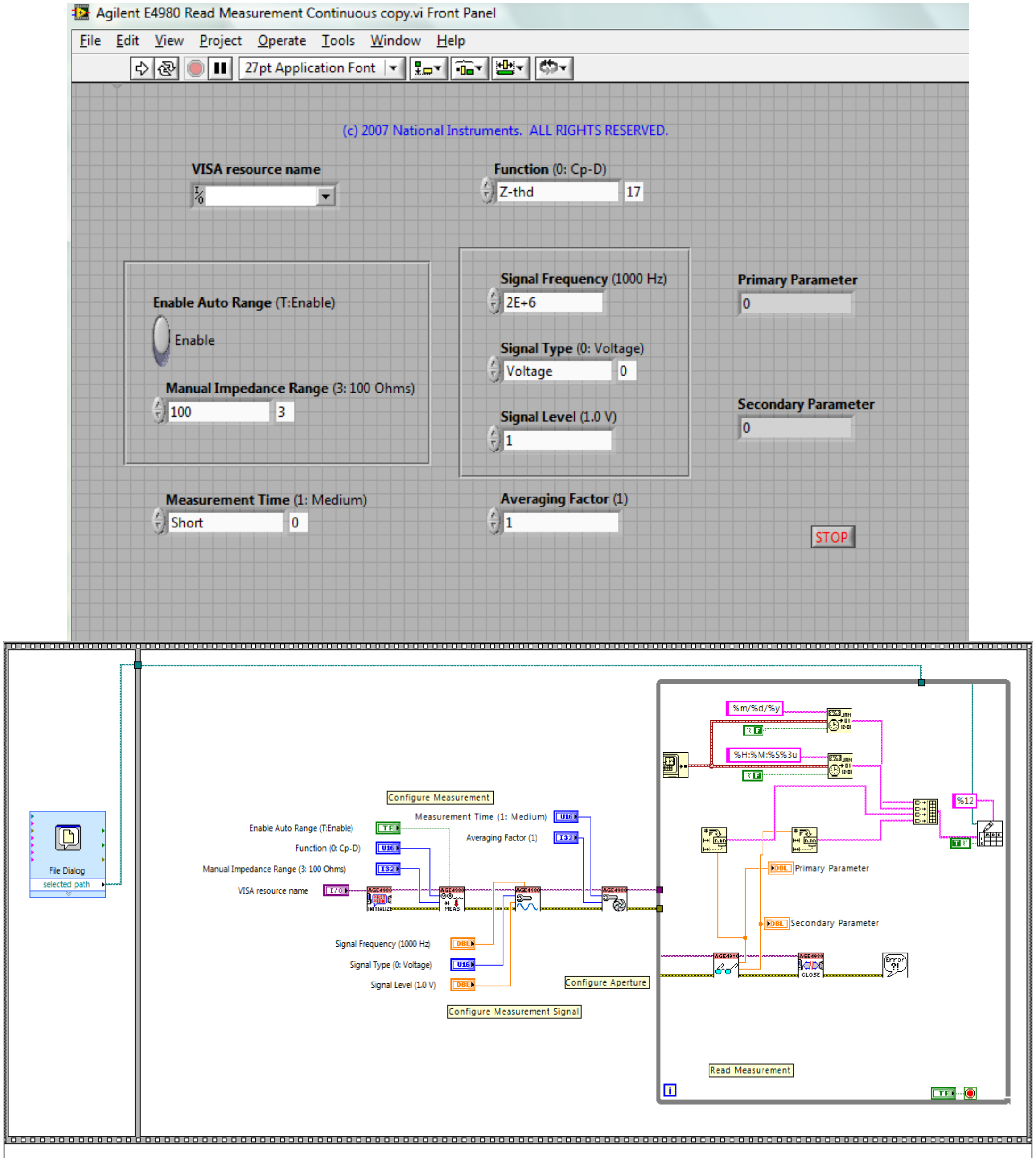

(c) 2007 National Instruments. ALL RIGHTS RESERVED.

VISA resource name:

Function (0: Cp-D): Z-thd 17

Enable Auto Range (T:Enable): Enable

Manual Impedance Range (3: 100 Ohms): 100 3

Signal Frequency (1000 Hz): 2E+6

Signal Type (0: Voltage): Voltage 0

Signal Level (1.0 V): 1

Primary Parameter: 0

Secondary Parameter: 0

Measurement Time (1: Medium): Short 0

Averaging Factor (1): 1

Figure B.5. (A) Front panel and (B) block diagram of Labview VI (National Instruments) for fixed-frequency data acquisition with time-stamp using the Agilent E4980A impedance analyzer.

VITA

Julianne Forman Audiffred was born in Baton Rouge, Louisiana. Her parents are Murray A. and Jean J. Forman, and she has an older sister, Maryelizabeth. Julianne grew up in Baton Rouge and attended St. Joseph's Academy for high school. After graduating high school in 1998, Julianne attended Louisiana Tech University in biomedical engineering and later transferred to Louisiana State University in the spring of 2000. She finished her bachelor's degree in 2002 in biological and agricultural engineering at Louisiana State University. After working in graduate school at the University of Kentucky in Lexington, Kentucky, for a semester, Julianne returned to Louisiana State University to complete a master's degree in biological and agricultural engineering while under a National Science Foundation (NSF) graduate research fellowship. In May 2006, Julianne married her husband, Bryan, and then continued her graduate school career to pursue a doctorate in engineering science, with major concentration of biological engineering and sub-areas of instrumentation and cellular and molecular engineering. Julianne and Bryan welcomed the arrival of their first son, Bennett Alexander, in November 2008.